Geophysical Journal International

*Geophys. J. Int.* (2025) **242,** 1–36
Advance Access publication 2025 June 27
Research Paper

https://doi.org/10.1093/gji/ggaf232

# Rheology and bathymetry effects captured by a multilayer landslide-tsunami model

A. Marbœuf[1], A. Mangeney,[1] A. Le Friant,[1] M. J. Castro,[2] E. Fernández-Nieto,[3] A. Lucas,[1] P. Poulain[1], A. Moatty,[4] M. Silver,[5] R. Pedreros,[6] A. Lemoine[6] and F. Løvholt[7]

[1] *Université Paris Cité, Institut de Physique du Globe de Paris, CNRS, F-75005 Paris, France. E-mail: marboeuf@ipgp.fr*
[2] *Departamento Análisis Matemático, Estadística e Investigación Operativa y Matemática Aplicada, Universidad de Málaga, Campus Teatinos S/N, Málaga 29080, Spain*
[3] *Departamento de Matemática Aplicada I, Universidad de Sevilla, E.T.S. Arquitectura. Avda Reina Mercedes, 41012 Sevilla, Spain*
[4] *UMR LGP (Laboratoire de Géographie Physique), CNRS, Paris 1 Panthéon Sorbonne, UPEC, 2 rue Henri Dunant, 94320 Thiais, France*
[5] *US Department of Agriculture (USDA) Natural Resources Conservation Service (NRCS), 430 G St., # 4164 Davis, CA 95616-4164, USA*
[6] *BRGM, French Geological Survey, Direction Risks, 3 avenue Claude-Guillemin, BP 36009, 45060 Orléans Cedex 02, France*
[7] *Norwegian Geotechnical Institute, sSandakerveien 140, 0484 Oslo (Street Address), P.O. Box 3930 Ullevål StadionNO-0806 Oslo, Norway*

Accepted 2025 June 14. Received 2025 June 10; in original form 2025 April 8

## SUMMARY

Numerical models are a powerful tool for understanding and predicting the impact of landslide-generated tsunamis. We use here the HySEA code which incorporates a multilayer structure and non-hydrostatic pressure to simulate the tsunami generated by a potential submarine landslide located offshore of the Mayotte island. The island is surrounded by a lagoon and steep slopes weakened by the 2018 seismo-volcanic crisis. The influence of the input parameters and of the model assumptions is shown to change by a factor 2 the predicted maximum water free surface elevation, velocity and maximum inundation depth. This demonstrates the need of using numerical models for building local scaling laws to relate tsunami and landslide properties. Our results highlight the necessity of incorporating high-resolution bathymetry, in-depth variations through multilayer modeling and relevant landslide rheology to accurately predict tsunami impact. In case of strong topography variations as in Mayotte, using four layers seems to be a good compromise between accuracy and computational cost. Accounting for these effects would enable to refine hazard maps by identifying safe and high-risk coastal zones and to improve wave arrival time estimates, thus reducing tsunami-related risks in regions like Mayotte.

**Key words:** Numerical modelling; Tsunamis; Submarine landslides..

## 1 INTRODUCTION

Neumann *et al.* (2015) estimate that 625 million people live in low-elevation coastal zones, that is, altitudes below 10 m. That number is expected to increase in the near future and reach 1 billion by 2030, mostly concerning population in least developed countries. Tsunami risk is growing due to climate change and the denser concentrations of people living in these area. While earthquakes are responsible of about 80 per cent of all historical tsunamis, landslides come second with 5 per cent as reported by Harbitz *et al.* (2014). In addition, when landslides are not the sole source of tsunamis, they are also reported as a contributing factor in a further 13 per cent jointly with other sources, sometimes as the main tsunamigenic source. Hence, the landslide contribution is often strong when both earthquakes and landslides are involved. Identifying and assessing landslide-induced tsunami hazards is essential for reducing the risk of catastrophic events on communities. Such assessments often involves hazard or probability maps, which inform early-warning systems, evacuation plans, and the development of natural or engineered coastal defenses.

### 1.1 Landslide tsunami hazard assessment

Landslide-induced tsunami hazard identification and assessment is a challenging task due to its multidisciplinary aspect (Roger *et al.* 2024). This paper focuses on one of the major component of tsunami hazard identification and assessment: numerical modeling of landslide-generated tsunamis. Calibrated towards laboratory experiments (e.g. Grilli *et al.* 2002; Ma *et al.* 2015; Poulain *et al.* 2023) and past landslides and tsunamis in the field (e.g. Crosta

*et al.* 2016; Brunet *et al.* 2017; Gylfadóttir *et al.* 2017; Paris *et al.* 2019; Svennevig *et al.* 2024), numerical models are a powerful tool capable of quantifying tsunami height and velocity over a realistic bathymetry for a given landslide scenario. Yavari-Ramshe and Ataie-Ashtiani review the available approaches in the literature and show the large variety of existing models (Yavari-Ramshe & Ataie-Ashtiani 2016, table 3). Each model implements different degrees of complexity when resolving the water part: (i) 2-D and 3-D hydrostatic models with no dispersion effect that include nonlinear Shallow Water equations (Harbitz 1992; Allgeyer *et al.* 2019; Poulain *et al.* 2022); (ii) Boussinesq or one-layer weakly dispersive models (Lynett & Liu 2002; Aïssiouene *et al.* 2020); (iii) Multilayer non-hydrostatic dispersive models (Macías *et al.* 2021a, b); (iv) Reynolds-Averaged Navier–Stokes (Liu *et al.* 2005) and Large Eddy Simulations (Mokhtarzadeh *et al.* 2021) models; and (v) full Navier–Stokes models (Mangeney *et al.* 2000; Abadie *et al.* 2010; Allgeyer *et al.* 2019). Note that the performances of these models against observations may be evaluated thanks to techniques such that the Nash–Sutcliffe model efficiency coefficient (Mathevet *et al.* 2023). These models are implemented in numerical codes that are currently in use and undergo continuous development: see for example FUNWAVE (Kirby *et al.* 1998), Basilisk (Popinet 2003), HySEA (Macías *et al.* 2015, 2021a, b), OpenFOAM (Rauter *et al.* 2022) or SWASH (Ruffini *et al.* 2021). The reader is referred to Kirby *et al.* (2022); Yavari-Ramshe & Ataie-Ashtiani (2016); Marras & Mandli (2021) for more details. Concerning landslide modeling, the increasing complexity in the models aim at reproducing the behaviour of the mixture between the granular material and the fluid. More accurate models include advanced rheological formulations concerning particle interaction and pore fluid stresses (e.g. Rauter *et al.* 2022). One finds in the literature: (i) depth-averaged models (e.g. Fernández-Nieto *et al.* 2008; Grilli *et al.* 2017; Delgado-Sánchez *et al.* 2020; Gueugneau *et al.* 2021); (ii) Navier–Stokes models (e.g. Heinrich *et al.* 1999; Rauter *et al.* 2021); and (iii) particle-sized models like Smoothed Particle Hydrodynamics or Discrete Element Method (e.g. Radjai & Dubois 2011; Guan & Shi 2023). A comparison between these different methods is performed by Martin *et al.* (2023).

Regardless of their complexity, numerical models have well-known limitations, especially when simulating real-world events. The two primary challenges stem from limited computational power (see e.g. Windows-Yule *et al.* 2015) and gaps in data or understanding of the underlying physical processes. Masson *et al.* (2006) emphasize that the reliability of numerical outputs are sensitive to the quality of available field data. In particular, field data related to a geophysical description of the underburden, including different geophysical horizons, geotechnical properties of soils or composition and stability of joints and faults (in the case of rock slopes), are all of first order importance. The generation and release probability mechanism also involves a high degree of uncertainty that should be embedded in prognostic forecasting (Løvholt *et al.* 2020). Bathymetric data is another important source of uncertainties (Hare *et al.* 2011; Svennevig *et al.* 2024) since high-resolution data (lower than 1 m) are rarely available (Cannat *et al.* 2013). Probabilistic and statistical methods are well suited for dealing with these uncertainties. Several groups have attempted sensitivity analyses (Tinti *et al.* 2000; Gonzalez-Vida *et al.* 2019; Sabeti & Heidarzadeh 2022; Esposti Ongaro *et al.* 2025) sometimes coupled with advanced probabilistic/statistical techniques (Behrens & Dias 2015; Sánchez-Linares *et al.* 2015; Zhao *et al.* 2021; Mulia *et al.* 2022; Tozato *et al.* 2023) to investigate the uncertainties related to input data. For earthquake tsunamis, Probabilistic Tsunami Hazard Assessments approaches have become a standard (Grezio *et al.* 2017, and reference therein). For landslide tsunamis, probabilistic methods are less developed, but have been employed for local settings where there are rich availability of past landside data (Lane *et al.* 2016; Esposti Ongaro *et al.* 2025) or detailed assessment of local slope stability (Løvholt *et al.* 2020, 2025). To this end, improved modeling capabilities for the tsunami generation will reduce modeling uncertainty.

### 1.2 Context and background on Mayotte

The volcanic island of Mayotte is located in the Indian ocean and is composed of Petite Terre and Grande Terre. The island catches the attention of researchers and the French government since the beginning of an intense seismo-volcanic crisis in 2018 (Mercury *et al.* 2022). The location of earthquakes near steep slopes and the construction of a new volcanic structure (Feuillet *et al.* 2021) may trigger submarine instabilities, in particular east of Mayotte (Roger 2019). The two islands Petite Terre and Grande Terre are surrounded by a well-developed shallow submarine shelf defining a lagoon (Fig. 1). The shelf corresponds to a significant topography change, from shallow slopes on the shelf ($< 9^\circ$) to flanks with maximum local slopes of $25^\circ$ to $60^\circ$ (Lemoine *et al.* 2020b; Poulain *et al.* 2022). The flanks are prone to tsunamigenic gravitational instabilities given the repetitive seismic activity located 5–15 km from the coast east of Petite Terre. In deeper water, gullies and canyons form large valleys which may control the circulation of sediments. Studies on Mayotte concern mainly the volcanic and seismic activities (Roger 2019; Lemoine *et al.* 2020a; Saurel *et al.* 2021; Thinon *et al.* 2022; Mercury *et al.* 2022, 2020; Sultan *et al.* 2023). After a preliminary overview considering 62 tsunami scenarios performed by Lemoine *et al.* (2020b), both of seismic and non-seismic sources, Poulain *et al.* (2022) focus on the modelling of the tsunami impact related to submarine landslides. The authors couple two numerical codes: hydrostatic HySEA (Fernández-Nieto *et al.* 2008; Escalante *et al.* 2019; Macías *et al.* 2020) and FUNWAVE-TVD (Wei *et al.* 1995; Kennedy *et al.* 2001; Chen 2006; Shi *et al.* 2012). They test hydrostatic/Boussinesq (i.e. non-dispersive and weakly dispersive) numerical models and the influence of the initial landslide volume through eight different submarine scenarios. However, this coupling introduces additional errors and reduces the computational efficiency. We will focus here on one of the most threatening submarine scenario, identified by Lemoine *et al.* (2020b) and considered by Poulain *et al.* (2022), using only the multilayer code HySEA describing the landslide dynamics as well as tsunami generation and propagation.

### 1.3 Motivation and objectives

While a few landslide-tsunami studies have included in-depth variation in the models using multiple layers in the vertical direction (Macías *et al.* 2017; Pedrosa-González *et al.* 2022; Bonilauri *et al.* 2024), few have numerically tested the influence of the number of layers, with the notable exception of Ongaro *et al.* (2021). This paper builds on Poulain *et al.* (2022), delving deeper into the impact of input parameters. Leveraging recent advancements in HySEA (Macías *et al.* 2021a, b), we conduct a robust sensitivity analysis focusing on newly introduced features controlling the dispersive properties of the model: multilayer structure and non-hydrostatic pressures. Since these new features are computationally demanding, evaluating their impact on the final results is crucial to determine whether their inclusion is necessary. In particular, are these new features of great influence on the computed waves hitting the Mayotte's coasts? We are also interested in the influence of crucial

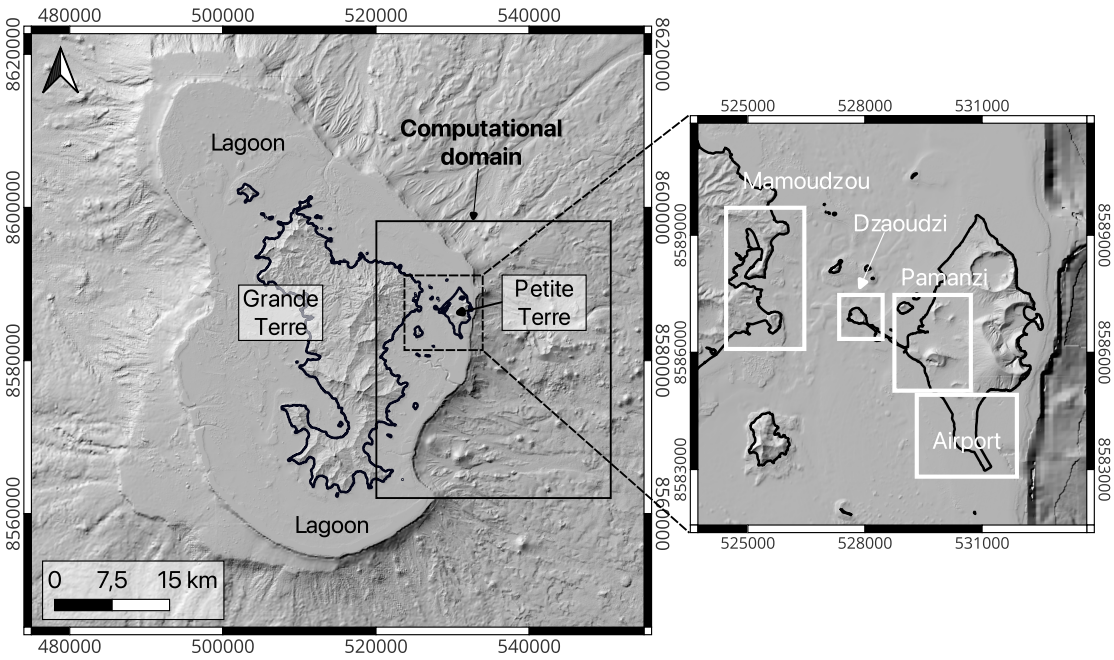


**Figure 1.** Mayotte bathymetric data and computational domain considered in this study. The two islands Petite Terre and Grande Terre are surrounded by a well-developed shallow submarine shelf defining a lagoon. The zoom on the right indicates the sensible areas in terms of strategic infrastructures.

parameters such as the grid resolution or the landslide related parameters. This sensitivity analysis will greatly help in the results interpretation and the choice of many input parameters, given the large uncertainties presented in the literature. As a first attempt to investigate the sensitivity of input parameters on Mayotte simulations, we restrict ourselves to a single volume configuration, such as in Gonzalez-Vida *et al.* (2019). We also keep statistical and probabilistic techniques for next studies.

Although landslide-tsunami models are currently employed for hazard assessment and risk analysis (Leone *et al.* 2011), significant uncertainties remain unquantified. These uncertainties are highly dependent on factors specific to the simulated event, such as topography, material properties, landslide volume, and water depth. Our objective here is to quantify the variability of the sea elevation, runup and tsunami impact velocity induced by: (i) the hydro versus non-hydrostatic approximation; (ii) the precision of the flow description in the vertical direction (from depth-averaged to multilayer equations); (iii) the bathymetry resolution; and (iv) the landslide rheology. The Mayotte configuration is a generic case study involving a coral reef, which often happens in oceanic islands. The coral reef induces strong variations of the bathymetry and related effects on the tsunamigenesis.

The rest of the paper is organized as follows: Mayotte's field data and the selected scenario are presented in Section 2; the multilayer HySEA code is introduced and its Shallow Water models for both the landslide and the water waves are described in Section 3; the reference case is presented in Section 4; the sensitivity analysis is performed in Sections 5, 6 and 7; this work is concluded in Section 8.

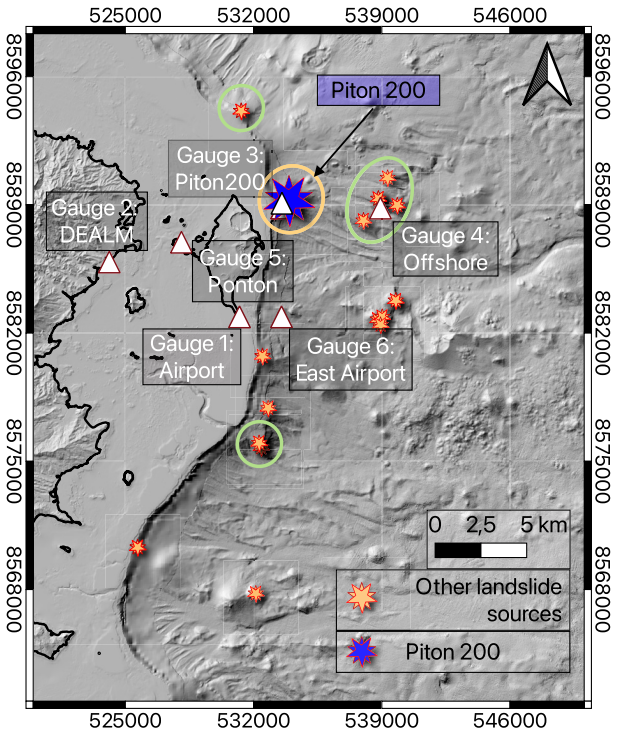


**Figure 2.** Bathymetry and landslide sources from Lemoine *et al.* (2020b). Circled submarine landslide scenarios are those considered by Poulain *et al.* (2022).

## 2 SCENARIO AND FIELD DATA

### 2.1 Mayotte's bathymetric and sea floor data

The accurate description of the bathymetry is known to have a major influence on tsunami propagation. Bathymetric data are shown in Figs 1 and 2 and are taken from Lemoine *et al.* (2020b). The data are based on Gebco 2014 (https://www.gebco.net), HOMONIM SHOM DTM (100 m resolution, https://data.shom.fr), MAYOBS 1 (Feuillet *et al.* 2021) (30 m resolution), bathymetric surveys of SHOM (25 m resolution, https://data.shom.fr), and litto3-D (lidar data at 1 m resolution, https://data.shom.fr). All these data are gathered to build a 10 m resolution Digital Elevation Model (DEM) on the computational domain shown in Fig. 1. The coordinate system

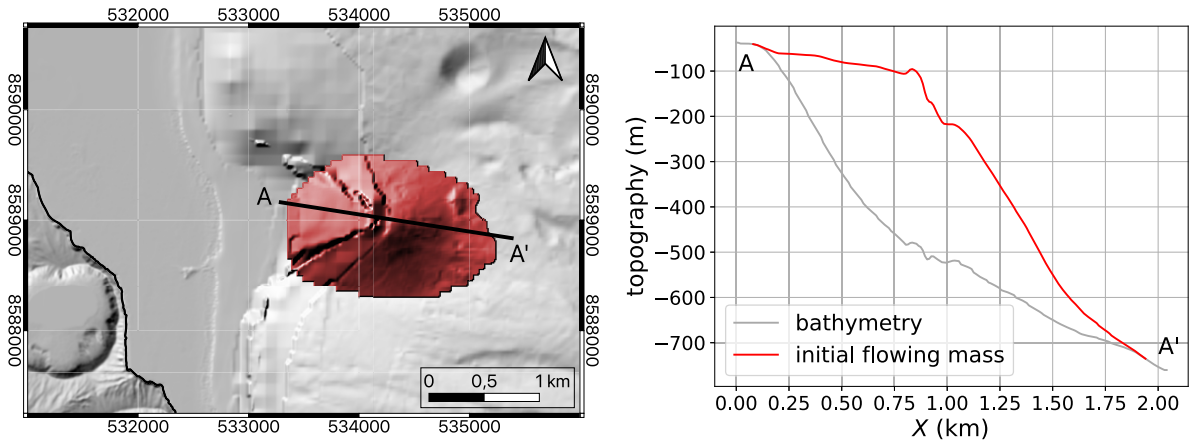


**Figure 3.** (Left) Initial released mass for the considered scenario called Piton 200. (Right) Cross-section (AA′) of the bathymetry and of the initial released mass.

used and displayed for all the figures is EPSG:4471-RGM04/UTM zone 38S. The Histolitt coastline from SHOM is represented on all the figures by a bold black full line. The main specificity of this bathymetry is the steep slope at the coral reef with typical water depths of 1000 m east of the reef and 30 m in the lagoon (Fig. A1).

Fig. A2 shows the spatial distribution of the Manning coefficient involved in the bed-water friction law (Section 3.1). The Manning coefficient is based on sea floor morphology as characterized in the 'Corine Land Cover' database and local coral reef (Lemoine *et al.* 2020b). Given the condition of the sea floor, a corresponding Manning coefficient has been taken from the literature (Bunya *et al.* 2010). Note that the Manning coefficient is higher along the topography change at the border of the coral reef compared to its value elsewhere below the ocean.

### 2.2 Selected scenario

A key challenge in landslide-tsunami hazard assessment is constructing realistic landslide scenarios. This difficulty arises primarily from limited data on tsunamigenic landslide volumes, locations, occurrence rates, digital elevation models, and gaps in understanding landslide dynamics and material behavior (Løvholt *et al.* 2020; Roger *et al.* 2024). In their exploratory study, Lemoine *et al.* (2020b) simulated tsunamis generated by 32 submarine landslide scenarios around Mayotte. The authors identify the most threatening events to the local population and infrastructures from: (i) initial sea surface deformation modeled using TOPICS (Tsunami Open and Progressive Initial Conditions System) tool; (ii) the empirical GEOWAVE model (Watts *et al.* 2003), based on well-tested parameter values. Using more advanced landslide-tsunami simulations, Poulain *et al.* (2022) build and analyse 8 submarine landslide scenarios from the most impactful events with diverse volumes and depths (circled in Fig. 2), providing hazard maps to the local French authorities. However, at that time, they use the hydrostatic depth-averaged version of HySEA coupled with the wave propagation code FUNWAVE-TVD.

Using a single and more precise numerical model, we focus our study on one submarine scenario called Piton 200 selected for the potential threat it represents to the local population and infrastructures (Lemoine *et al.* 2020b; Poulain *et al.* 2022). The collapse structure and extent of Piton 200, described in Fig. 3, are defined by a geomorphological analysis of bathymetric surveys. The collapse structure is located at the shelf with slope transition close to Petite Terre (2.5 km) at depths between 50 and 600 m below sea level. it involves a volume of 200 $Mm^3$. The Piton 200 scenario meets three of the four hazard characteristics of submarine landslide tsunami cited by Roger *et al.* (2024): (i) rapid arrival time or short tsunami travel time, (ii) relatively large wave amplitudes, and (iii) lack of forewarning.

### 2.3 Gauge locations

Fig. 2 presents the locations of the six virtual wave gauges used in this study. Gauge n° 3 is positioned at the Piton 200 location (76.5 m depth) and gauge n° 4 is located 5 km further offshore to provide wave observation in front of the landslide and at greater water depth (1106 m depth). Three additional gauges are put closer to the coast. These gauges have been positioned around major assets for the island: the airport runway, the terminal for the ferry that links Petite Terre and Grande Terre, and the DEALM (Direction de l'Environnement, de l'Aménagement, du Logement et de la Mer). The airport gauge n° 1 is located in the commune of Pamandzi at the end of the current runway (3.23 m depth). The gauge n° 6 is placed 2.3 km east of the airport gauge (same $Y$ coordinate as the airport gauge) on the other side of the reef (466 m depth). This gauge corresponds to the location where the vertical velocity profile is animated: *animationEastAirportVelX.mp4* available in the supplementary material. The gauge n° 6 also defines the cross-section at constant $Y$ coordinate with the airport gauge: Fig. A1, animations *animation1Layer.mp4* and *animation6Layer.mp4* available in the Supporting Information. The pier's gauge n° 5 (Ponton) at 9.8 m depth is located in Dzaoudzi and also represents a critical infrastructure asset, as commuter traffic between Petite and Grande Terre is a daily occurrence. Finally, the gauge n° 2 on Grande Terre (DEALM) is located at 2.5 m depth near the DEALM building at M'tsapéré, south of Mamoudzou. These gauges allow a more local analysis and a closer look to the results at the selected critical locations. Only the 4 first gauges Airport, DEALM, Piton200 and Offshore are included in the main text. For convenience, the gauge data for gauge n° 5 (Ponton) are shown in Appendix D. Table A2 of Appendix D provides the exact coordinates (m) and the depth (m) of these 6 gauges.

## 3 NUMERICAL MODEL

Multilayer HySEA (Hyperbolic Systems and Efficient Algorithms) is part of a family of long wave landslide-tsunami models (Macías *et al.* 2021a, b). HySEA 1-layer models have been widely used and

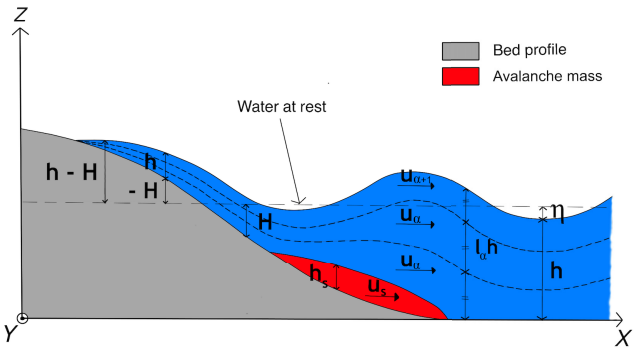


**Figure 4.** Multilayer structure and notations. The water depth $H$ is positive offshore and is negative inland. Inland, $-H > 0$ is the topography.

tested against laboratory experiments (e.g. Poulain *et al.* 2023) and field scale events (e.g. Linares-Sánchez *et al.* 2011; Gonzalez-Vida *et al.* 2019). HySEA models simulate both the granular mass and the water flow, as well as the coupling between the two *via* a friction term at the landslide/water interface (Macías *et al.* 2021a, b) (Fig. 4). The landslide is described by the depth-averaged Savage-Hutter type equations. In 1-layer models, depth-averaged equations for the water motion are considered, including non-hydrostatic water pressures. In multilayer HySEA, on top of the landslide, several layers may be used to describe the water motion. This allows solving part of the vertical structure of the water flow, making it possible, for example, to describe velocity profiles (Fernández-Nieto *et al.* 2016; Garres-Díaz *et al.* 2020; Escalante *et al.* 2023). Adding vertical discretization (several layers) allows to better capture the dispersion effects as shown in Macías *et al.* (2021a). In each layer, the shallow water equations are solved in the $X-Y$ plane and the quantities are averaged in the vertical $Z$-direction over the layer thickness. Note that the shallow approximation and depth-averaging are made in the vertical direction for both the landslide and the water layers while it should be done in the direction perpendicular to the slope for the landslide and in the vertical direction for the water (Delgado-Sánchez *et al.* 2020). However, models accounting for both this effect and multilayer discretization do not presently exist.

### 3.1 Landslide-tsunami model with one water layer

Let us first recall the so-called 1-layer model which consists of 1 layer describing the landslide and 1 layer describing the water behaviour. The equations include non-hydrostatic effects (i.e. dispersive effects) only in the water even though these terms also play a role in landslide dynamics (Garres-Díaz *et al.* 2021). The resulting equations read:

$$\begin{cases} \partial_t h + \partial_x (h\,u) + \partial_y (h\,v) = 0 \\ \partial_t (h\,u) + \partial_x \left(hu^2 + \frac{1}{2} g h^2 + h\,p\right) + \partial_y (h\,u\,v) \\ \qquad = (g\,h + p)\,\partial_x (H - h_s) - S_x \\ \partial_t (h\,v) + \partial_x (h\,u\,v) + \partial_y \left(hv^2 + \frac{1}{2} g h^2 + h\,p\right) \\ \qquad = (g\,h + p)\,\partial_y (H - h_s) - S_y \\ \partial_t (h\,w) + \partial_x (h\,w\,u) + \partial_y (h\,w\,v) = p \\ \nabla \cdot \mathbf{u} + \frac{w_\eta - w_0}{h} = 0, \end{cases} \tag{1}$$

where the unknowns of system (1) are the water surface height $h$, the horizontal water velocity vector $\mathbf{u} = (u\ v)$, the vertical water velocity $w$, the non-hydrostatic pressure $p$, the landslide thickness $h_s$ and its horizontal velocity $\mathbf{u_s} = (u_s\ v_s)$. Offshore, the total water height $h$ is defined as $h = H + \eta$ where $H(x, y)$ is the height of the water at rest above the bed and $\eta$ the sea surface elevation. Inland, $H(x, y)$ becomes negative and $-H > 0$ denotes the topography elevation above the sea level at rest. The water free surface elevation above the water level at rest becomes $h - H$ and $h$ is still the height of the water column above the topography. Fig. 4 describes the notations, both inland and offshore. Eq. (1) simulates the water flow inland and offshore the same way. No distinction is made by the model between inland and offshore zones and no additional model or treatment is needed to resolve the flow inland, outside the usual wet/dry transition treatment at small water depth (Castro *et al.* 2005; Macías *et al.* 2021a). The gravity acceleration is denoted by $g$. The last equation of system (1) is the incompressibility condition and involves the vertical velocity at the free surface $w_\eta$ and the vertical velocity at the bottom $w_0 = -\partial_t (H - h_s)$. The non-hydrostatic pressure is assumed to be zero at the free surface. The friction term

$$\mathbf{S} = (S_x\ ,\ S_y) = g\,h\,\frac{n^2}{h^{4/3}} \|\mathbf{u}\| \mathbf{u} - m_f (\mathbf{u_s} - \mathbf{u})$$

involves the empirical Manning coefficient $n$, controlling the water/bottom friction, and the empirical granular mass/water friction coefficient $m_f$.

The landslide unknowns $h_s$, $u_s$, $v_s$ obey the reduced-gravity Savage–Hutter model (Savage & Hutter 1989), which reads

$$\begin{cases} \partial_t h_s + \partial_x (h_s\,u_s) + \partial_y (h_s\,v_s) = 0 \\ \partial_t (h_s\,u_s) + \partial_x \left(h_s u_s^2 + \frac{1}{2}(1-r) g h_s^2\right) + \partial_y (h_s\,u_s\,v_s) \\ \qquad = (1-r)\,g\,h_s\,\partial_x (H - h_s) - S_{s,x} \\ \partial_t (h_s\,v_s) + \partial_x (h_s\,u_s\,v_s) + \partial_y \left(h_s v_s^2 + \frac{1}{2}(1-r) g h_s^2\right) \\ \qquad = (1-r)\,g\,h_s\,\partial_y (H - h_s) - S_{s,y}, \end{cases} \tag{2}$$

where the friction term writes

$$\mathbf{S_s} = (S_{s,x}\ ,\ S_{s,y}) = g(1-r)\mu\,h_s \frac{\mathbf{u_s}}{\|\mathbf{u_s}\|} + r\,m_f (\mathbf{u_s} - \mathbf{u}).$$

In eqs (2), buoyancy induces a factor $1 - r$ that multiplies the gravity $g$ where $r$ is the density ratio between the constant fluid density $\rho_f$ and the constant grain phase density $\rho_s$

$$r = \frac{\rho_f}{\rho_s}. \tag{3}$$

The buoyancy effects are only taken into account when the landslide is underwater. In this paper, the fluid density is taken to be $\rho_f = 1000$ kg . m$^{-3}$ and the grain phase density is $\rho_s = \rho_g\,\Phi$ where $\rho_g = 2500$ kg . m$^{-3}$ is the grain density and $\Phi$ the solid volume fraction. The solid volume fraction $\Phi$ is included in the sensitivity analysis and its values are discussed in Subsection 3.3. The friction coefficient $\mu$ plays a key role in the granular mass motion (Savage & Hutter 1989; Greve & Hutter 1993; Pouliquen & Forterre 2002; Mangeney *et al.* 2007). Three different formula are tested in this paper, going from the constant Coulomb friction coefficient $\mu_C$ to the more complex Pouliquen and Forterre friction coefficient $\mu_P$ as well as the $\mu(I)$ rheology:

$$\mu_C = \tan(\delta_1), \tag{4}$$

$$\mu_P = \begin{cases} \tan(\delta_1) + \dfrac{\tan(\delta_2) - \tan(\delta_1)}{1 + \beta\,\frac{h_s}{d\,\mathrm{Fr}}} & \text{if } Fr \geq \beta \\ \mu_{\text{start}} + \left(\frac{\mathrm{Fr}}{\beta}\right)^{\chi} (\mu_{\text{stop}} - \mu_{\text{start}}) & \text{if } \mathrm{Fr} < \beta \end{cases}, \tag{5}$$

$$\mu(I) = \tan(\delta_1) + \frac{\tan(\delta_2) - \tan(\delta_1)}{1 + \frac{I_0}{I}}. \tag{6}$$

The parameter $d$ is of the same order of magnitude as the grain diameter and is included in our sensitivity analysis (Table 1). The

**Table 1.** Performed simulations. Friction coefficients $\mu$ are respectively given by eqs (4), (5) and (6). The final time is set to $t_f = 3600$ s for all simulations. $^\star$ the 30 m bathymetry is smoothed thanks to a Gaussian filter of kernel $3 \times 3$. Hydro type: Hydrostatic (H) or Non-hydrostatic (NH).

| Simulation | Hydro type | Layer n° | Grid res. (m) | Solid volume fraction $\Phi$ | Grain size $d$ (m) | Friction angles $\delta$ (°) $\delta_1$ $\delta_2$ $\delta_3$ | Rheology | Manning (s m$^{-1/3}$) | Mass water friction (m s$^{-1}$) | Initial water elevation (m) |
|---|---|---|---|---|---|---|---|---|---|---|
| Ref | NH | 3 | 30 | 0.8 | 1 | 7 17 – | $\mu(I)$ | Fig. A2 | 0.004 | 0 |
| Smoothed | NH | 3 | 30$^\star$ | 0.8 | 1 | 7 17 – | $\mu(I)$ | Fig. A2 | 0.004 | 0 |
| Hydro | H | 1 | 30 | 0.8 | 1 | 7 17 – | $\mu(I)$ | Fig. A2 | 0.004 | 0 |
| 1 Layer | NH | 1 | 30 | 0.8 | 1 | 7 17 – | $\mu(I)$ | Fig. A2 | 0.004 | 0 |
| 6 Layers | NH | 6 | 30 | 0.8 | 1 | 7 17 – | $\mu(I)$ | Fig. A2 | 0.004 | 0 |
| 10 Layers | NH | 10 | 30 | 0.8 | 1 | 7 17 – | $\mu(I)$ | Fig. A2 | 0.004 | 0 |
| 10 m grid | NH | 3 | 10 | 0.8 | 1 | 7 17 – | $\mu(I)$ | Fig. A2 | 0.004 | 0 |
| 50 m grid | NH | 3 | 50 | 0.8 | 1 | 7 17 – | $\mu(I)$ | Fig. A2 | 0.004 | 0 |
| $\Phi = 0.6$ | NH | 3 | 10 | 0.6 | 1 | 7 17 – | $\mu(I)$ | Fig. A2 | 0.004 | 0 |
| 0.1 m grain | NH | 3 | 30 | 0.8 | 0.1 | 7 17 – | $\mu(I)$ | Fig. A2 | 0.004 | 0 |
| 0.5 m grain | NH | 3 | 30 | 0.8 | 0.5 | 7 17 – | $\mu(I)$ | Fig. A2 | 0.004 | 0 |
| 3° friction | NH | 3 | 30 | 0.8 | 1 | 3 13 – | $\mu(I)$ | Fig. A2 | 0.004 | 0 |
| 11° friction | NH | 3 | 30 | 0.8 | 1 | 11 21 – | $\mu(I)$ | Fig. A2 | 0.004 | 0 |
| Coulomb | NH | 3 | 30 | 0.8 | 1 | 7 – – | $\mu_C$ | Fig. A2 | 0.004 | 0 |
| Pouliquen | NH | 3 | 30 | 0.8 | 1 | 7 17 9 | $\mu_P$ | Fig. A2 | 0.004 | 0 |
| Cst Manning | NH | 3 | 30 | 0.8 | 1 | 7 17 – | $\mu(I)$ | 0.025 | 0.004 | 0 |
| $m_f = 0$ | NH | 3 | 30 | 0.8 | 1 | 7 17 – | $\mu(I)$ | Fig. A2 | 0 | 0 |
| +1 m water | NH | 3 | 30 | 0.8 | 1 | 7 17 – | $\mu(I)$ | Fig. A2 | 0.004 | +1 |

Froude number is defined as

$$\mathrm{Fr} = \begin{cases} \frac{\|\boldsymbol{u}_s\|}{\sqrt{g(1-r)h_s}} & \text{if } h_s > 0, \\ 0 \quad \text{otherwise.} \end{cases} \tag{7}$$

We use $\beta = 0.136$ as in Pouliquen & Forterre (2002) even though this was calibrated for glass bead flows in the experiments. For $0 \leq \mathrm{Fr} < \beta$, the friction coefficient $\mu_P$ involves the following quantities

$$\mu_{\text{start}} = \tan(\delta_3) + \frac{\tan(\delta_2) - \tan(\delta_1)}{1 + \frac{h_s}{d}}$$

$$\mu_{\text{stop}} = \tan(\delta_1) + \frac{\tan(\delta_2) - \tan(\delta_1)}{1 + \frac{h_s}{d}}$$

and the empirical parameter $\chi = 0.001$ which is of small influence on the results as soon as $\chi < 0.01$ (Poulain *et al.* 2023). Eq. (6) is a common expression resulting from steady flows on constant slopes (Jop *et al.* 2006) with the inertial number $I$ chosen here as in Martin *et al.* (2023)

$$I = \frac{\frac{5}{2}\,\|\boldsymbol{u}_s\|\,d}{h_s \sqrt{g\,(1-r)\,h_s\,\Phi}}. \tag{8}$$

The empirical value of the constant $I_0 = 0.279$ comes from Jop *et al.* (2006) and Martin *et al.* (2023). The solid volume fraction in the inertial number $I$ is empirically taken to be $\Phi = 0.6$ for all simulations. Changing $\Phi$ in the inertial number $I$ does not significantly affect the simulation results. Note that the $\mu(I)$ rheology make use of two angles $\delta_1$ and $\delta_2$, The Pouliquen and Forterre law $\mu_P$ involves three angles $\delta_1$, $\delta_2$ and $\delta_3$ while the Coulomb rheology only uses one friction angle $\delta_1$.

### 3.2 Multilayer discretization for the water motion

The landslide part is governed by the same equations since only the water column is divided into several layers. The water column of thickness $h$ is decomposed into $L$ sublayers of size $l_\alpha h$, where $\sum_{\alpha=1}^{L} l_\alpha = 1$ as illustrated in Fig. 4. It is usually considered that $l_\alpha = 1/L$, although other definitions exist (Bonaventura *et al.* 2018).

The unknowns of system (9) are now the total water thickness $h$, the horizontal water velocity vector $\mathbf{u}_\alpha = (u_\alpha \; v_\alpha)$, the vertical water velocity $w_\alpha$ for each layers $\alpha = 1, \cdots, L$ and the non-hydrostatic pressure $p_{\alpha-1/2}$ at the lower interface of each layer

$$z = z_{\alpha-1/2} = \sum_{\beta=1}^{\alpha-1} l_\beta h + h_s - H.$$

The vertical averaged velocity is given by $(\bar{u} \; \bar{v}) = \sum_{\alpha=1}^{L} l_\alpha \, \mathbf{u}_\alpha$.

The mass and momentum equations including non-hydrostatic (i.e. dispersive) effects read

$$\begin{cases} \partial_t \boldsymbol{U}_f + \partial_x \boldsymbol{F}_f + \partial_y \boldsymbol{G}_f + \boldsymbol{B}_f = \boldsymbol{H}_f + \boldsymbol{K}_{NH} - \boldsymbol{S}_f, \\ \nabla_{NH} \cdot \boldsymbol{U}_f = \boldsymbol{0}. \end{cases} \tag{9}$$

The conservative terms $\boldsymbol{F}_f$, $\boldsymbol{G}_f$ and the pressure gradient $\boldsymbol{H}_f$ are

$$\boldsymbol{U}_f = \begin{bmatrix} h \\ \begin{bmatrix} h\,u_\alpha \\ h\,v_\alpha \\ h\,w_\alpha \end{bmatrix}_{\{\alpha=1,\ldots,L\}} \end{bmatrix},$$

$$\boldsymbol{F}_f = \begin{bmatrix} h\,\bar{u} \\ \begin{bmatrix} h u_\alpha^2 \\ h\,u_\alpha\,v_\alpha \\ h\,u_\alpha\,w_\alpha \end{bmatrix}_{\{\alpha=1,\ldots,L\}} \end{bmatrix},$$

$$\boldsymbol{G}_f = \begin{bmatrix} h\,\bar{v} \\ \begin{bmatrix} h\,u_\alpha\,v_\alpha \\ h v_\alpha^2 \\ h\,v_\alpha\,w_\alpha \end{bmatrix}_{\{\alpha=1,\ldots,L\}} \end{bmatrix},$$

$$\boldsymbol{H}_f = \begin{bmatrix} 0 \\ \begin{bmatrix} -g\,h\,\partial_x\,(h + h_s - H) \\ -g\,h\,\partial_y\,(h + h_s - H) \\ 0 \end{bmatrix}_{\{\alpha=1,\ldots,L\}} \end{bmatrix}.$$

The breaking dissipation model and the friction terms are defined in $\boldsymbol{S}_f$. The friction terms $\boldsymbol{S}_f$ are only non-zero in the bottom layer $\alpha = 1$ and the breaking model is defined for the vertical momentum

equation at each layer

$$\boldsymbol{S}_{\mathrm{f}} = \begin{bmatrix} 0 \\ g\,h\,\frac{n^2}{l_1 h^{4/3}} u_1 \sqrt{u_1^2+v_1^2} - m_{\mathrm{f}}(u_{\mathrm{s}}-u_1) \\ g\,h\,\frac{n^2}{l_1 h^{4/3}} v_1 \sqrt{u_1^2+v_1^2} - m_{\mathrm{f}}(v_{\mathrm{s}}-v_1) \\ m_1^w \\ \begin{bmatrix} 0 \\ 0 \\ m_\alpha^w \end{bmatrix}_{\{\alpha=2,\dots,L\}} \end{bmatrix}.$$

Following (Scala *et al.* 2024, eq. 8), the coefficients for the breaking dissipation model are defined in the following form,

$$m_\alpha^w = \frac{C}{l_\alpha^2}\sqrt{(\partial_x(hu_\alpha))^2+(\partial_y(hv_\alpha))^2}\,w_\alpha, \tag{10}$$

for $\alpha = 1,\dots,N$, with $C = 35\,\max\left(\frac{\sqrt{\tilde{u}^2+\tilde{v}^2}}{0.4\sqrt{gh}} - 1, 0\right)$ (Roeber *et al.* 2010).

The non-conservative products $\boldsymbol{B}_{\mathrm{f}}$ describe the momentum transfer across layer interfaces

$$\boldsymbol{B}_{\mathrm{f}} = \begin{bmatrix} 0 \\ \begin{bmatrix} (u_{\alpha+1/2}\Gamma_{\alpha+1/2} - u_{\alpha-1/2}\Gamma_{\alpha-1/2})/l_\alpha \\ (v_{\alpha+1/2}\Gamma_{\alpha+1/2} - v_{\alpha-1/2}\Gamma_{\alpha-1/2})/l_\alpha \\ (w_{\alpha+1/2}\Gamma_{\alpha+1/2} - w_{\alpha-1/2}\Gamma_{\alpha-1/2})/l_\alpha \end{bmatrix}_{\{\alpha=1,\dots,L\}} \end{bmatrix},$$

with $\Gamma_{1/2} = \Gamma_{L+1/2} = 0$ and

$$\Gamma_{\alpha+1/2} = \sum_{\beta=1}^{\alpha} l_\beta(\,\partial_x(h(\bar{u}-u_\beta)) + \partial_y(h(\bar{v}-v_\beta))\,)$$

$\alpha = 1,\dots,L-1$.

Interface velocities are defined as $u_{\alpha+1/2} = \frac{1}{2}(u_\alpha + u_{\alpha+1})$ and analoguous definitions for $v_{\alpha+1/2}$ and $w_{\alpha+1/2}$. The term $\boldsymbol{K}_{\mathrm{NH}}$ takes into account the non-hydrostatic effects

$$\boldsymbol{K}_{\mathrm{NH}} = \begin{bmatrix} 0 \\ \begin{bmatrix} -\partial_x(h\,p_\alpha) + (p_{\alpha+1/2}\partial_x z_{\alpha+1/2} \\ \qquad - p_{\alpha-1/2}\partial_x z_{\alpha-1/2})/l_\alpha \\ -\partial_y(h\,p_\alpha) + (p_{\alpha+1/2}\partial_y z_{\alpha+1/2} \\ \qquad - p_{\alpha-1/2}\partial_y z_{\alpha-1/2})/l_\alpha \\ -(p_{\alpha+1/2} - p_{\alpha-1/2})/l_\alpha \end{bmatrix}_{\{\alpha\}} \end{bmatrix},$$

for $\alpha = 1,\dots,L$, where $p_\alpha = (p_{\alpha+1/2} + p_{\alpha-1/2})/2$ and

$$z_{1/2} = h_{\mathrm{s}} - H, \quad z_{L+1/2} = \eta = h + h_{\mathrm{s}} - H$$
$$p_{L+1/2} = 0.$$

Note that the pressure at the free surface is usually set to zero. Finally, the system is completed with the discrete incompressibility condition at each layer

$$\nabla_{\mathrm{NH}} \cdot \boldsymbol{U}_{\mathrm{f}} = \boldsymbol{0},$$

being

$$h\nabla_{\mathrm{NH}} \cdot \boldsymbol{U}_{\mathrm{f}} = \begin{bmatrix} l_1 h\partial_x(hu_1) - l_1 hu_1\partial_x h \\ +l_1 h\partial_y(hv_1) - l_1 hv_1\partial_y h \\ +2(hw_1 - hw_0) \\ \begin{bmatrix} (hu_{\alpha+1} - hu_\alpha)\partial_x z_{\alpha+1/2} \\ +(hv_{\alpha+1} - hv_\alpha)\partial_y z_{\alpha+1/2} \\ -(hw_{\alpha+1} - hw_\alpha) \end{bmatrix}_{\{\alpha\}} \end{bmatrix},$$

for $\alpha = 1,\dots,L-1$ and where $w_0$ is still defined by $w_0 = -\partial_t(H - h_s)$.

Multilayer HySEA implements a parallelized version of the described numerical method on GPU architectures (Castro *et al.* 2011; Escalante *et al.* 2018). The numerical discretization of the system is presented in Appendix F. The reader is referred to Fernández-Nieto *et al.* (2008), Macías *et al.* (2021a, b) and Escalante *et al.* (2018) for more details about the numerical method.

### 3.3 Unknown parameters and model assumptions for the sensitivity tests

We perform a series of numerical simulations, listed in Table 1, by varying key parameters involved in the model around a reference simulation (Section 4). In all simulations, the final time is set to $t_{\mathrm{f}} = 3600$ s and open boundary conditions are prescribed thanks to sponge layers absorbing the waves. The size of this sponge layer is defined to be four cells and thus depends on the grid resolution. The reference simulation has the following features: (i) non-hydrostatic three layers simulation; (ii) 30 m bathymetry grid; (iii) $\mu(I)$ rheology; (iv) first friction angle $\delta_1 = 7°$; (v) a characteristic grain size diameter $d = 1$ m; (vi) a solid volume fraction $\Phi = 0.8$; (vii) the spatialized Manning coefficient of Fig. 2 varying with the bed properties between 0.025 and 0.2 $\mathrm{s\,.\,m^{-1/3}}$; and (viii) a landslide/water interface friction $m_{\mathrm{f}} = 0.004$ $\mathrm{m\,.\,s^{-1}}$. Each simulation differs from the reference case by only one parameter for consistency and comparison purposes. The only exception concerns the Hydro simulation which is hydrostatic with 1 layer in the water column. For all the simulations, the same friction angles' differences are kept for all the sets: $\delta_2 - \delta_1 = 10°$ and $\delta_3 - \delta_1 = 2°$ as done in Pouliquen & Forterre (2002), Poulain *et al.* (2023) and Brunet *et al.* (2017) (see also the discussion in Poulain *et al.* (2023) for the choice of the friction angle). In the following, we refer to a set of friction angles only by the first one $\delta_1$. We varied the first friction angle $\delta_1$ by decreasing/increasing it by 4°, giving $\delta_1 = 3°$, $\delta_1 = 7°$ and $\delta_1 = 11°$. Note that $\delta = 11°$ approximately corresponds to the friction angle given by the law $\mu_{\mathrm{c}} = V^{-0.0774}$, with $V$ the landslide volume, fitted empirically by Lucas *et al.* (2014) on subaerial landslides. The effect of the solid volume fraction $\Phi$ has been tested in the grain phase density. The order of magnitude of the maximum packing fraction of mono-disperse granular media is 0.6 but this volume fraction increases for poly-disperse materials (Andreotti *et al.* 2013). We have thus considered two typical values $\Phi = 0.6$ and $\Phi = 0.8$ in this paper. We also considered different values for the parameter $d$ (0.1 and 0.5 m) as well as for the Manning and interface friction parameters, which are generally highly uncertain.

The 10 m resolution DEM from Lemoine *et al.* (2020b) is degraded for obtaining the 30 and 50 m grids. The resolution degradation is performed by removing rows and columns from the raster of data to avoid additional treatments (like interpolations) and uncertainties. The 30 m resolution for the grid is chosen for the reference case for its reasonable computation time given all the performed simulations and our computational capabilities: Appendix E Table A3 as well as Fig. A10. To quantify bathymetry effect, we: (i) reduce the quality of the 30 m DEM while keeping the same number of grid points in the numerical scheme; and (ii) decrease/increase the accuracy of the DEM with decreasing/increasing the number of grid points. We consider 10, 30 and 50 m grids in this paper. Concerning the first point (i), we reduce the bathymetry quality by smoothing the DEM: 'Smoothed' case in Table 1. The smoothing process is implemented using a $3 \times 3$ kernel window Gaussian filter, which is commonly used for bathymetric data as it balances the need for noise reduction and the preservation of the spatial resolution. The kernel's coefficients were calculated based on the

Gaussian function, which is defined as

$$G(x, y) = \frac{1}{2\pi\sigma^2} e^{-\frac{x^2+y^2}{2\sigma^2}}$$

where $x$ and $y$ are the distances from the kernel's center, and $\sigma$ is the standard deviation of the Gaussian distribution. The value $\sigma = 3$ was chosen to ensure that the filter effectively smooths the data without overly blurring important features of the bathymetry.

Another source of uncertainty is the initial water level which varies with time due to the tide and which is expected to increase between 63 cm up to 1.32 m at the end of the century (Pörtner *et al.* 2019; Intergovernmental Panel on Climate Change, IPCC). We consider a case where the initial water level at rest is increased by 1 m: '+1 m water' case in Table 1.

Concerning the model assumptions, the hydrostatic approximation, leading to much simpler equations and comparatively very low computational cost, is not always valid. Non-hydrostatic pressures are sometimes required, as widely observed in the literature (Kirby *et al.* 2022; Poulain *et al.* 2023). Outside of the lagoon of Mayotte, it is likely to find wavelengths with the same order of magnitude as the water depth $H$ (Poulain *et al.* 2022), thus challenging the hydrostatic approximation. We will investigate here the differences between hydrostatic and non-hydrostatic simulations.

Another key point here is to investigate the effect of adding layers in the vertical directions (i.e. increasing the vertical discretization) to describe the water motion in the non-hydrostatic case. Three layers are recommended by Macías *et al.* (2021a) corresponding to the better compromise between accuracy and computational cost. Indeed, they show that a 3-layers model reproduce the phase velocity from the Airy's theory with a good accuracy for $0 \leq k\,H \leq 15$ where $k$ is the wave number. Using less layers significantly increases the error in this range of $k\,H$. Here, the number of layers is taken between 1 and 10. Finally, the breaking wave mechanism described in eq. (10) has also been tested (Scala *et al.* 2024). We restrict ourselves to the parameters listed in Table 1 for the sake of clarity of this paper and these results are shown in the Supporting Information. The maximum sea surface elevation is shown in Fig. S10 (Supporting Information) when the breaking model is active. For comparison purposes, Fig. S10 (Supporting Information) also includes the maximum sea surface elevation for the reference case (Fig. 9c). This feature affects the maximum sea surface elevation but the difference remains limited. In particular, the same amount of waves seems to pass the lagoon in both cases.

## 4 LANDSLIDE AND WATER WAVE DYNAMICS FOR THE REFERENCE CASE

Fig. 5 shows the water wave propagation in the reference case. The landslide mass flows downwards the slope at a 54 m . s$^{-1}$ maximum velocity (Fig. S3 in the Supporting Information), almost stops at 250 s and reaches a runout distance of 8.14 km (Table A1). We clearly see the influence of the lagoon that dissipates and slows down the waves.

Water waves take around 60 s to reach the closest coast of Petite Terre, 170 s to reach the airport gauge n° 1, and 805 s to reach the DEALM gauge n° 2 on Grande Terre. Sea surface elevations of around 3 m height propagating at 2 m . s$^{-1}$ are recorded around 60 s after the event, when they first hit the eastern coast of Petite Terre (Fig. 5a for the first impact location). This illustrates the threat represented by the scenario Piton 200. In that eastern part of Petite Terre where the depth $H \simeq 2$ m, the computed velocity of 2 m . s$^{-1}$ is of the same order of magnitude than the shallow velocity approximation $\sqrt{g\,H} \simeq 4.5$ m . s$^{-1}$. Maximum sea surface elevation and maximum surface velocities are shown later in the paper when discussing the other simulations (Fig. 9 and Fig. S1 in the Supporting Information). The landslide dynamics and the maximum landslide velocity are also displayed in Figs S2 (top row) and S3 in the Supporting Information. Fig. 6 represents the sea surface elevation at the gauge locations in the reference case (dark blue line). The sensitivity range of the sea surface elevation obtained from all the simulations listed in Table 1 displays the significant impact of the tested parameters. The sea surface elevation varies by a factor around 2–3 and up to 4 approximately compared to the reference case (see the first variation band peak on gauge n° 4).

Note that our results differ from what was obtained in Poulain *et al.* (2022) by coupling HySEA hydrostatic and FUNWAVE-TVD non-hydrostatic simulations. This may be due to the different approximation used (fully hydrostatic or fully non-hydrostatic here) and to the influence of the coupling time considered in Poulain *et al.* (2022). Poulain *et al.* (2022) simulate the landslide and generated near-field waves with hydrostatic HySEA and define a coupling time at which the computed water state is transferred to FUNWAVE-TVD. At the coupling time, the computed waves in HySEA (hydrostatic simulation) are used to initialize FUNWAVE-TVD (non-hydrostatic simulation). These waves continue to propagate thanks to FUNWAVE-TVD.

## 5 KEY ROLE OF NON-HYDROSTATIC EFFECTS

Figs 7(a) and (c) show the maximum sea surface elevation $\iota_{ij}$

$$\iota_{ij} = \max_t \eta_{ij}(t), \tag{11}$$

for the hydrostatic (Hydro) and non-hydrostatic (1 Layer) cases, both dealing with 1 layer to describe the water motion. Inland on Petite Terre, the inundation pattern of Figs 7(b) and (d) correspond to the maximum inundation depth

$$\max_t h_{ij}(t). \tag{12}$$

Note that, inland, the sea surface elevation relative to the water at rest writes $\max_t h_{ij}(t) - H$ (Fig. 4). Recall that multilayer HySEA resolves water flow inland the same way as offshore. No treatment is needed to create the inundation maps. The three resolutions considered in this paper do not allow for analyses of inundation patterns at building scale. The inundation maps are intended to provide a general trend and a comparison point to determine the influence of input parameters.

Non-hydrostatic effects drastically change the result with major differences observed east of the lagoon. Overall, the hydrostatic simulation shows larger waves with smoother spatial variation of the maximum sea surface elevation. The waves overcome the reef and enter the lagoon more easily in the hydrostatic case. Around the Piton 200 collapse area, the wave pattern reflects the landslide trajectory very precisely only in the non-hydrostatic case. For both hydrostatic and non-hydrostatic cases, no more than 1.5 m waves are observed throughout the simulation inside the lagoon. The waves height passed the lagoon are mostly below 1 m; and even below 0.5 m in the larger part of the lagoon for the non-hydrostatic case. Waves are largely stopped by the coral reef which

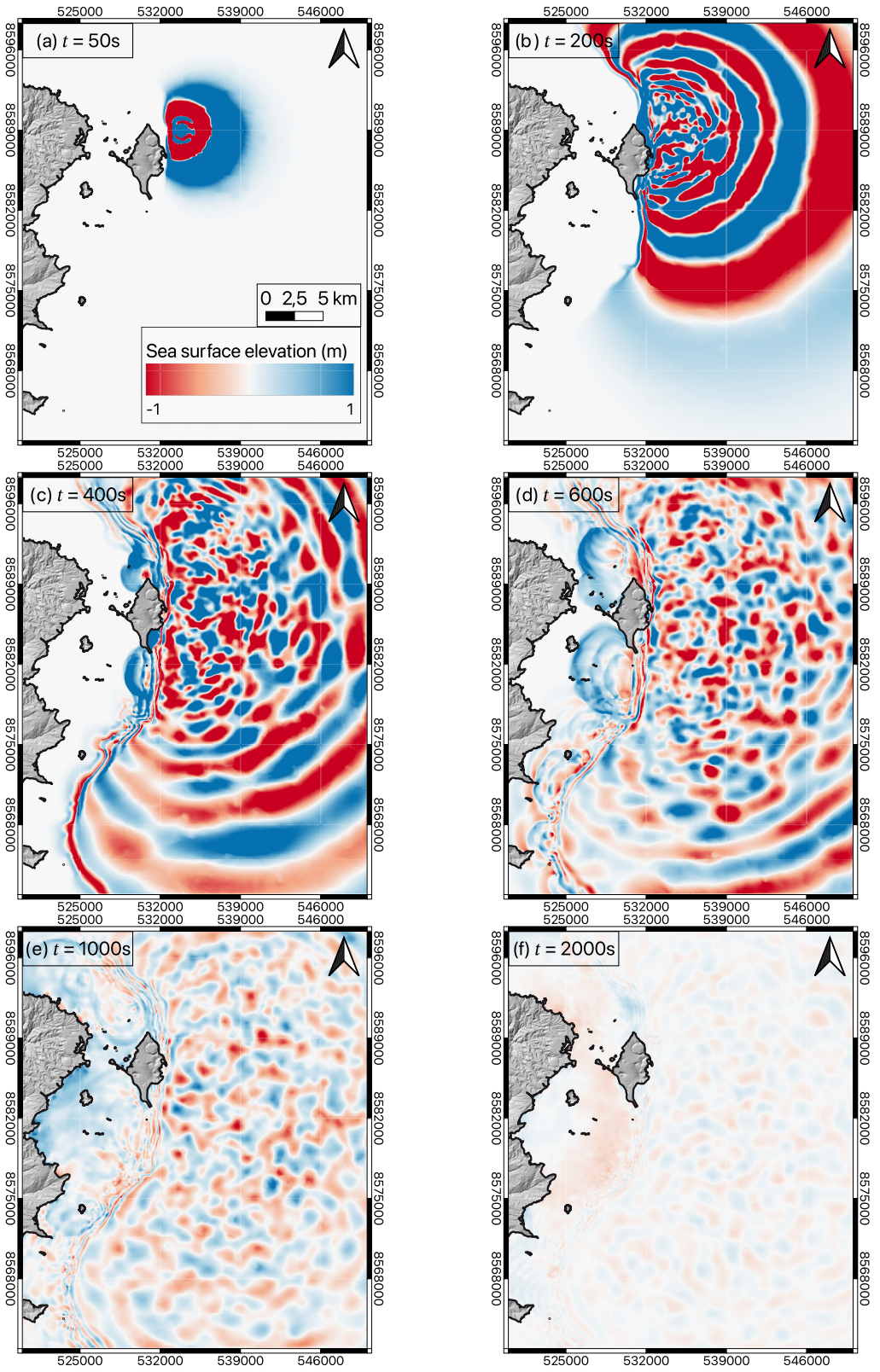


**Figure 5.** Propagation of water waves for the reference case: sea surface elevation at different times.

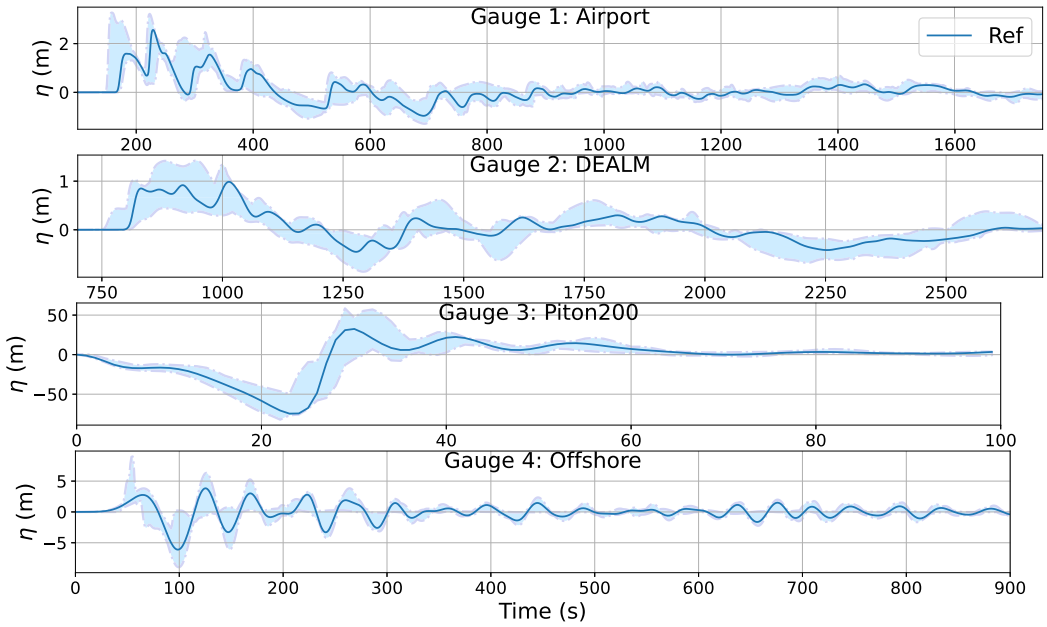


**Figure 6.** Sea surface elevation $\eta$ for the reference case and variation band given by all the simulations of Table 1.

offers a great protection for the coasts of Mayotte. This artificial impact of the reef in the 1-layer models differs from what is obtained with the 3-layers reference case as discussed later (Section 6).

Waves however reach the east coast of Petite Terre but the high relief (+10 m) prevents the water from entering inland. We also see higher waves in the south east part of Petite Terre in the hydrostatic case. In Figs 7(b) and (d), a larger part of the airport area is covered by water in the hydrostatic case (lower than 1.5 m). This is also illustrated at the airport gauge n° 1 in Fig. S5 (Supporting Information) where the maximum wave is almost three times higher in the hydrostatic case. Much higher maximum waves are obtained at the offshore gauge n° 4 in front of the landslide, consistent with what is observed in laboratory experiments of granular flows and generated waves (Poulain *et al.* 2023). At this gauge n° 4, the waves are completely attenuated after 250 s in the hydrostatic case while the signal is still visible around 600 s in the non-hydrostatic case. Overall, the hydrostatic simulation overestimates the first waves (or the first water drop in the Piton 200 collapse area) up to a factor 3 compared to the non-hydrostatic 1-layer case. However, in the Mayotte configuration, the overestimation related to the hydrostatic approximation is not so much impactful on the coasts due to the artificial reef protection.

At early times, the wave signal contains much higher frequencies (>40 mHz) in the hydrostatic case as illustrated on the spectrograms at the offshore gauge n° 4 in Fig. 8. This is due to the well-known sharp variations of the initial wave near the source in hydrostatic simulations (Poulain *et al.* 2023). The hydrostatic assumption strongly impacts the whole frequency content of the wave trains (Fig. 8). This assumption is indeed no longer valid at the offshore gauge n° 4 for example. The shallow approximation assumes $H/\lambda << 1$, where $\lambda$ is the tsunami wavelength. If we assume a velocity scaling with $\sqrt{gH}$, this leads to

$$f << \sqrt{\frac{g}{H}}.$$

At the offshore gauge n° 4, the water depth is $H \simeq 1100$ m, requiring $f << 95$ mHz while the dominant frequency $f \simeq 20$ mHz is only five times smaller (Fig. 8). On the opposite, the depth at the airport gauge n° 1 is $H \simeq 3$ m meaning $f << 1800$ mHz. We observe a dominant frequency of around 1 mHz in Fig. S9 (Supporting Information) for all the presented simulations at the airport gauge, which means that the hydrostatic assumption is valid at this gauge. Note that for frequencies smaller than $\simeq 10$ mHz (periods $T \geq 100$ s), the frequency content of the hydrostatic and non-hydrostatic cases well match (Fig. 8c). Contrary to the early times, when $t \geq 100$ s, the frequency content in the non-hydrostatic case is higher than in the hydrostatic case, describing more precisely the wave train following the first waves (Figs 8a and b).

## 6 CRUCIAL NEED OF MULTILAYER MODELS AND HIGH RESOLUTION BATHYMETRY

### 6.1 Effect of vertical discretization (number of layers)

One of the key result of this work is the crucial role of vertical discretization in capturing strong topography variations as those related to the presence of the coral reef.

#### *6.1.1 Maximum sea surface elevation*

Fig. 9 shows the significant differences in maximum sea surface elevation $\iota_{ij}$ between simulations as the number of layers increases. The barrier power of the coral reef decreases with more layers. The main difference is observed between 1 layer and 3 layers. Indeed, with 3 layers, wave heights reach 0.5–1 m in the lagoon while they are mostly smaller than 0.5 m with 1 layer (Figs 9(a) and (b)). Using 6 and 10 layers still increases the wave capacity to overcome the coral reef barrier (comparing Figs 9(b) and (c)). As a result, the 1-layer case dramatically underestimates the waves past the lagoon:

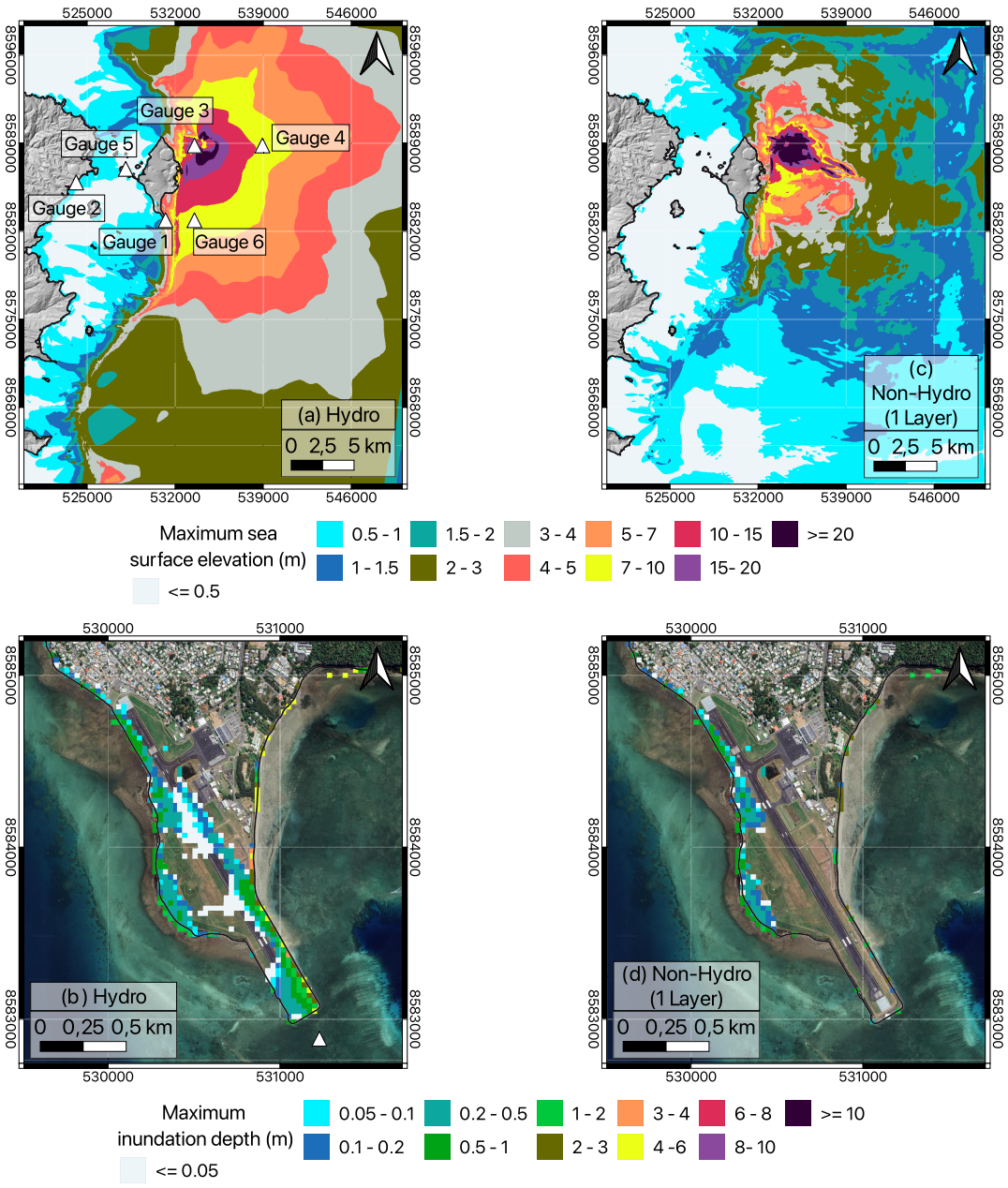


**Figure 7.** (a) Maximum sea surface elevation $\iota_{ij}$ (eq. 11) for the hydrostatic case. (b) Maximum inundation depth for the hydrostatic case. (c) Maximum sea surface elevation $\iota_{ij}$ (eq. 11) for the non-hydrostatic case (1 layer). (d) Maximum inundation depth for the non-hydrostatic case (1 layer).

we observe a factor 2 comparing with 3 layers (Figs 9(a) and (c)) and 6 layers (Figs 9(a) and (e)). Signed differences between -25 and -100 per cent are found in the Piton 200 area when comparing 1- and 3-layers simulations (Fig. A3(a)). The 1-layer simulation also shows more than 100 per cent of difference with the 3-layers reference case inside the lagoon. The differences become much smaller as we continue to increase the number of layers. For example, we still have differences up to 60 per cent between the 3- and 6-layer cases. For a reasonable accuracy and computational cost, the optimal number of layer seems to be slightly higher than 3 layers, recommended by Macías *et al.* (2021a), probably due to strong bathymetry variations around Mayotte. The 6- and 10-layers simulations show similar results and tend to converge on all gauges (Fig. 10). Interestingly, the frequency content for a number of layers greater than 3 is very similar with frequencies up to 45 mHz. On the contrary, the 1-layer model only captures frequencies $f < 35$ mHz ($T > 28$ s) as shown in Fig. 11.

Concerning the wave impact on the Mayotte coasts, Figs 9(b), (d) and (f) presents the inundation pattern on Petite Terre depending on the number of layers. In the multilayer cases (above 3 layers), the water enters and propagates inside Petite Terre over approximately 100 m on a 2 km coastline south west at the airport location. In that area, recorded maximum water height are around 1 m but 50 cm of water covers the most part of the inundated zone. The path leading to the most western part is largely flooded by 40 cm and a small area north west is also covered by water. The water height reaches approximately 80 cm in that area. The 1-layer model leads to much less inundation in Fig. 9 (b): the water penetrates the land over 50 m in average and observed water height are around 30 cm. The high relief (+10 m) protects the east coast of Petite

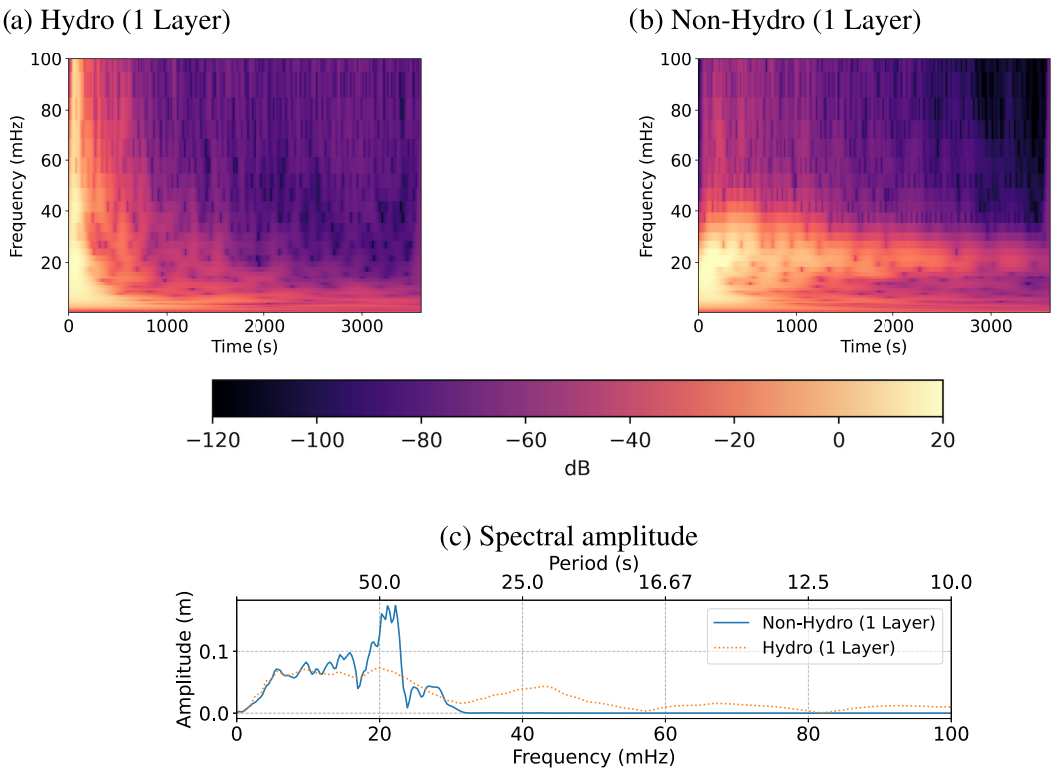


**Figure 8.** Spectrogram and spectral amplitude of the sea surface elevation signal at the gauge n° 4: Offshore.

Terre from inundation. The sea surface velocity patterns shown in Fig. S1 (Supporting Information) looks roughly similar between each other. As for the maximum sea surface elevation, the major differences are observed for the 1-layer case: in the landslide area, where the final deposit pattern is more visible, and inside the lagoon, where the reef offers a higher protection. The 3-layer model leads to higher velocities. For example, inland at the airport location, water penetrates with velocities around 0.5 $\mathrm{m.s^{-1}}$ in the 1-layer case (Fig. S1b in the Supporting Information) and around 1.5 $\mathrm{m.s^{-1}}$ in the 3-layer case (Fig. S1d in the Supporting Information). The overestimation of the barrier power of the coral reef with the 1-layer model is observed at the gauge n° 2 (Fig. 10). More gauge results are given in Appendix D.

The increased accuracy with more water layers comes with the price of a higher computational cost as it is shown in Fig. A10(a). The real computational time is expected to grow linearly with the number of layers: a 2-layer simulation doubles the computational time compared to a 1-layer simulation. We observe indeed a linear trend in Fig. A10(a). The mean error of the simulated maximum sea surface elevation for 1 layer compared to the 10-layer simulation is non-negligible (Fig. A10(b)). It stays below 20 cm as soon as we consider 2 layers or more, and it decreases rapidly as we increase the number of layers. We estimate a reasonable number of layers in term of accuracy and computational cost being 4 layers according to Fig. A10(b). We note that the Mayotte configuration demands a number of layers higher than 3, while the gain from 6 layers or more seems low. In particular, the mean error decrease is non-negligible when going from 3 to 4 layers. Three layers is the recommended value from Macías *et al.* (2021a), based on analytical formula derived from the model to determine its dispersive properties.

### *6.1.2 Velocity profiles and power to overcome large reliefs*

The capacity of the waves simulated by the multilayer model to overcome large reliefs depends on how the model captures vertical profiles of the velocity. Such information is intrinsically missing in depth-averaged 1-layer models. An example of velocity profiles is given in Fig. 12 at the airport gauge n° 1. In multilayer models, even if the water flow is blocked by the bathymetry obstacle at depth, resulting in a strong drop of the horizontal velocity close to the sea floor, the surface velocity may stay large, allowing the water to overcome large reliefs. On the contrary, with only 1 layer, the bathymetric variations greatly impact the whole water column of constant velocity. The depth-averaged $X$-velocity in the 1-layer model is 1.5 times smaller than the averaged velocity obtained with 10 layers (if we remove the bottom layer) at the airport gauge n° 1 (Fig. 12a). The bottom boundary layer sees a lower velocity due to friction while the rest of upper layers in the water column experiences a much higher velocity. While using 10 layers still increases the precision, the profiles of the horizontal and vertical velocities are close for 6 and 10 layers. It seems that we observe a convergence in the vertical profiles when increasing the number of layers. The velocity field is complex across the reef as shown in the movies *animation1Layer.mp4* and *animation6Layer.mp4* representing the velocity vectors along a 2-D $X-Z$ cross section between airport (left) and east airport (right) gauges (Supporting Information). We may even observe higher horizontal velocities at the bottom layer than at the surface: see the animation *animationEastAirportVelX.mp4* between 120 and 140 s, showing the time change of the velocity vertical profiles at the east airport gauge.

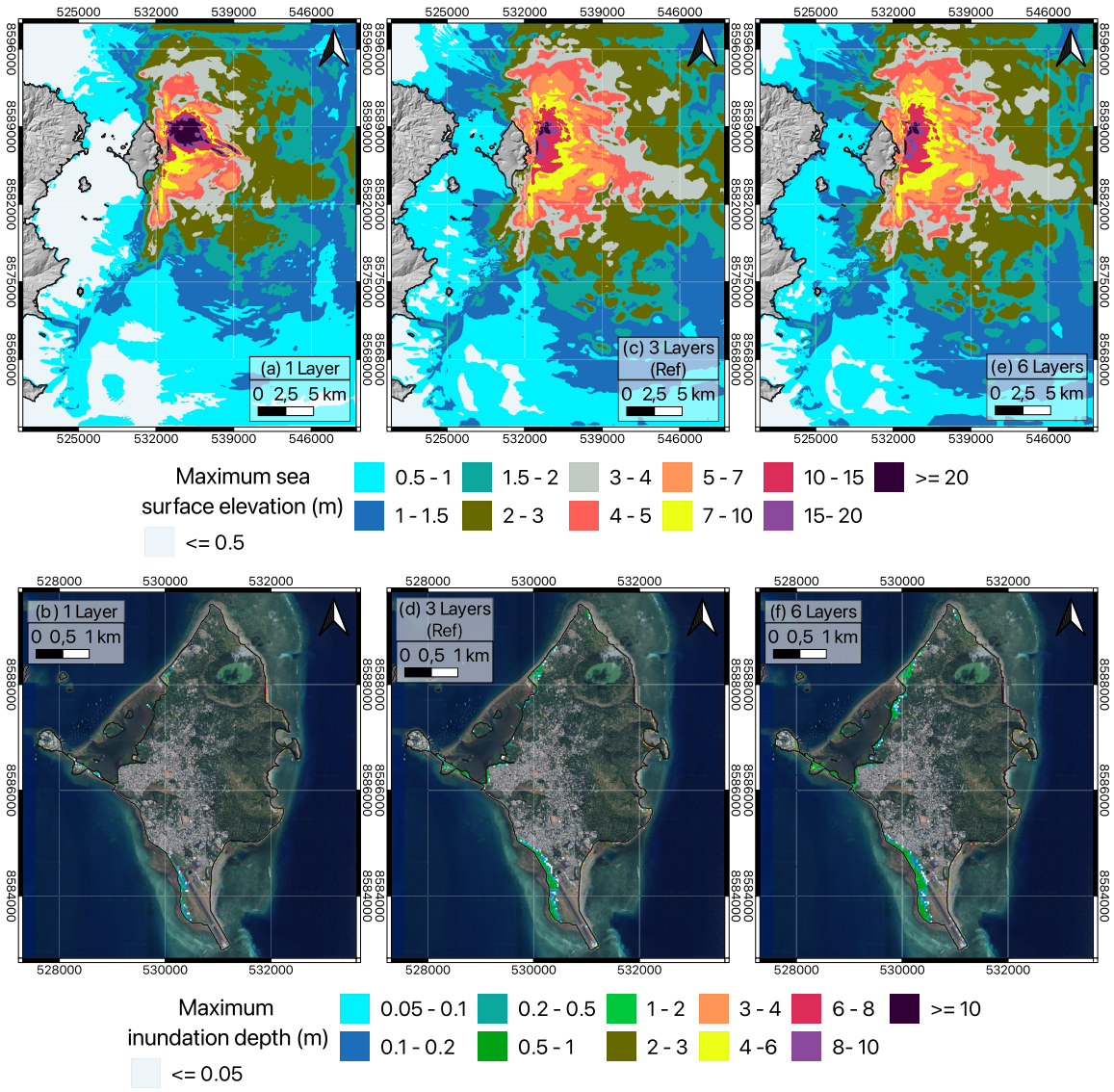


**Figure 9.** (a) Maximum sea surface elevation $\iota_{ij}$ (eq. 11) for 1 layer. (b) Maximum inundation depth for 1 layer. (c) Maximum sea surface elevation $\iota_{ij}$ (eq. 11) for 3 layers (reference case). (d) Maximum inundation depth for 3 layers (reference case). (e) Maximum sea surface elevation $\iota_{ij}$ (eq. 11) for 6 layers. (f) Maximum inundation depth for 6 layers.

### 6.2 Bathymetry resolution and accuracy

The resolution of bathymetry data is expected to impact the simulation results even though there are not many in-depth studies of the resolution effects in literature. Figs 13(c) and (e) show similar patterns on the maximum sea surface elevation outside the lagoon for 30 and 10 m bathymetry grids. The capacity of waves to overcome the reef barrier is however higher on the 10 m grid. The east coast of Grande Terre mostly sees waves of around 1 to 1.5 m with the 10 m grid, as opposed to 0.5 to 1 m with the 30 m grid. In the west coast of Petite Terre, the 10 m grid noticeably lead to higher maximum inundation depth and higher velocities as illustrated in Figs 13(d), (f) and Fig. S1 (Supporting Information). Inland at the airport location, water penetrates with high velocities around 1.5 $\mathrm{m.s^{-1}}$ on the 30 m grid (Fig. S1d in the Supporting Information) and even 2.5 $\mathrm{m.s^{-1}}$ on the 10 m grid (Fig. S1f in the Supporting Information). The high impact of the resolution of bathymetric data is also visible in Fig. A4 showing differences in the sea surface elevation between the different grid simulations up to 60–80 per cent in the lagoon.

We argue that these differences are related to the accuracy of the bathymetry and not to numerical dissipation. Indeed, the numerical dissipation is known to decrease with finer resolution meshes but is expected to be significant only after a few hours of simulations as recently shown in Svennevig *et al.* (2024). It would be interesting to run simulations on finer grids to more precisely quantify bathymetry impact on generated waves, but it is beyond the scope of this paper. Furthermore, it is quite rare to get bathymetry data in such a wide area with precision lower than 10 m. Finally, we check the effect of a smoothed, low resolution bathymetry described by a 30 m grid. Note that the dashed black coastline calculated from the smoothed bathymetry does not exactly fit with the Hystolitt coasline because of the smoothing process. While we observe roughly the same pattern on the maximum sea surface elevation between the smoothed and reference case (Figs 13(a) and (c)), the waves overcome the reef more easily with the smoothed grid. The differences

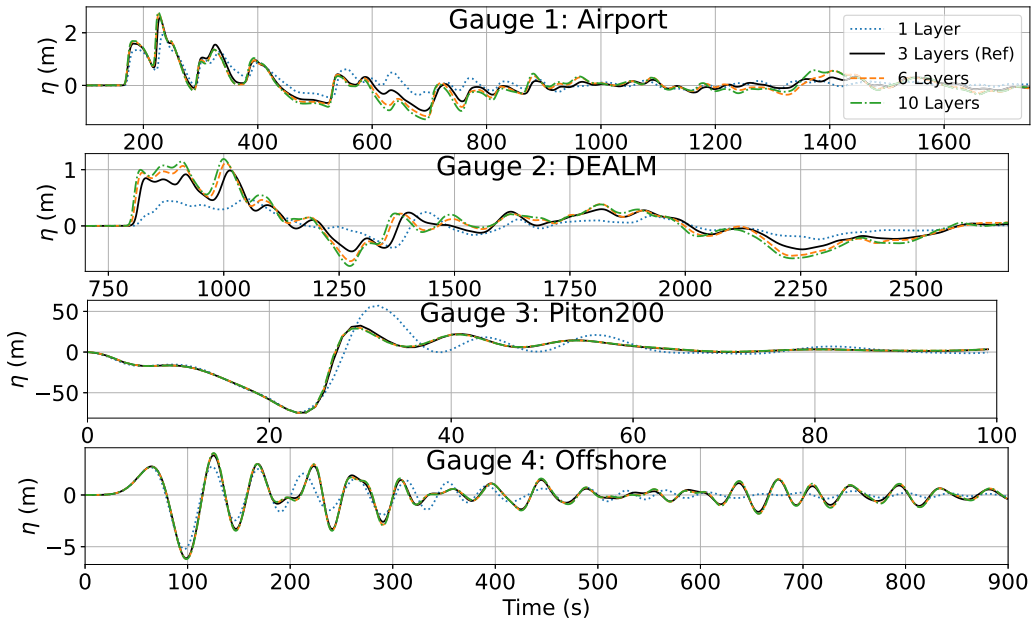


**Figure 10.** Sea surface elevation $\eta$ for different number of layers superposed with the reference case.

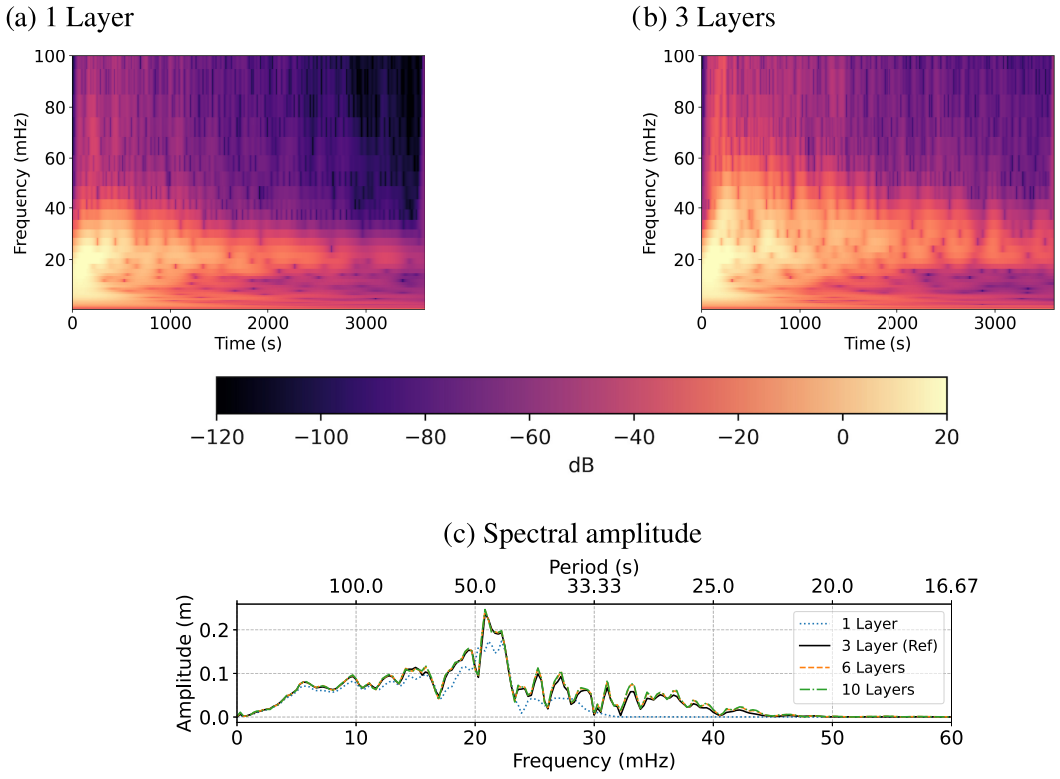


**Figure 11.** Spectrograms and spectral amplitude of the sea surface elevation signal at the gauge n° 4: Offshore.

on the simulated inundation areas is significant when looking locally around Petite Terre (Figs 13(b) and (d)). The inundation depth is much higher in the airport area due to lower topographic obstacles (Fig. 13(b)): up to 3 m of water is observed. Taking into account the new coastline in dashed black defined by the smooth bathymetry, the east coast is almost totally under a few meters of water with penetration length going from 50 to 100 m. As a result in our case, a low quality bathymetry may overestimate by up to 2 m the maximum water height inland and by 500 m the penetration length (airport location). The high relief located on the east coast of Petite Terre drops from 10 to 3 m approximately due to the smoothing process.

Notably, the effect of the bathymetry strongly depends on the location and time. For example, the maximum positive wave observed at $t \sim 30$ s is much higher with the 10 m grid at the Piton 200 gauge n° 3 whereas the first simulated waves are the same for all

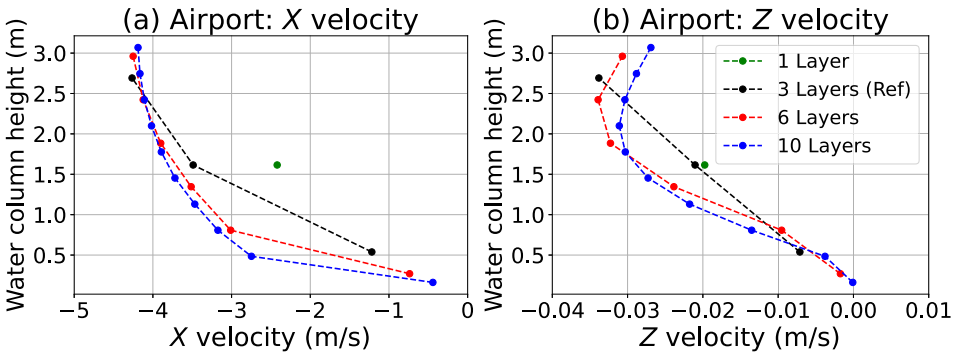


**Figure 12.** Vertical profiles at the airport gauge n° 1 of (a) the velocity in the $X$-direction and (b) the velocity in the $Z$-direction. The selected time for each simulation corresponds to $t_a + 75$ s, where $t_a = 165$ s is the arrival time of the first wave at the gauge. The vertical velocity profile is thus plotted at $t = 240$ s.

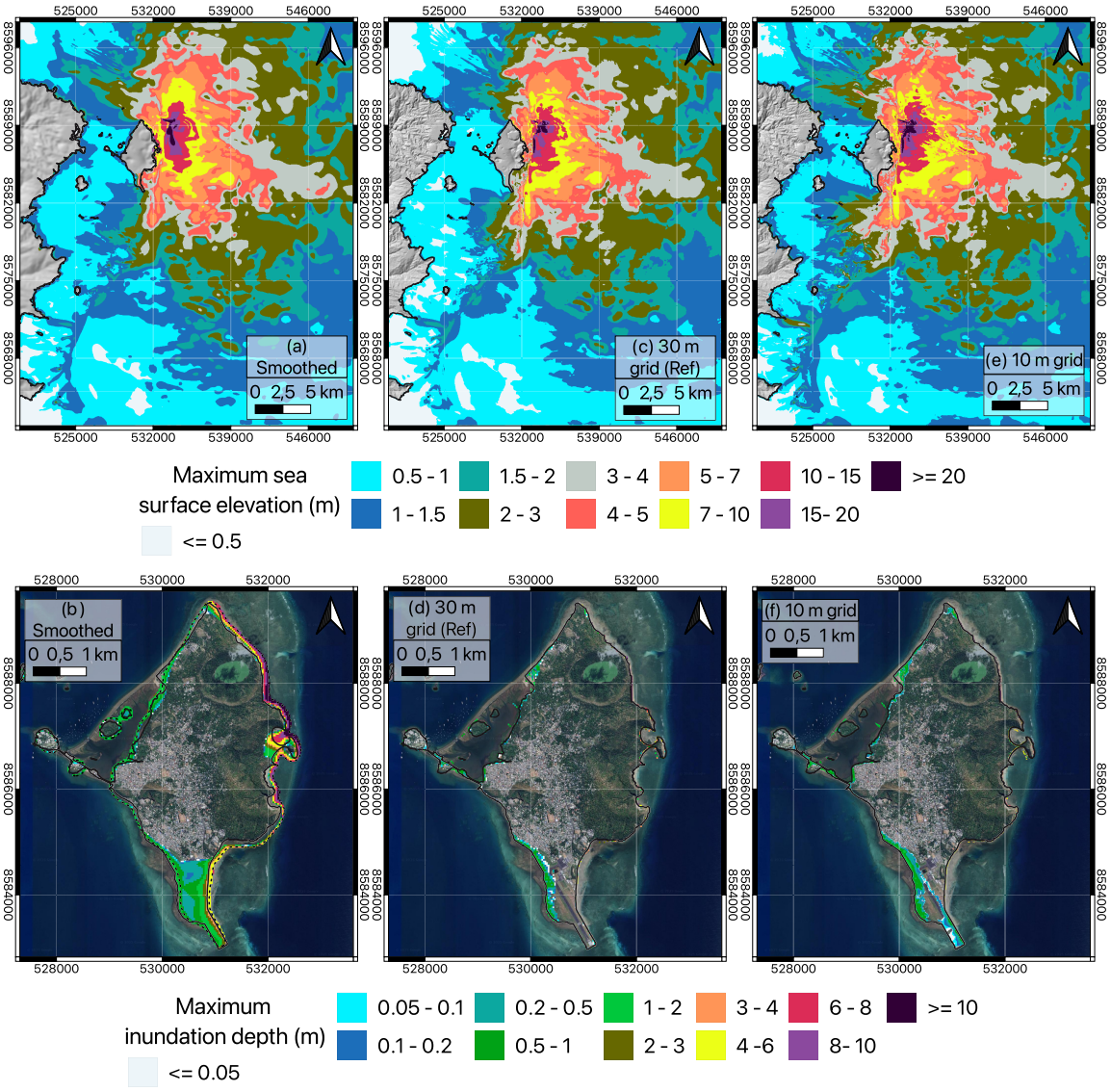


**Figure 13.** (a) Maximum sea surface elevation $\iota_{ij}$ (eq. 11) for a smoothed bathymetry on a 30 m grid. (b) Maximum inundation depth for a smoothed bathymetry on a 30 m grid. (c) Maximum sea surface elevation $\iota_{ij}$ (eq. 11) for a 30 m grid (reference case). (d) Maximum inundation depth for a 30 m grid (reference case). (e) Maximum sea surface elevation $\iota_{ij}$ (eq. 11) for a 10 m grid. (f) Maximum inundation depth for a 10 m grid. The dashed black line in panels (a) and (b) is the coastline calculated from the smoothed bathymetry while the full black line is the regular Histolitt coastline.

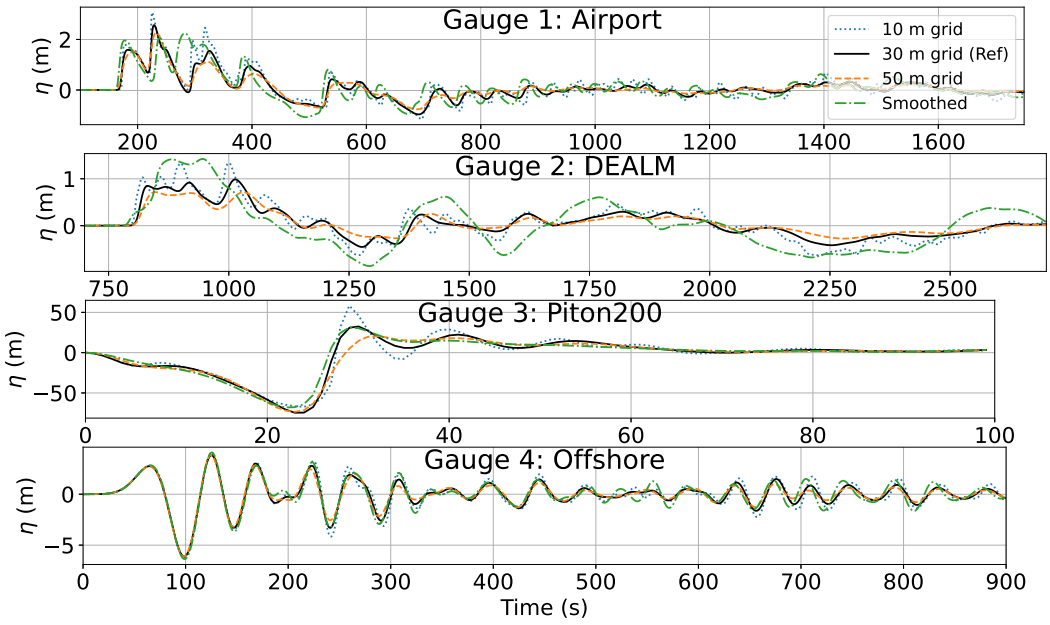


**Figure 14.** Sea surface elevation $\eta$ for the different bathymetry superposed with the reference case.

the resolutions (Fig. 14). On the contrary, the effect of bathymetry resolution is quite small at the offshore gauge n° 4, but is significant at the DEALM gauge n° 2. The wave form is much smoother on the smoothed bathymetry on gauges n° 1 and 2.

A higher grid resolution allows to capture higher frequencies as shown by the spectrogram and spectral amplitude at the offshore gauge n° 4 (Fig. 15). The typical wavelength associated with the wave train is $\lambda = \sqrt{gH}/f$, which gives $\lambda \simeq 5$ km for $H \simeq 1000$ m and $f \simeq 20$ mHz. A numerical grid resolution of a few tens of meters is thus enough to handle such large wavelengths. We conclude that the higher frequency content with increasing resolution is related to the source (landslide) dynamics. The resolution of heterogeneities in the landslide dynamic thanks to higher grid resolution are indeed at a much smaller scale than 5 km (Fig. S2 in the Supporting Information). However, the grid resolution and bathymetry quality seem to weakly affect the contours of the flowing mass at 50, 100 and 3600 s. Differences appear on the flow thicknesses, especially at the early times 50 and 100 s.

Interestingly, a very long period oscillation $T \simeq 600$ s is observed at the airport gauge n° 1 (spectral amplitude of Fig. S9 in the Supporting Information). This period corresponds to the typical period of a seiche that would go back and forth within the channel between north west of Petite Terre and Grande Terre, west of the airport gauge. Analytical formulas give a seiche period of $T_s = 2L/\sqrt{gH}$ in a closed rectangular basin of depth $H$ (Magdalena *et al.* 2020). In our case, the channel width is $L \simeq 4$ km and the water depth $H \simeq 15$ m, leading to $T_s \simeq 650$ s. Only the multilayer simulations capture this frequency well.

## 7 LANDSLIDE RHEOLOGY, FRICTION PARAMETERS AND TIDE EFFECTS

### 7.1 Impact of landslide dynamics on the water waves

Despite lots of work, uncertainties still remain on the physical understanding of submarine landslide dynamics and associated parameters (Delannay *et al.* 2017; Roger *et al.* 2024). We will identify here which of these parameters mostly influence the simulated tsunami wave. The tsunami waveform is known to depend on the thickness distribution and velocity of the landslide, which in turn depend on the landslide rheology and associated friction coefficients. Figs 20 and S4 (Supporting Information) illustrate that: the mass velocity and runout distance obviously increase when lowering the friction coefficient $\mu(I)$, i.e. with decreasing friction angle $\delta_1$ and grain diameter $d$, as shown by eq. (6). The Pouliquen friction law (eq. (5)) gives a similar final deposit compared to the $\mu(I)$ rheology. The same conclusion holds for the solid volume fraction $\Phi = 0.6$ that gives a similar final deposit compared to the reference case with $\Phi = 0.8$. For all simulations, the front of the deposit contains the largest amount of mass with thicknesses ranging from 15 m up to 40 m. The final runout, area, maximum thickness are collected in Table A1. The case $\delta_1 = 3°$ leads to notably higher thicknesses on the front and therefore less mass left behind.

The maximum sea surface elevation (Figs A7 and A8) and the waveform at the gauge (Figs S6 and S7 in the Supporting Information) only slightly depend on the grain diameter and on the type of friction law. However, the associated landslide deposit are quite different in Fig. 20. On the contrary, the maximum sea surface elevation significantly depends on the values of the friction coefficients that have been tested: $\delta_1 = 3°$ and $\delta_1 = 11°$ (Fig. 16). The maximum landslide velocities from Fig. S3 (Supporting Information) significantly differ between the $\delta_1 = 3°$ and $\delta_1 = 11°$ cases while they appear to be closer when changing the grain diameter $d$ or the rheological law. Biggest differences in the maximum sea surface elevation are clearly found when comparing $\delta_1 = 3°$ and $\delta_1 = 11°$ simulations (Fig. A5). The solid volume fraction value also has a high impact on the maximum sea surface elevation (Fig. 17), despite a similar final deposit for $\Phi = 0.6$ compared to the reference case (Fig. 20). We note that increasing the solid volume fraction reduces the density ratio $r$ which causes a higher gravity force $(1 - r)g$ for the landslide in the model. This is consistent with the observed maximum sea surface elevation in Fig. 17 where the solid volume fraction $\Phi = 0.6$ leads to higher waves, more concentrated around the landslide source, compared to the case $\Phi = 0.8$. The high impact

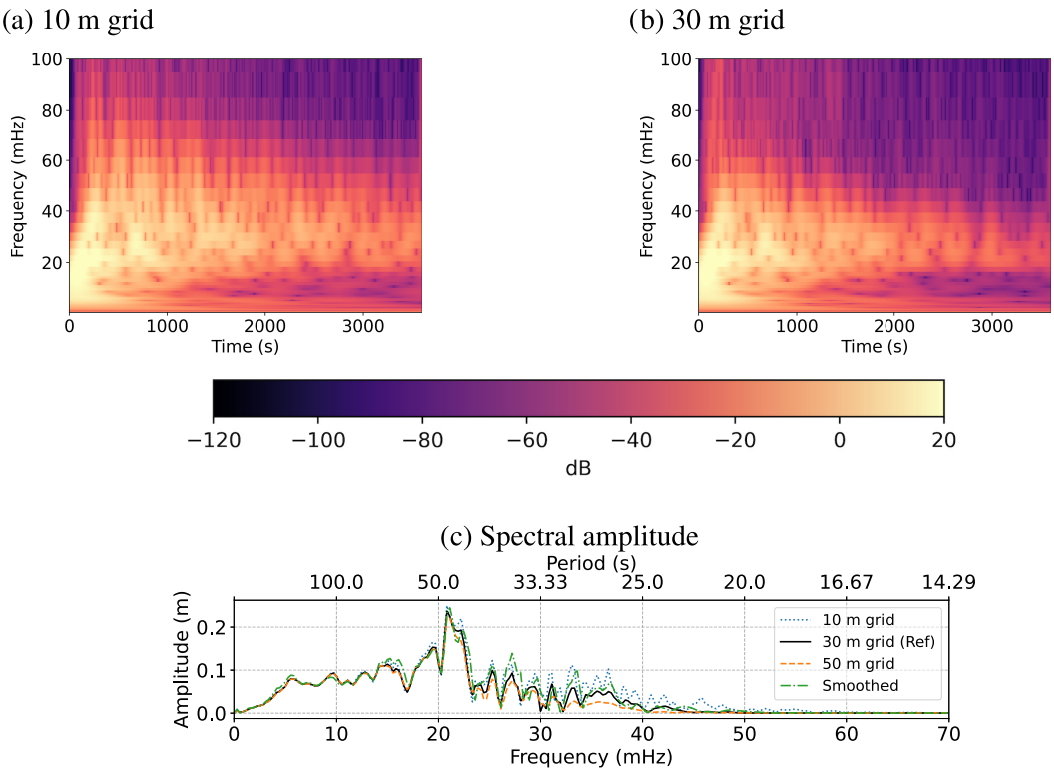


**Figure 15.** Spectrograms and spectral amplitude of the sea surface elevation signal at the gauge n° 4: Offshore.

of the solid volume fraction $\Phi$ suggests that using more complex and realistic rheology including dilatancy ($\mu(I)$, $\Phi(I)$) would significantly affect the results (Iverson & George 2014; Bouchut *et al.* 2016, 2025). The higher impact of both the friction angles and the solid volume fraction on the simulated waves is attributed to the early landslide dynamics. Fig. A6 shows that the landslide thickness (resp. landslide velocity) from the simulations with $\delta_1 = 3°$, $\delta_1 = 11°$ and $\Phi = 0.6$ differ from the rest of the simulations in the first 50 s (resp. 20 s). The impact of the friction angle and solid volume fraction is also observed on the gauge data in Figs 18 and 19. More gauge data related to landslide parameters are given in Appendix D and the Supporting Information. The inundation pattern looks similar for all the landslide parameters except when comparing $\delta_1 = 3°$ and $\delta_1 = 11°$ (Figs 16, A7, A8(b), (d)) and when comparing $\Phi = 0.6$ and $\Phi = 0.8$ (Figs 17(b) and (d)). In particular, for $\delta_1 = 11°$, tsunami waves inundate less of the airport zone, which sees a maximum water height of around 0.4 m as opposed to 0.7 m for $\delta_1 = 3°$. The effect of the solid volume fraction is non-negligible on the inundation pattern as we observe less inundation for $\Phi = 0.6$.

### 7.2 Landslide/water and water/bottom friction analysis

We study here the effect of the Manning coefficient by comparing to a simulation with a constant manning coefficient ('Cst Manning' case). We also set the mass/water interface friction to 0 ('$m_f = 0$' case) and compare with the reference case ($m_f = 2 \times 10^{-5}$ m . s$^{-1}$). Values are specified in Table 1. The mass/water coefficient have a negligible effect on the water waves (Fig. S4c in the Supporting Information). The constant Manning coefficient leads to high differences compared to the spatialized Manning (reference case) on the generated waves: up to 90 per cent differences are observed. With no surprise, these differences are located inside the lagoon (Fig. S4a in the Supporting Information) since a higher Manning value is applied at the reef location for the reference (Fig. A2).

### 7.3 Tide effect

When adding 1 m to the water level, we observe that the waveform is similar but the water wave arrive slightly earlier (30 s) at the DEALM gauge n° 2 (Fig. S8 in the Supporting Information). This is consistent with a higher wave velocity $\sqrt{g\,H}$ when the water depth $H$ increases by 1 m. Note that on these figures, the sea surface elevation has been shifted (by $-1$ m) to match the hydrostatic zero of other simulations for comparison purposes. Unsurprisingly, the west coast of Petite Terre is largely impacted by a 1 m elevation of the initial water level: a larger part of west Petite Terre is under water and the water depth inland reaches 1 to 1.5 m in Fig. 21(b), especially south west around the aiprort. The reference (+0 m water) only gives around 0.5 m water depth inland.

## 8 CONCLUSION

In this work, we perform a sensitivity analysis using the multilayer code HySEA on a island-type bathymetry characterized by large relief variations. We quantify the impact of the different model parameters on the generated waves. Mayotte island is a relevant example due to the presence of the submarine shelf surrounding Petite and Grande Terre. In the studied cases, the tsunami waves are induced by a potential landslide of 200 millions of m$^3$ initiated 2.5 km offshore Mayotte island.

The main result of this paper is the strong impact of the vertical discretisation (through multiple layers in the water column) when

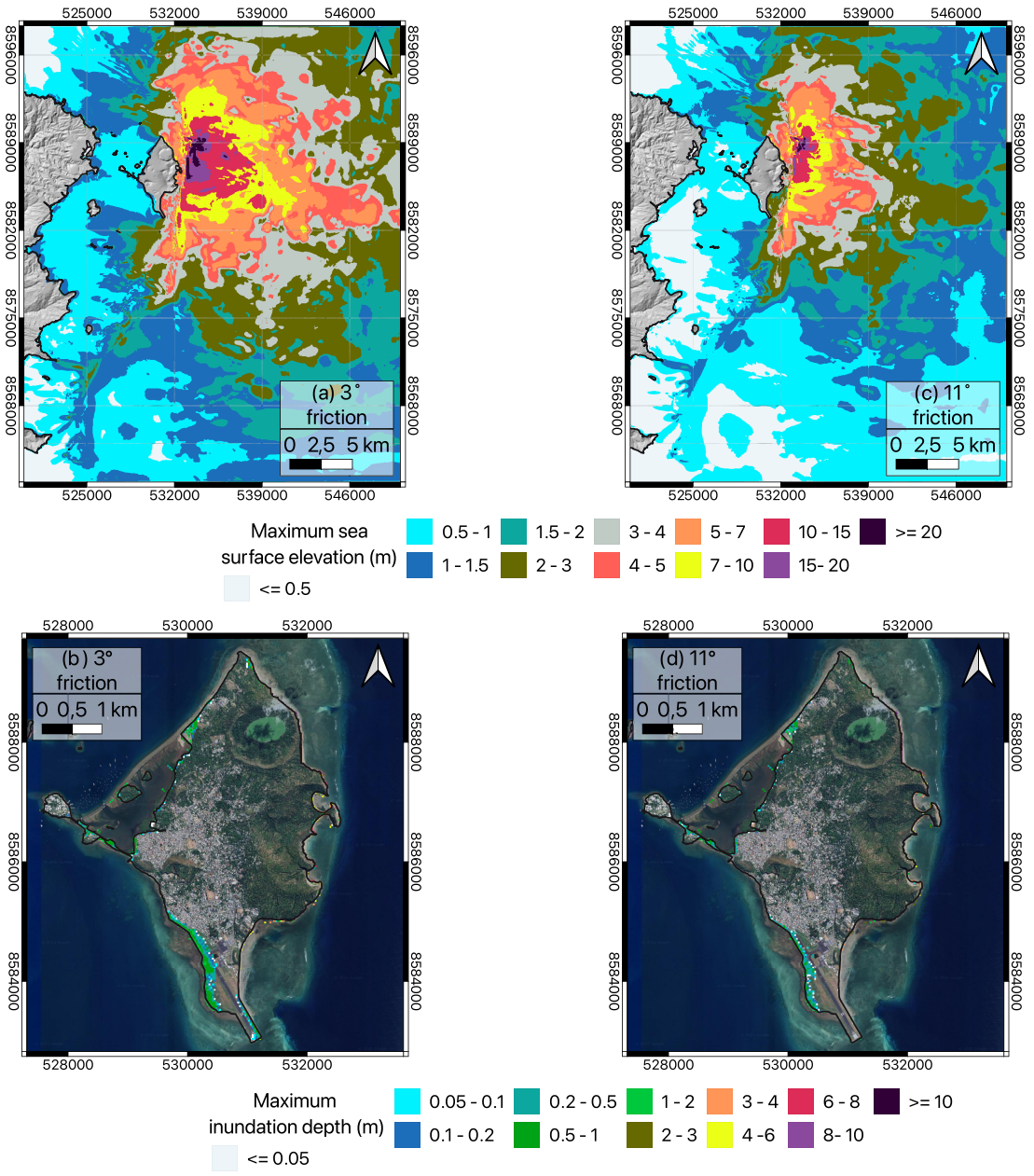


**Figure 16.** (a) Maximum sea surface elevation $\iota_{ij}$ (eq. 11) for a 3° friction angle. (b) Maximum inundation depth for a 3° friction angle. (c) Maximum sea surface elevation $\iota_{ij}$ (eq. 11) for a 11° friction angle. (d) Maximum inundation depth for a 11° friction angle.

the bathymetry presents obstacles and steep slopes. In the Mayotte configuration, the coral reef presents steep slopes with typical water depths ranging from 30 m (west of the reef) to 1000 m (east of the reef). The 1-layer (i.e. depth-averaged) model is much more sensitive to this bathymetric barrier. The 1-layer model thus predicts waves that are more attenuated inside the lagoon compared to multilayer models. On the west coast of Petite Terre including the crucial zone occupied by the airport, the 1-layer model underestimates the impact of the tsunami by a factor 2 compared to the 3-layer model. Adding more layers still increases the capacity of the tsunami waves to overcome the coral reef, even though the model roughly converges for 6 and 10 layers. The influence of increasing the number of layers is also visible in the landslide area. Above the landslide, the wave pattern simulated with the 1-layer model clearly reflects the landslide contours while multilayer models yield to a much smoother pattern, owing to the higher degree of freedom for the water motion in the vertical direction. We show that the numerical cost increases approximately linearly with the number of layers. In the particular case of Mayotte, involving strong topography variations, a good balance between accuracy and computational cost seems to be around 4 layers. We expect that this could be the case for other locations where bathymetry presents large variations and obstacles. Adding more layers allow to better capture the dispersion effects as detailed in Macías *et al.* (2021a), who recommend using 3 layers in their simulations over much simpler topographies. Our results illustrate the major importance of the dispersive effects (non-hydrostatic pressure and multilayer description) and the need to include them in the model, despite the increased computational

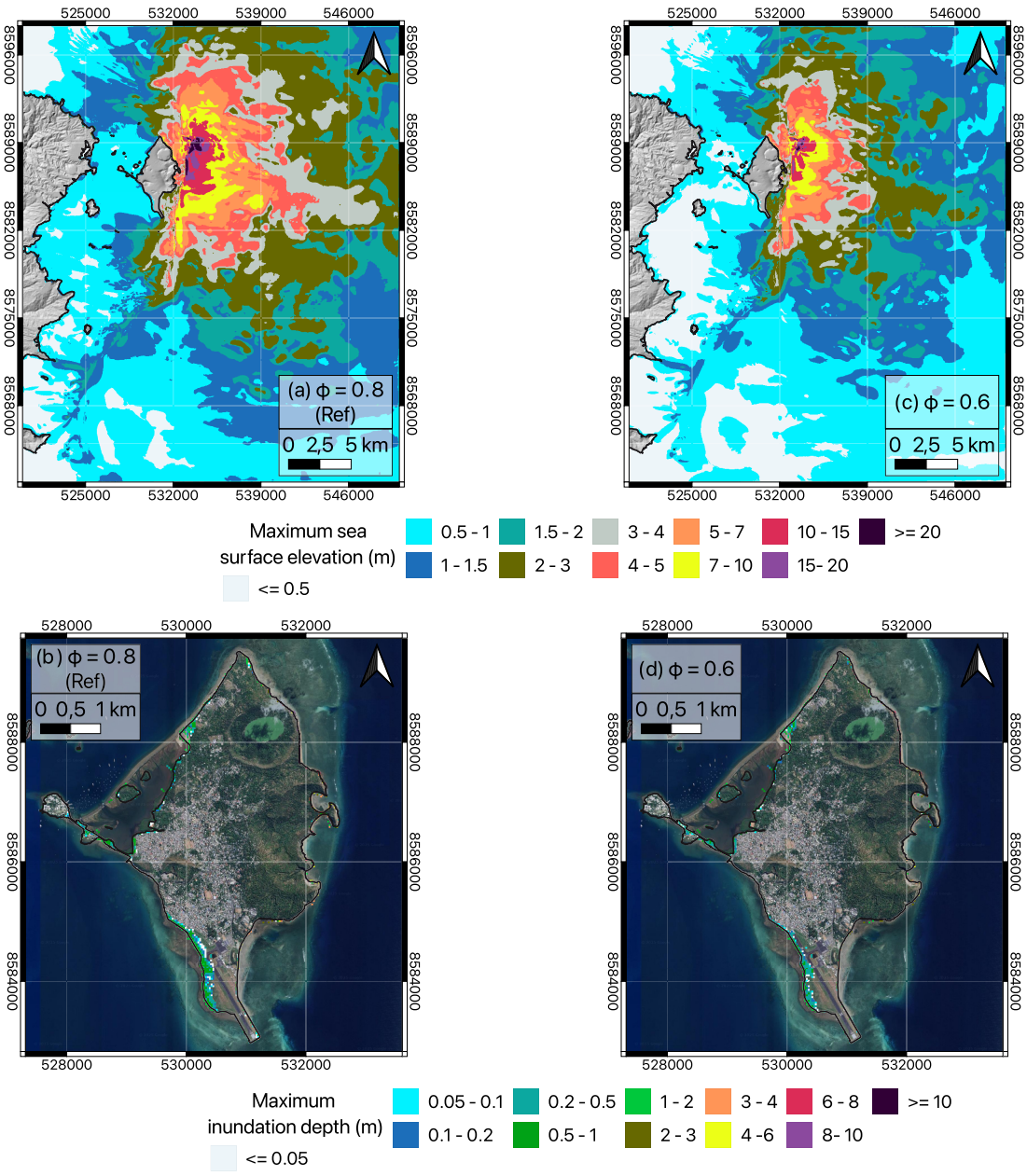


**Figure 17.** (a) Maximum sea surface elevation $\iota_{ij}$ (eq. 11) for a solid volume fraction $\Phi = 0.8$. (b) Maximum inundation depth for a solid volume fraction $\Phi = 0.8$. (c) Maximum sea surface elevation $\iota_{ij}$ (eq. 11) for a solid volume fraction $\Phi = 0.6$. (d) Maximum inundation depth for a solid volume fraction $\Phi = 0.6$.

cost, as recommended in Kirby *et al.* (2022). Interestingly, our multilayer simulations capture the seiche of period $T_s \simeq 600$ s observed at the aiport gauge n°1, seemingly related to the water waves going back and forth between the coasts of Grande and Petite Terre as observed and simulated in the Greenland fjords (Svennevig *et al.* 2024).

Our results show that for the finest 10 m grid used here, the water waves overcome the reef barrier more easily than on rougher grids (30 m grids). A smoothing of the bathymetry (representing low quality bathymetric data) leads to a complete different result at the airport location for example: the airport area is completely submerged by a few meters of water as opposed to all other simulations. This points out the crucial need for more oceanographic campaigns to acquire accurate and high-resolution bathymetric data in areas at risk. The major influence of the bathymetric data on landslide-tsunami simulations has also been highlighted by Svennevig *et al.* (2024).

The avalanche parameters also impact the amplitude and waveform of the tsunami, even locally, at Petite Terre for example. They obviously also change the landslide final deposit and mass distribution. While the form of the different friction laws investigated here and the grain diameter give quite similar water waves, the friction angles involved in these laws and the solid volume fraction have a large effect on both the landslide dynamics and tsunami waves. The impact on Petite Terre coastline is clearly visible: simulated wave amplitude doubles at the airport for $\delta_1 = 3°$ compared to $\delta_1 = 11°$. The landslide dynamic indeed affects the water waves generation and propagation.

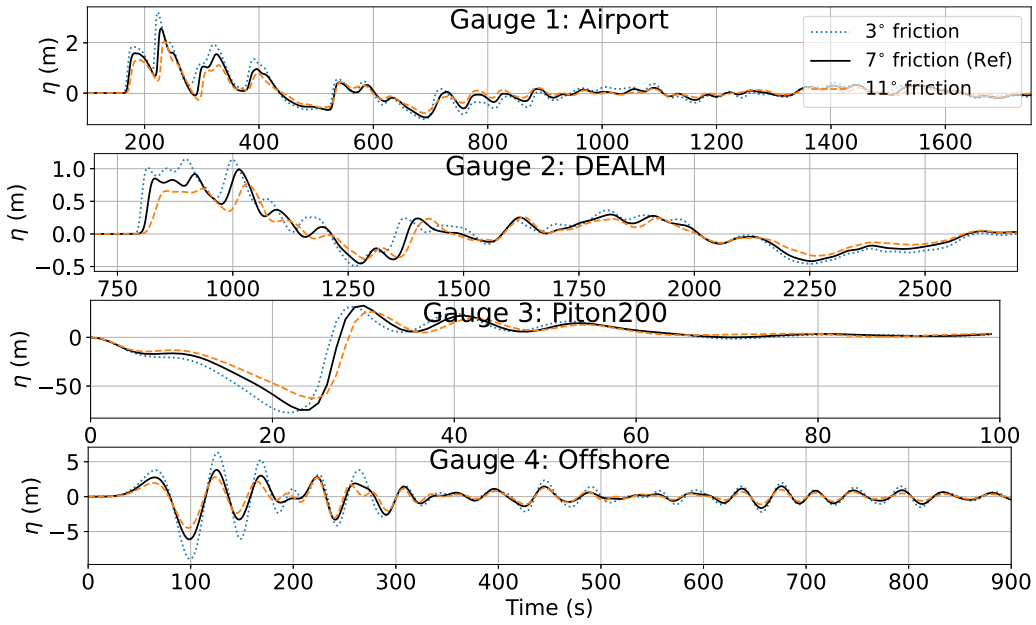


**Figure 18.** Sea surface elevation $\eta$ for the different sets of friction angles superposed with the reference case.

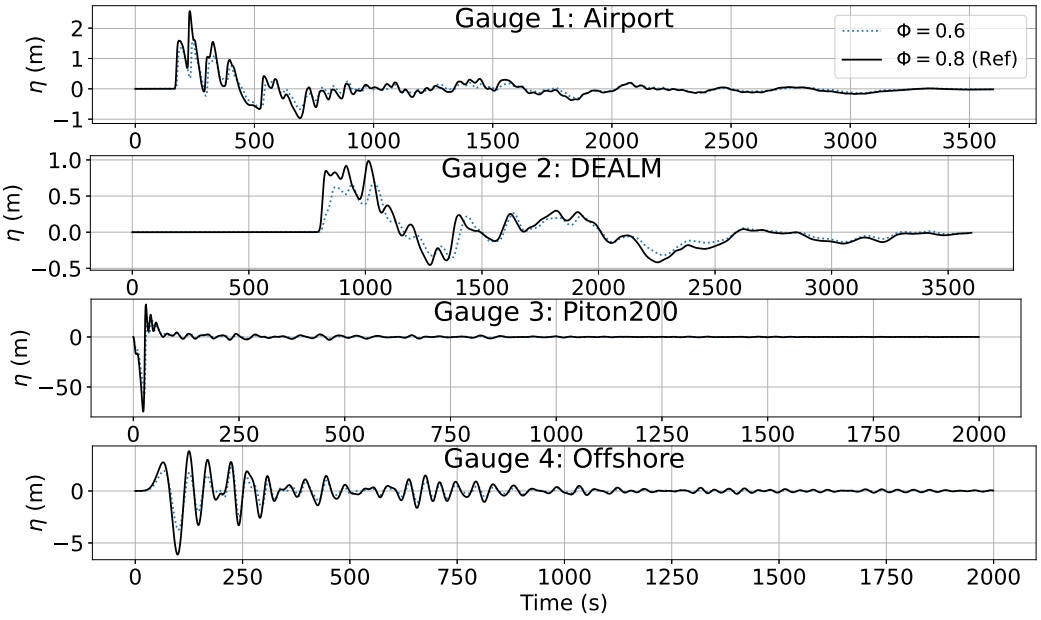


**Figure 19.** Sea surface elevation $\eta$ for a solid volume fraction $\Phi = 0.6$ superposed with the reference case.

While the mass/water friction coefficient is of small influence on the water waves, significant differences are observed when comparing the simulations with a constant and a variable Manning coefficient. Finally, a +1 m initial water level, potentially due to climate change, induces higher velocities, wider inundation distance, higher inundation depth and an earlier arrival time of around 30 s at gauge n°2 compared to the reference simulation.

Overall, the performed simulations allow us to roughly classify the parameters' influence on the maximum sea surface elevation and inundation pattern in the case of Mayotte from the more influential parameters to the least: (1) dispersion properties (non-hydrostatic versus hydrostatic and number of layers); (2) quality of bathymetric data, grid resolution, friction angles $\delta$s in the rheological laws and the solid volume fraction $\Phi$; (3) initial water level; (4) Manning coefficient; (5) type of rheological laws ($\mu(I)$ versus Coulomb); (6) mass/water friction and grain size related parameter $d$. The same classification applies locally at the Ponton gauge n°5 (Fig. A9).

Those considerations should be useful to develop modelling strategy in case of near field configuration for landslides induced

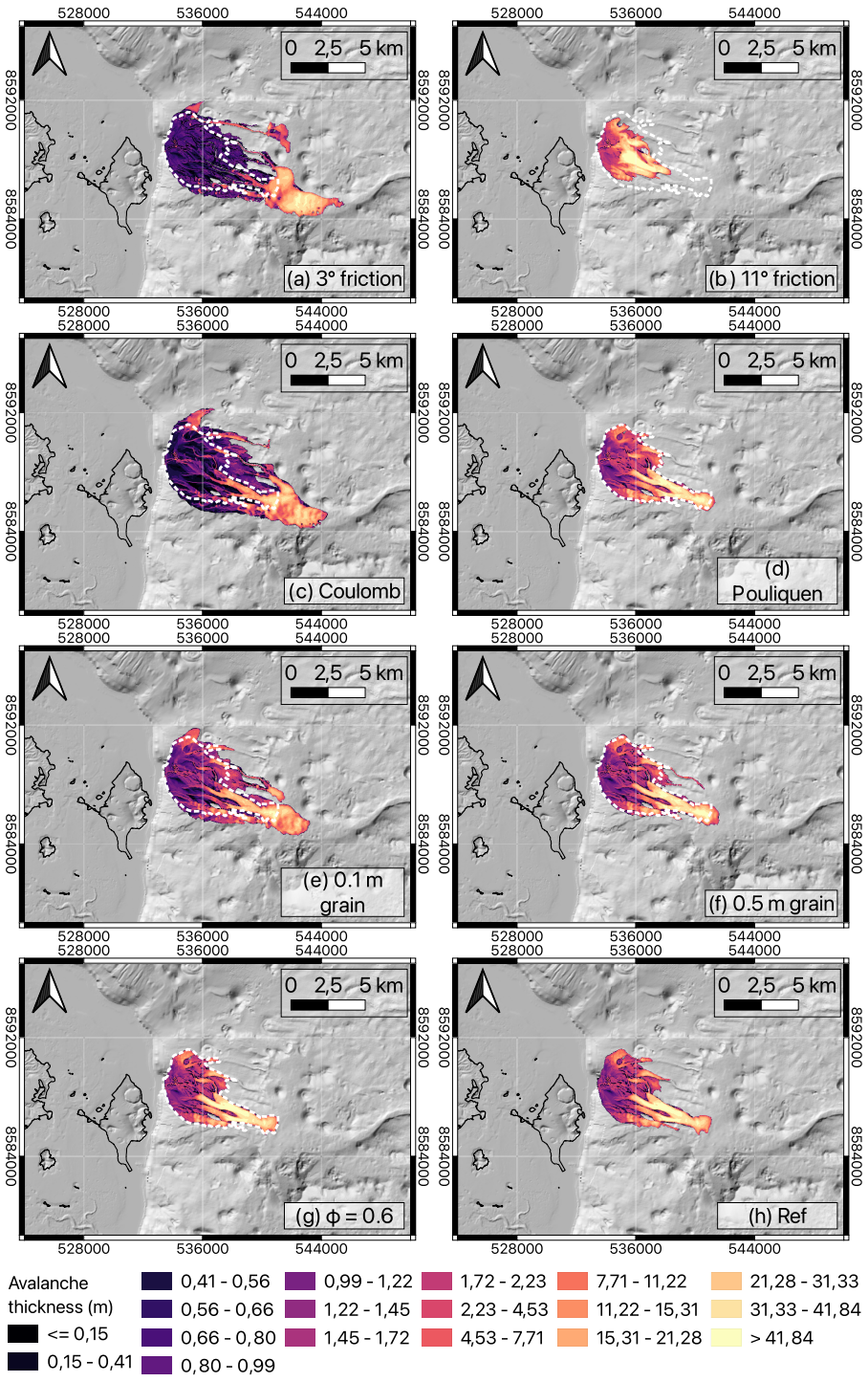


**Figure 20.** Final mass deposit for the different landslide parameters. White dashed lines indicate the final deposit for the reference case.

tsunamis in a complex bathymetry context. Future works may include a deeper insight into the influence of the parameters or features targeted by this study using statistical analysis. As pointed out in this paper, a proper convergence with even finer grids and/or an increasing number of layers would be interesting to carry out. Additional features related to a multilayer model, like vertical viscosity terms and breaking wave mechanisms, would also be worth investigating. This sensitivity analysis shows that the parameter uncertainties and model hypotheses may lead to a factor of approximately 2 on the simulated wave amplitude and velocity. Consequently, we observe about the same error on the penetration length and the inundation depth. Increasing the level of accuracy of landslide-tsunami models would have a significant impact on hazard assessment by providing actionable insights for evacuation planning, such as defining more precise safe zones and optimizing warning times.

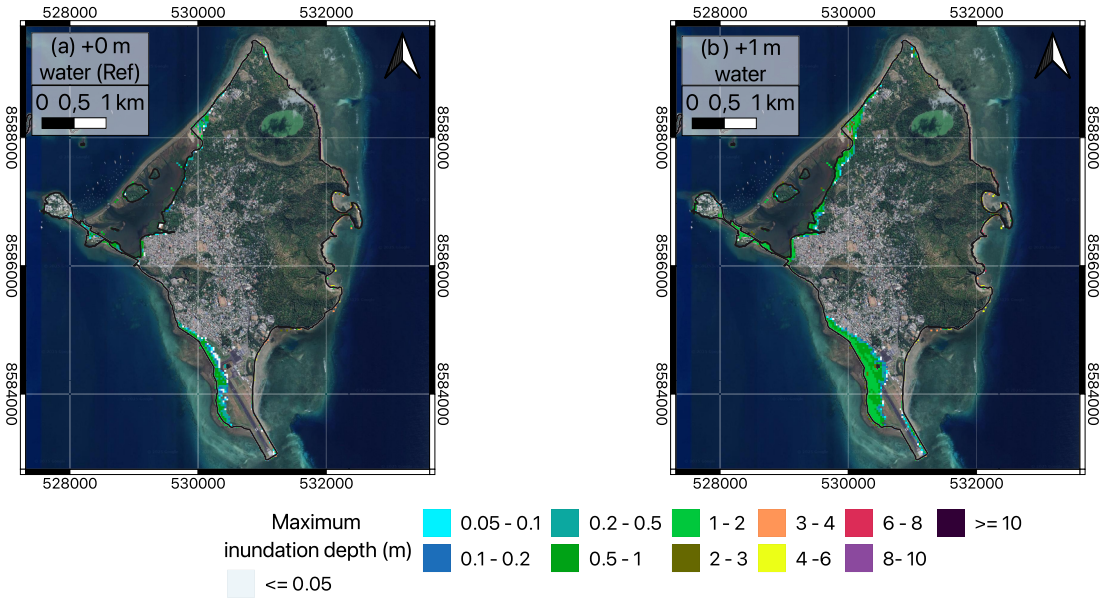


**Figure 21.** Maximum inundation depth: (a) +0 m water (reference case); (b) +1 m water.

## ACKNOWLEDGMENTS

AM, AM and FL are part of the DT-GEO project funded by the European Union's Horizon Europe research and innovation programme under grant agreement nº101058129. MJC was partially supported and funded by MCIN/AEI/10.13039/501100011033, by the "European Union NextGenerationEU/PRTR" through the grant PDC2022-133663-C21, by MCIN/AEI/10.13039/50110001103, by "ERDF A way of making Europe", by the "European Union" through the grant PID2022-137637NB-C21. EF-N was partially supported by the European Union—NextGeneration EU programme, by grant PID2022-137637NB-C22 funded by MCIN/AEI/10.13039/501100011033, the project "ERDF A way of making Europe", and by Junta de Andalucía research project ProyExcel_00525. ALF benefits from funds managed by the Agence Nationale de la Recherche under the France 2030 programme with the reference ANR-22-EXIR-0005, (PEPR Risques, IRiMa). ALF acknowledges the support from the Programme National de Télédétection Spatiale (PNTS, Grant PNTS-2022) and the LabEx UnivEarthS (ANR-10-LABX-0023 and ANR-18-IDEX-0001). RP and ALF benefits from fundings of the French Ministry for the Ecological Transition and BRGM.

## SUPPORTING INFORMATION

Supplementary data are available at *GJIRAS* online.

**Figure S1**. Maximum sea surface velocity for different numbers of layers and different grid resolutions.
**Figure S2**. Landslide dynamics (top panels) Reference case (30 m grid); (middle panels) Smoothed bathymetry; (bottom panels) 10 m grid. Dashed white lines correspond to the reference final deposit shape on the top panels. The dashed black line in the middle panels is the coastline calculated from the smoothed bathymetry while the full black line is the regular Histolitt coastline. The two coastlines seem almost merged when it is zoomed out.
**Figure S3**. Maximum velocity ($\mathrm{m.s^{-1}}$) reached by the landslide mass during its flow down the slope for the different landslide parameters.
**Figure S4**. Relative difference $\Delta_{ij}$ in maximum sea surface elevation given in percentage for different friction parameters: (a) Cst Manning (Simu 2) versus spatialized Manning (Simu 1, Reference case); (b) +1 m water (Simu 2) versus +0 m water (Simu 1, Reference case); (c) $m_f = 0$ (Simu 2) versus $m_f = 2 \times 10^{-5}$ (Simu 1, Reference case). Minimum and maximum differences are: a) −20 per cent up to 90 per cent; b) −33 per cent up to 100 per cent; c) −30 per cent up to 15 per cent.
**Figure S5**. Sea surface elevation $\eta$ for the hydrostatic (1 Layer) and non-hydrostatic simulations (1 Layer).
**Figure S6**. Gauge data for the different values of the grain diameter $d$.
**Figure S7**. Gauge data for simulations with different rheological laws for the landslide.
**Figure S8**. Gauge data for friction parameters and initial water level superposed with the reference case. The sea surface elevation has been shifted by −1 m to match the hydrostatic zero of other simulations for comparison purposes.
**Figure S9**. Spectral amplitude of the sea surface elevation signal at the gauge n°1: Airport.
**Figure S10**. Maximum sea surface elevation $\iota_{ij}$ without a breaking wave model (reference case) and with a breaking wave model.

Please note: Oxford University Press are not responsible for the content or functionality of any supporting materials supplied by the authors. Any queries (other than missing material) should be directed to the corresponding author for the article.

## DATA AVAILABILITY

The simulations are performed with the code multilayer HySEA developed by the EDANYA group of Malaga University in Spain. The continuous equations and the associated numerical discretization are described in this paper. The reader is referred to the references cited in this paper and to the website available at https://edanya.uma.es/hysea/ for more details about the HySEA numerical codes. The input parameters used for the simulations are all mentioned in the paper. Bathymetric data are sourced and they may be distributed on demand. The maps are produced with

the QGis open-source software (https://qgis.org) and homemade Python scripts for gauge data. The authors are available to provide any information needed to reproduce the results.

## REFERENCES


Abadie, S., Morichon, D., Grilli, S. & Glockner, S., 2010. Numerical simulation of waves generated by landslides using a multiple-fluid navier–stokes model, *Coast. Eng.,* **57,** 779–794.

Allgeyer, S. *et al.*, 2019. Numerical approximation of the 3d hydrostatic navier–stokes system with free surface, *ESAIM: Math. Model. Numer. Anal.,* **53,** 1981–2024.

Andreotti, B., Pouliquen, O. & Forterre, Y., 2013. *Granular Media: Between Fluid and Solid,* Cambridge University Press, Cambridge.

Aïssiouene, N., Bristeau, M.O., Godlewski, E., Mangeney, A., Madroñal, C.P. & Sainte-Marie, J., 2020. A two-dimensional method for a family of dispersive shallow water models, *SMAI J. Comput. Math.,* **6,** 187–226.

Audusse, E., Bouchut, F., Bristeau, M.O., Klein, R. & Perthame, B., 2006. A fast and stable well-balanced scheme with hydrostatic reconstruction for shallow water flows, *SIAM Journal on Scientific Computing* **25,** 2050–2065.

Behrens, J. & Dias, F., 2015. New computational methods in tsunami science, *Phil. Trans. R. Soc. A: Math. Phys. Eng. Sci.,* **373,** doi:10.1098/RSTA.2014.0382.

Bonaventura, L., Fernández-Nieto, E.D., Garres-Díaz, J. & Narbona-Reina, G., 2018. Multilayer shallow water models with locally variable number of layers and semi-implicit time discretization, *J. Comput. Phys.,* **364,** 209–234.

Bonilauri, E.M., Aaron, C., Cerminara, M., Paris, R., Ongaro, T.E., Calusi, B., Mangione, D. & Harris, A.J.L., 2024. Inundation and evacuation of shoreline populations during landslide-triggered tsunami: An integrated numerical and statistical hazard assessment, *Nat. Hazards Earth Syst. Sci.* **24,** 3789–3813.

Bouchut, F., Fernández-Nieto, E.D., Mangeney, A. & Narbona-Reina, G., 2016. A two-phase two-layer model for fluidized granular flows with dilatancy effects, *J. Fluid Mech.,* **801,** 166–221.

Bouchut, F., Drach, E., Fernández-Nieto, E.D., Mangeney, A. & Narbona-Reina, G., 2025. A series of two-phase models for grain–fluid flows with dilatancy, *J. Fluid Mech.,* **1008,** A43. doi:10.1017/jfm.2025.131.

Brunet, M., Moretti, L., Friant, A.L., Mangeney, A., Nieto, E.D.F. & Bouchut, F., 2017. Numerical simulation of the 30–45 ka debris avalanche flow of montagne pelée volcano, martinique: from volcano flank collapse to submarine emplacement, *Nat. Hazards,* **87,** 1189–1222.

Bunya, S. *et al.*, 2010. A high-resolution coupled riverine flow, tide, wind, wind wave, and storm surge model for southern louisiana and mississippi. Part I: Model development and validation, *Mon. Weather Rev.,* **138,** 345–377.

Cannat, M., Mangeney, A., Ondréas, H., Fouquet, Y. & Normand, A., 2013. High-resolution bathymetry reveals contrasting landslide activity shaping the walls of the mid-atlantic ridge axial valley, *Geochem. Geophys. Geosyst.,* **14,** 996–1011.

Castro, M.J. & Parés, C., 2020. Well-balanced high-order methods for systems of balance laws, *Continuum Mechanics, Applied Mathematics and Scientific Computing: Godunov's Legacy: A Liber Amicorum to Professor Godunov,* Springer, pp. 69–75.

Castro, M.J., Ferreiro, A.M.F., García-Rodríguez, J.A., González-Vida, J.M., MacíAs, J., Parés, C. & Vázquez-Cendón, M.E., 2005. The numerical treatment of wet/dry fronts in shallow flows: application to one-layer and two-layer systems, *Math. Comput. Model.,* **42,** 419–439.

Castro, M.J., Ortega, S., de la Asunción, M., Mantas, J.M. & Gallardo, J.M., 2011. Gpu computing for shallow water flow simulation based on finite volume schemes, *Comptes Rendus Mécanique,* **339,** 165–184.

Castro-Diaz, M.J. & Fernandez-Nieto, E.D., 2012. A class of computationally fast first order finite volume solvers: Pvm methods, *SIAM Journal on Scientific Computing,* **34,** doi:10.1137/100795280.

Chen, Q., 2006. Fully nonlinear boussinesq-type equations for waves and currents over porous beds, *J. Eng. Mech.,* **132,** 220–230.

Crosta, G.B., Imposimato, S. & Roddeman, D., 2016. Landslide spreading, impulse water waves and modelling of the vajont rockslide, *Rock Mech. Rock Eng.,* **49,** 2413–2436.

Delannay, R., Valance, A., Mangeney, A., Roche, O. & Richard, P., 2017. Granular and particle-laden flows: from laboratory experiments to field observations, *J. Phys. D: Appl. Phys.,* **50,** 053 001. doi:10.1088/1361-6463/50/5/053001.

Delgado-Sánchez, J.M., Bouchut, F., Fernández-Nieto, E.D., Mangeney, A. & Narbona-Reina, G., 2020. A two-layer shallow flow model with two axes of integration, well-balanced discretization and application to submarine avalanches, *J. Comput. Phys.,* **406,** 109 186. doi:10.1016/J.JCP.2019.109186.

Escalante, C., de Luna, T.M. & Castro, M.J., 2018. Non-hydrostatic pressure shallow flows: Gpu implementation using finite volume and finite difference scheme, *Appl. Math. Comput.,* **338,** 631–659.

Escalante, C., Dumbser, M. & Castro, M.J., 2019. An efficient hyperbolic relaxation system for dispersive non-hydrostatic water waves and its solution with high order discontinuous galerkin schemes, *J. Comput. Phys.,* **394,** 385–416.

Escalante, C., Fernández-Nieto, E.D., Garres-Díaz, J. & Mangeney, A., 2023. Multilayer shallow model for dry granular flows with a weakly non-hydrostatic pressure, *J. Sci. Comput.,* **96,** 1–50.

Esposti Ongaro, T. *et al.*, 2025. Modeling and simulation of volcanic mass movements and induced tsunamis at Stromboli volcano (Aeolian archipelago, Tyrrhenian sea, Italy), *Front. Earth Sci.,* **13,** 1548 961. doi:10.3389/feart.2025.1548961.

Fernández-Nieto, E.D., Bouchut, F., Bresch, D., Díaz, M.J.C. & Mangeney, A., 2008. A new savage–hutter type model for submarine avalanches and generated tsunami, *J. Comput. Phys.,* **227,** 7720–7754.

Fernández-Nieto, E.D., Garres-Díaz, J., Mangeney, A. & Narbona-Reina, G., 2016. A multilayer shallow model for dry granular flows with the -rheology: application to granular collapse on erodible beds, *J. Fluid Mech.,* **798,** 643–681.

Feuillet, N. *et al.*, 2021. Birth of a large volcanic edifice offshore Mayotte via lithosphere-scale dyke intrusion, *Nat. Geosci.,* **14,** 787–795.

Garres-Díaz, J., Bouchut, F., Fernández-Nieto, E.D., Mangeney, A. & Narbona-Reina, G., 2020. Multilayer models for shallow two-phase debris flows with dilatancy effects, *J. Comput. Phys.,* **419,** 109 699. doi:10.1016/J.JCP.2020.109699.

Garres-Díaz, J., Fernández-Nieto, E.D., Mangeney, A. & de Luna, T.M., 2021. A weakly non-hydrostatic shallow model for dry granular flows, *J. Sci. Comput.,* **86,** 1–35.

Gonzalez-Vida, J.M., Macías, J., Castro, M.J., Sanchez-Linares, C., Asuncion, M.D.L., Ortega-Acosta, S. & Arcas, D., 2019. The lituya bay landslide-generated mega-tsunami—numerical simulation and sensitivity analysis, *Nat. Hazards Earth Syst. Sci.,* **19,** 369–388.

Greve, R. & Hutter, K., 1993. Motion of a granular avalanche in a convex and concave curved chute: experiments and theoretical predictions, *Phil. Trans. R. Soc. London Ser. A: Phys. Eng. Sci.,* **342,** 573–600.

Grezio, A. *et al.*, 2017. Probabilistic tsunami hazard analysis: Multiple sources and global applications, *Rev. Geophys.,* **55,** 1158–1198.

Grilli, S.T., Vogelmann, S. & Watts, P., 2002. Development of a 3-D numerical wave tank for modelling tsunami generation by underwater landslides, *Eng. Anal. Boundary Elements,* **26,** 301–313.

Grilli, S.T., Shelby, M., Kimmoun, O., Dupont, G., Nicolsky, D., Ma, G., Kirby, J.T. & Shi, F., 2017. Modeling coastal tsunami hazard from submarine mass failures: effect of slide rheology, experimental validation, and case studies off the us east coast, *Nat. Hazards,* **86,** 353–391.

Guan, X. & Shi, H., 2023. Translational momentum of deformable submarine landslides off a slope, *J. Fluid Mech.,* **960,** doi:10.1017/JFM.2023.177.

Gueugneau, V. *et al.*, 2021. Synthetic benchmarking of concentrated pyroclastic current models, *Bull. Volcanol.,* **83,** 75. doi:10.1007/S00445-021-01491-Y.

Gylfadóttir, S.S., Kim, J., Helgason, J.K., Brynjólfsson, S., Ármann, Höskuldsson, Jóhannesson, T., Harbitz, C.B. & Løvholt, F., 2017. The 2014 lake askja rockslide-induced tsunami: Optimization of numerical

tsunami model using observed data, *J. Geophys. Res.: Oceans,* **122,** 4110–4122.
Harbitz, C.B., 1992. Model simulations of tsunamis generated by the storegga slides, *Mar. Geol.,* **105,** 1–21.
Harbitz, C.B., Løvholt, F. & Bungum, H., 2014. Submarine landslide tsunamis: How extreme and how likely?, *Nat. Hazards,* **72,** 1341–1374.
Hare, R., Eakins, B. & Amante, C., 2011. Modelling bathymetric uncertainty, *Int. Hydrogr. Rev,* **6**.
Heinrich, P., Guibourg, S., Mangeney, A. & Roche, R., 1999. Numerical modeling of a landslide-generated tsunami following a potential explosion of the montserrat volcano, *Phgs. Chem. Earrh (A),* **24,** 163–168.
Intergovernmental Panel on Climate Change (IPCC), 2023. Climate change 2022–impacts, adaptation and vulnerability: Working group ii contribution to the sixth assessment report of the intergovernmental panel on climate change, in *Climate Change 2022–Impacts, Adaptation and Vulnerability,* Cambridge University Press, doi:10.1017/9781009325844.
Iverson, R.M. & George, D.L., 2014. A depth-averaged debris-flow model that includes the effects of evolving dilatancy. I. Physical basis, *Proc. R. Soc. A: Math. Phys. Eng. Sci.,* **470**(2170), 20 130 819. doi:10.1098/rspa.2013.0819.
Jop, P., Forterre, Y. & Pouliquen, O., 2006. A constitutive law for dense granular flows, *Nature,* **441,** 727–730.
Kennedy, A.B., Kirby, J.T., Chen, Q. & Dalrymple, R.A., 2001. Boussinesq-type equations with improved nonlinear performance, *Wave Motion,* **33,** 225–243.
Kirby, J.T., Wei, G., Chen, Q., Kennedy, A.B. & Dalrymple, R.A., 1998. Funwave 1.0: Fully nonlinear boussinesq wave model - documentation and user's manual, Research Report NO. CACR-98-06
Kirby, J.T. *et al.*, 2022. Validation and inter-comparison of models for landslide tsunami generation, *Ocean Modelling,* **170,** 101 943. doi:10.1016/J.OCEMOD.2021.101943.
Lane, E.M., Mountjoy, J.J., Power, W.L. & Mueller, C., 2016. Probabilistic hazard of tsunamis generated by submarine landslides in the cook strait canyon (new zealand), *Pure Appl. Geophys.,* **173,** 3757–3774, doi:10.1007/978-3-319-55480-8_6.
Lemoine, A. *et al.*, 2020a. The 2018–2019 seismo-volcanic crisis east of mayotte, comoros islands: seismicity and ground deformation markers of an exceptional submarine eruption, *Geophys. J. Int.,* **223,** 22–44.
Lemoine, A. *et al.* , 2020b. Scénarios d'impact de tsunamis pour Mayotte, BRGM final report RP-69869-FR.
Leone, F., Lavigne, F., Paris, R., Denain, J.C. & Vinet, F., 2011. A spatial analysis of the december 26th, 2004 tsunami-induced damages: Lessons learned for a better risk assessment integrating buildings vulnerability, *Appl. Geogr.,* **31,** 363–375.
Linares-Sánchez, C., Castro-Diaz, M.J. & Gonzalez-Vida, J.M., 2011, Simulación numérica de tsunamis generados por avalanchas submarinas: aplicación al caso de lituya-bay, *Trabajo Fin de Máster, Universidad de Málaga*.
Liu, P.L.-F., Wu, T.-R., Raichlen, F., Synolakis, C.E. & Borrero, J.C., 2005. Runup and rundown generated by three-dimensional sliding masses, *J. Fluid Mech.,* **536,** 107–144.
Lucas, A., Mangeney, A. & Ampuero, J.P., 2014. Frictional velocity-weakening in landslides on earth and on other planetary bodies, *Nat. Commun.,* **5,** 1–9.
Løvholt, F., Glimsdal, S. & Harbitz, C.B., 2020. On the landslide tsunami uncertainty and hazard, *Landslides,* **17,** 2301–2315.
Løvholt, F., Glimsdal, S. & Harbitz, C.B., 2025. Tsunami hazard from subaerial landslides, *Probabilistic Tsunami Hazard and Risk Analysis: Towards Disaster Risk Reduction and Resilience,* pp. 289–301, Elsevier, doi:10.1016/B978-0-443-18987-6.00010-5.
Lynett, P. & Liu, P.L., 2002. A numerical study of submarine–landslide–generated waves and run–up, *Proc. R. Soc. London Ser. A: Math. Phys. Eng. Sci.,* **458,** 2885–2910.
Ma, G., Kirby, J.T., Hsu, T.J. & Shi, F., 2015. A two-layer granular landslide model for tsunami wave generation: Theory and computation, *Ocean Modelling,* **93,** 40–55.
Macías, J., Vázquez, J.T., Fernández-Salas, L.M., González-Vida, J.M., Bárcenas, P., Castro, M.J., del Río, V.D. & Alonso, B., 2015. The al-borani submarine landslide and associated tsunami. a modelling approach, *Mar. Geol.,* **361,** 79–95.
Macías, J., Escalante, C., Castro, M.J., González-Vida, J.M. & Ortega, S., 2017, Hysea model landslide benchmarking results, *NTHMP Landslide Benchmark Workshop*.
Macías, J., Castro, M.J., Ortega, S. & González-Vida, J.M., 2020. Performance assessment of tsunami-hysea model for nthmp tsunami currents benchmarking. field cases, *Ocean Modelling,* **152,** 101 645. doi:10.1016/J.OCEMOD.2020.101645.
Macías, J., Escalante, C. & Castro, M.J., 2021a. Multilayer-hysea model validation for landslide-generated tsunamis-part 1: Rigid slides, *Nat. Hazards Earth Syst. Sci.,* **21,** doi:10.5194/nhess-21-775-2021.
Macías, J., Escalante, C. & Castro, M.J., 2021b. Multilayer-hysea model validation for landslide-generated tsunamis-part 2: Granular slides, *Nat. Hazards Earth Syst. Sci.,* **21,** doi:10.5194/nhess-21-791-2021.
Magdalena, I., Rif'atin, H.Q. & Matin, A.M.A., 2020. Analytical and numerical studies for seiches in a closed basin with bottom friction, *Theor. Appl. Mech. Lett.,* **10,** 429–437.
Mangeney, A., Heinrich, P., Rachel, R., Boudon, G. & Cheminée, J.L., 2000. Modeling of debris avalanche and generated water waves: Application to real and potential events in montserrat, *Phys. Chem. Earth (A),* **25,** 741–745.
Mangeney, A., Bouchut, F., Thomas, N., Vilotte, J.P. & Bristeau, M.O., 2007. Numerical modelling of self-channeling granular flows and of their levee-channel deposits, *J. geophys. Res.: Earth Surface,* **112,** 2017. doi:10.1029/2006JF000469.
Marras, S. & Mandli, K.T., 2021. Modelling and simulation of tsunami impact: a short review of recent advances and future challenges, *Geosciences,* **11**(1), 5. doi:10.3390/geosciences11010005.
Martin, H.A. *et al.*, 2023. Numerical simulations of granular dam break: comparison between discrete element, navier-stokes, and thin-layer models, *Phys. Rev. E,* **108,** 054 902. doi:10.1103/PHYSREVE.108.054902/FIGURES/17/MEDIUM.
Masson, D.G., Harbitz, C.B., Wynn, R.B., Pedersen, G. & Løvholt, F., 2006. Submarine landslides: processes, triggers and hazard prediction, *Phil. Trans. R. Soc. A: Math. Phys. Eng. Sci.,* **364,** 2009–2039.
Mathevet, T., Moine, N.L., Andréassian, V., Gupta, H. & Oudin, L., 2023. Multi-objective assessment of hydrological model performances using Nash–Sutcliffe and Kling–Gupta efficiencies on a worldwide large sample of watersheds, *C. R. Géosci.,* **355**(S1), 117–141.
Mercury, N. *et al.*, 2020. The 2018-2020 seismo-volcanic crisis, east of mayotte, comoros islands: in-depth study of poorly instrumented first months of crisis, *AGUFM,* **2020,** V040–0007.
Mercury, N., Lemoine, A., Doubre, C., Bertil, D., Woerd, J.V.D., Hoste-Colomer, R. & Battaglia, J., 2022. Onset of a submarine eruption east of mayotte, comoros archipelago: The first ten months seismicity of the seismo-volcanic sequence (2018–2019), *C. R. - Geosci.,* **354,** 105–136.
Mokhtarzadeh, G., Basirat, S., Bazargan, J. & Delavari, E., 2021. Impulse wave generation: A comparison of landslides of block and granular masses by coupled Lagrangian tracking using VOF over a set mesh, *Water Supply,* **22**(1), 510–526.
Mulia, I.E., Ueda, N., Miyoshi, T., Gusman, A.R. & Satake, K., 2022. Machine learning-based tsunami inundation prediction derived from offshore observations, *Nat. Commun.,* **13,** 1–14.
Neumann, B., Vafeidis, A.T., Zimmermann, J. & Nicholls, R.J., 2015. Future coastal population growth and exposure to sea-level rise and coastal flooding - a global assessment, *PLOS ONE,* **10,** e0118571. doi:10.1371/JOURNAL.PONE.0118571.
Ongaro, T.E. *et al.*, 2021. Modeling tsunamis generated by submarine landslides at stromboli volcano (aeolian islands, italy): A numerical benchmark study, *Front. Earth Sci.,* **9,** 628 652. doi:10.3389/FEART.2021.628652/BIBTEX.
Paris, A., Okal, E.A., Guérin, C., Heinrich, P., Schindelé, F. & Hébert, H., 2019. Numerical modeling of the june 17, 2017 landslide and tsunami events in karrat fjord, west greenland, *Pure appl. Geophys.,* **176,** 3035–3057.
Pedrosa-González, M.T., González-Vida, J.M., Galindo-Záldivar, J., Ortega, S., Castro, M.J., Casas, D. & Ercilla, G., 2022. Simulation of tsunami

induced by a submarine landslide in a glaciomarine margin: The case of storfjorden ls-1 (southwestern svalbard islands), *Nat. Hazards Earth Syst. Sci.,* **22,** 3839–3858.

Popinet, S., 2003. Gerris: a tree-based adaptive solver for the incompressible euler equations in complex geometries, *J. Comput. Phys.,* **190,** 572–600.

Poulain, P. *et al.*, 2022. Numerical simulation of submarine landslides and generated tsunamis: application to the on-going mayotte seismo-volcanic crisis, *C. R. Géosci.,* **354,** 361–390.

Poulain, P. *et al.*, 2023. Performance and limits of a shallow-water model for landslide-generated tsunamis: from laboratory experiments to simulations of flank collapses at montagne pelée (martinique), *Geophys. J. Int.,* **233,** 796–825.

Pouliquen, O. & Forterre, Y., 2002. Friction law for dense granular flows: application to the motion of a mass down a rough inclined plane, *J. Fluid Mech.,* **453,** 133–151.

Pörtner, H.-O. *et al.*, 2019. Ipcc special report on the ocean and cryosphere in a changing climate, *IPCC*. https://www.ipcc.ch/srocc/

Radjai, F. & Dubois, F., 2011, *Discrete-element modeling of granular materials,* Wiley-ISTE.

Rauter, M., Hoße, L., Mulligan, R.P., Take, W.A. & Løvholt, F., 2021. Numerical simulation of impulse wave generation by idealized landslides with openfoam, *Coast. Eng.,* **165,** 103 815. doi:10.1016/J.COASTALENG.2020.103815.

Rauter, M., Viroulet, S., Gylfadóttir, S.S., Fellin, W. & Løvholt, F., 2022. Granular porous landslide tsunami modelling–the 2014 lake askja flank collapse, *Nat. Commun.,* **13,** 1–13.

Roeber, V., Cheung, K.F. & Kobayashi, M.H., 2010. Shock-capturing boussinesq-type model for nearshore wave processes, *Coast. Eng.,* **57,** 407–423.

Roger, J., 2019. Potential tsunami hazard related to the seismic activity east of mayotte island, comoros archipelago., *Sci. Tsunami Hazards,* **38**.

Roger, J.H. *et al.*, 2024. A review of approaches for submarine landslide-tsunami hazard identification and assessment, *Mar. Petrol. Geol.,* **162,** 106 729. doi:10.1016/J.MARPETGEO.2024.106729.

Ruffini, G., Heller, V. & Briganti, R., 2021. Numerical characterisation and efficient prediction of landslide-tsunami propagation over a wide range of idealised bathymetries, *Coast. Eng.,* **167,** 103 854. doi: 10.1016/j.coastaleng.2021.103854.

Sabeti, R. & Heidarzadeh, M., 2022. Numerical simulations of tsunami wave generation by submarine landslides: Validation and sensitivity analysis to landslide parameters, *J. Waterway Port Coast. Ocean Eng.,* **148,** 05 021 016. doi:10.1061/(ASCE)WW.1943-5460.0000694/ASSET/3F278BB6-8B66-496A-9773-F990510ACB0F/ASSETS/IMAGES/LARGE/FIGURE13.JPG.

Saurel, J.M. *et al.*, 2021. Mayotte seismic crisis: building knowledge in near real-time by combining land and ocean-bottom seismometers, first results, *Geophys. J. Int.,* **228,** 1281–1293.

Savage, S.B. & Hutter, K., 1989. The motion of a finite mass of granular material down a rough incline, *J. Fluid Mech.,* **199,** 177–215.

Scala, A. *et al.*, 2024. Assessing the optimal tsunami inundation modeling strategy for large earthquakes in subduction zones, *J. geophys. Res.: Oceans,* **129,** e2024JC020941. doi:10.1029/2024JC020941.

Shi, F., Kirby, J.T., Harris, J.C., Geiman, J.D. & Grilli, S.T., 2012. A high-order adaptive time-stepping TVD solver for Boussinesq modelling of breaking waves and coastal inundation, *Ocean Model.,* **43-44,** 36–51.

Shu, C.W. & Osher, S., 1988. Efficient implementation of essentially non-oscillatory shock-capturing schemes, *J. Comput. Phys.,* **77,** 439–471.

Sánchez-Linares, C., de la Asunción, M., Castro, M.J., Mishra, S. & Šukys, J., 2015. Multi-level Monte Carlo finite volume method for shallow water equations with uncertain parameters applied to landslides-generated tsunamis, *Appl. Math. Model.,* **39,** 7211–7226.

Sultan, N., Jouet, G., Riboulot, V., Terzariol, M., Garziglia, S., Cattaneo, A., Giraudeau, J. & Jorry, S.J., 2023. Sea-level fluctuations control the distribution of highly liquefaction-prone layers on volcanic-carbonate slopes, *Geology,* **51,** 402–407.

Svennevig, K. *et al.*, 2024. A rockslide-generated tsunami in a greenland fjord rang earth for 9 days, *Science,* **385,** pp. 1196–1204, doi:10.1126/SCIENCE.ADM9247.

Thinon, I. *et al.*, 2022. Volcanism and tectonics unveiled in the Comoros archipelago between Africa and Madagascar, *C. R. - Geosci.,* **354,** 7–34.

Tinti, S., Bortolucci, E. & Romagnoli, C., 2000. Computer simulations of tsunamis due to sector collapse at Stromboli, Italy, *J. Volcanol. Geotherm. Res.,* **96,** 103–128.

Tozato, K., Moriguchi, S., Takase, S., Otake, Y., Motley, M.R., Suppasri, A. & Terada, K., 2023. Optimal probabilistic placement of facilities using a surrogate model for 3-D tsunami simulations, *Nat. Hazards Earth Syst. Sci.,* **23,** 1891–1909.

Watts, P., Grilli, S.T., Kirby, J.T., Fryer, G.J. & Tappin, D.R., 2003. Landslide tsunami case studies using a Boussinesq model and a fully nonlinear tsunami generation model, *Nat. Hazards Earth Syst. Sci.,* **3,** 391–402.

Wei, G., Kirby, J.T., Grilli, S.T. & Subramanya, R., 1995. A fully nonlinear Boussinesq model for surface waves. Part 1. Highly nonlinear unsteady waves, *J. Fluid Mech.,* **294,** 71–92.

Windows-Yule, C.R., Tunuguntla, D.R. & Parker, D.J., 2015. Numerical modelling of granular flows: a reality check, *Comput. Part. Mech.,* **3,** 311–332.

Yavari-Ramshe, S. & Ataie-Ashtiani, B., 2016. Numerical modeling of subaerial and submarine landslide-generated tsunami waves—recent advances and future challenges, *Landslides,* **13,** 1325–1368.

Zhao, H., Amann, F. & Kowalski, J., 2021. Emulator-based global sensitivity analysis for flow-like landslide run-out models, *Landslides,* **18,** 3299–3314.

## APPENDIX A: SPECIFICITY OF THE MAYOTTE's CONFIGURATION AND MANNING COEFFICIENT

Isolines of the Mayotte's bathymetry and a cross-section across the coral reef are shown in Fig. A1 to highlight the specificity of the Mayotte configuration. The spatialized Manning coefficient is presented in Fig. A2.

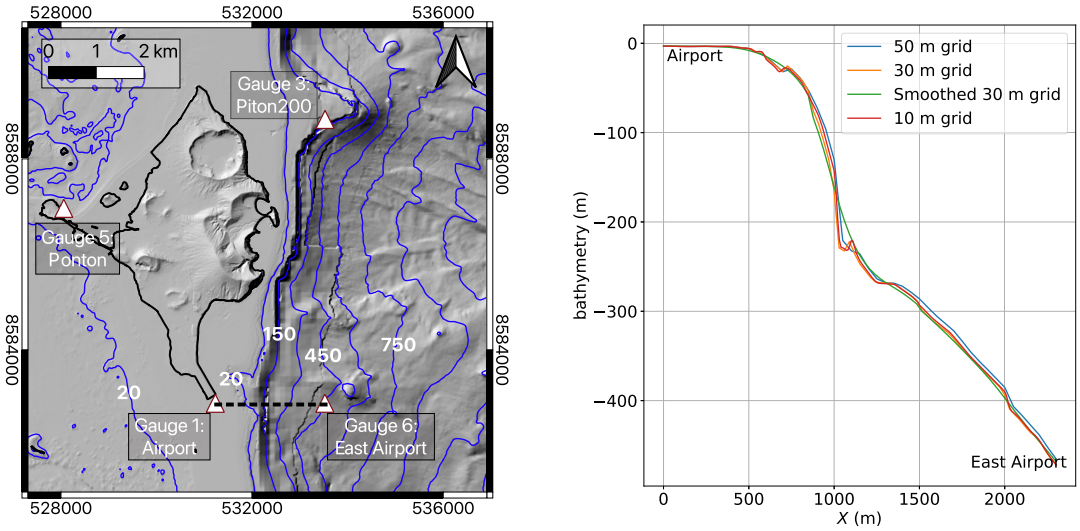


**Figure A1.** Bathymetric data and isolines at 20, 150, 300, 450, 600, 750, 900 and 1050 m depth. Cross-section of the bathymetric data between the airport and east airport gauges n°1 and 6 (gauges locations described in Subsection 2.3) for the 50, 30 (reference case) and 10 m grids as well as for the smoothed 30 m bathymetry. The dashed black line on the left panel indicates the cross-section location. The cross-section is built using the QGis open-source software.

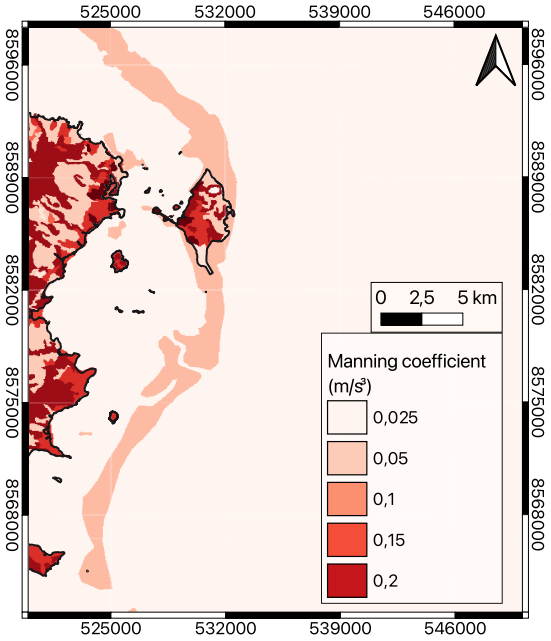


**Figure A2.** Values of the spatialized Manning coefficient used in this study (Lemoine *et al.* 2020b).

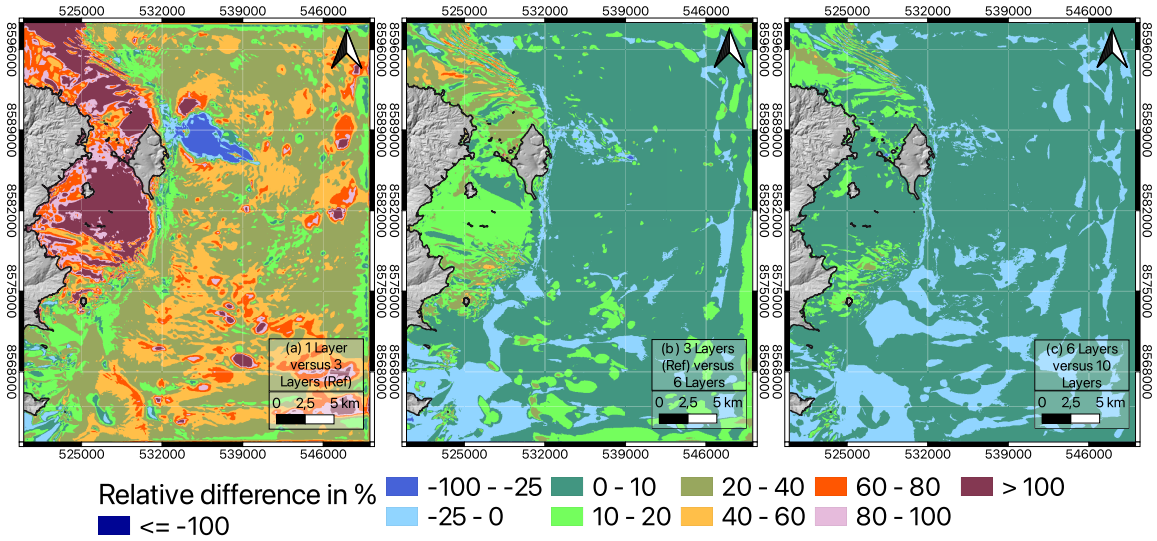


**Figure A3.** Relative signed difference $\Delta_{ij}$ in the maximum sea surface elevation $\iota_{ij}$ (eq. B1) given in percentage: (a) 1 Layer (Simu 1) versus 3 Layers (Simu 2, Ref of Table 1); (b) 6 Layers (Simu 2) versus 3 Layers (Simu 1, Ref of Table 1); (c) 10 Layers (Simu 2) versus 6 Layers (Simu 1). Minimum and maximum differences are: (a) −77 per cent up to 500 per cent; (b) −96 per cent up to 312 per cent; (c) −53 per cent up to 75 per cent.

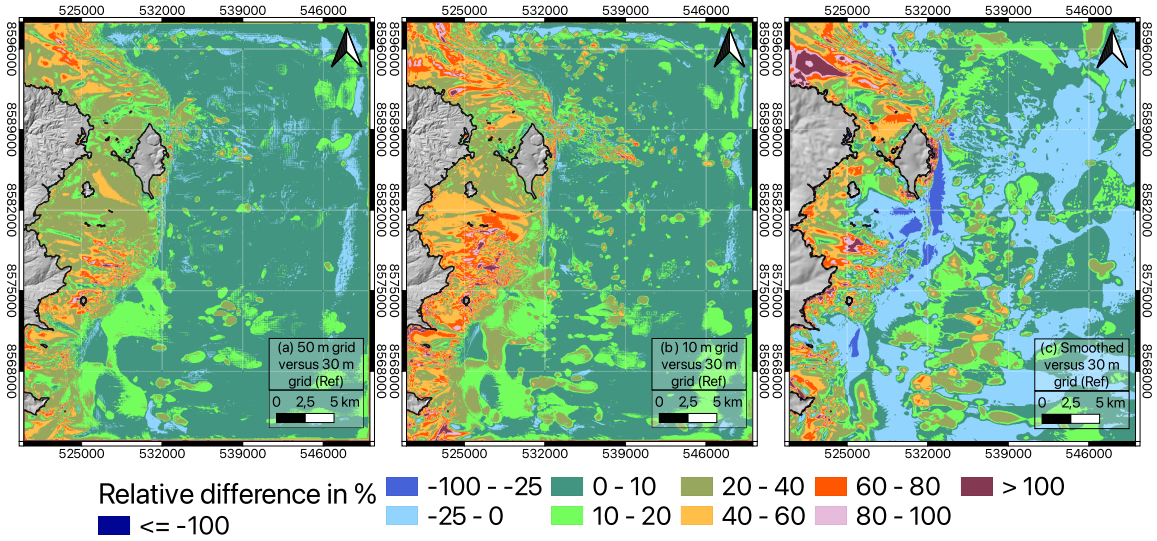


**Figure A4.** Relative signed difference $\Delta_{ij}$ in the maximum sea surface elevation $\iota_{ij}$ given in percentage (eq. B1): (a) 30 m grid (Simu 2, Ref of Table 1) versus 50 m grid (Simu 1); (c) 10 m grid (Simu 2) versus 30 m grid (Simu 1, Ref of Table 1); (e) Smoothed (Simu 2) versus 30 m grid (Simu 1, Ref of Table 1). Minimum and maximum differences are: (a) −40 per cent up to 140 per cent; b) −40 per cent up to 180 per cent; (c) −50 per cent up to 200 per cent.

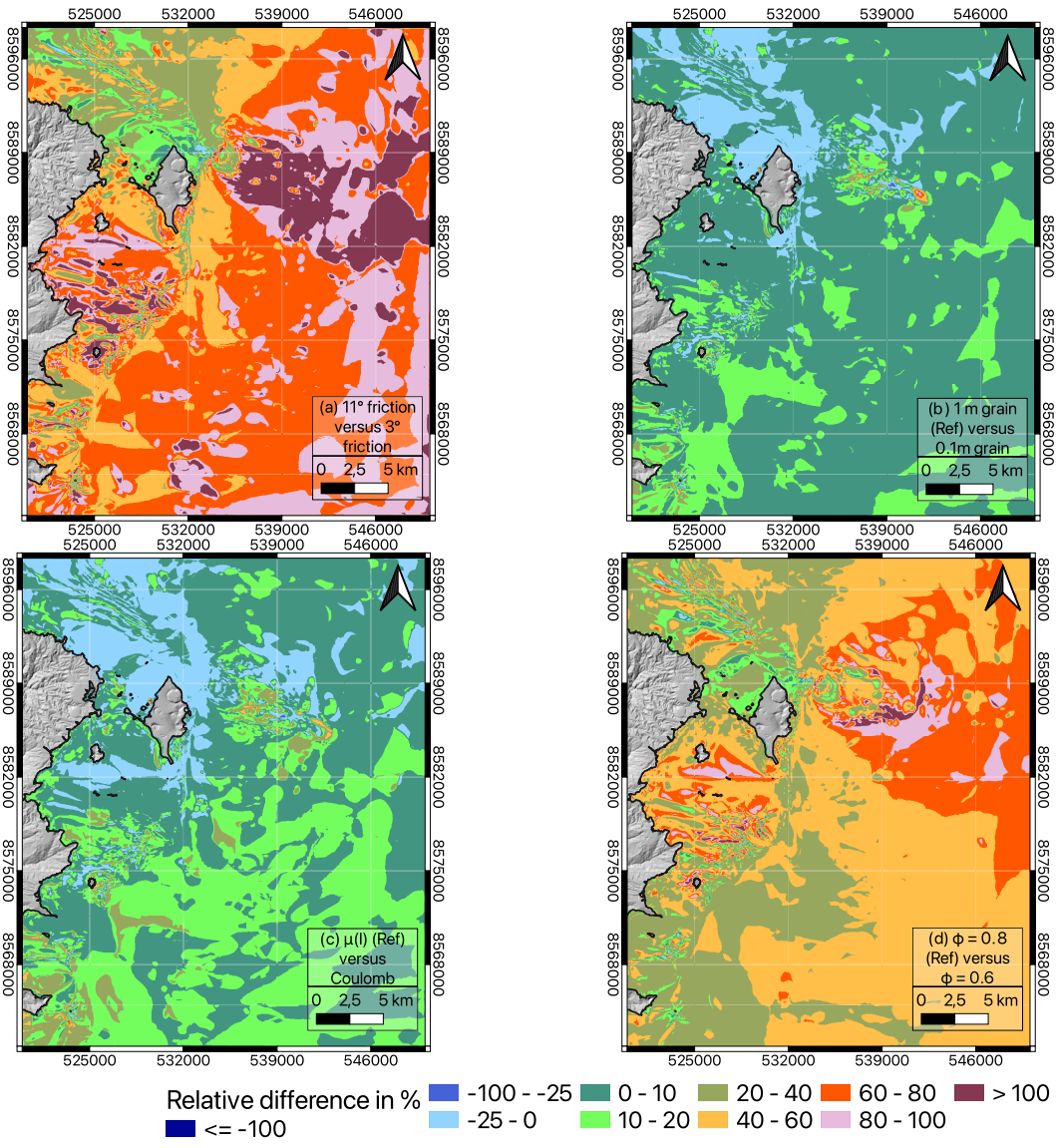


**Figure A5.** Relative signed difference $\Delta_{ij}$ in the maximum sea surface elevation (eq. B1) given in percentage: (a) 3° friction coefficient (Simu 2) versus 11° friction coefficient (Simu 1); (b) 0.1 m grain diameter (Simu 2) versus 1 m grain diameter (Simu 1, Ref of Table 1); (c) Coulomb friction law (Simu 2) versus $\mu(I)$ rheology (Simu 1, Ref of Table 1); and (d) $\Phi = 0.8$ (Simu 2, Ref of Table 1) versus $\Phi = 0.6$ (Simu 1). Minimum and maximum differences are: (a) −97 per cent up to 270 per cent; b) −29 per cent up to 51 per cent; c) −63 per cent up to 78 per cent; and d) −13 per cent up to 170 per cent.

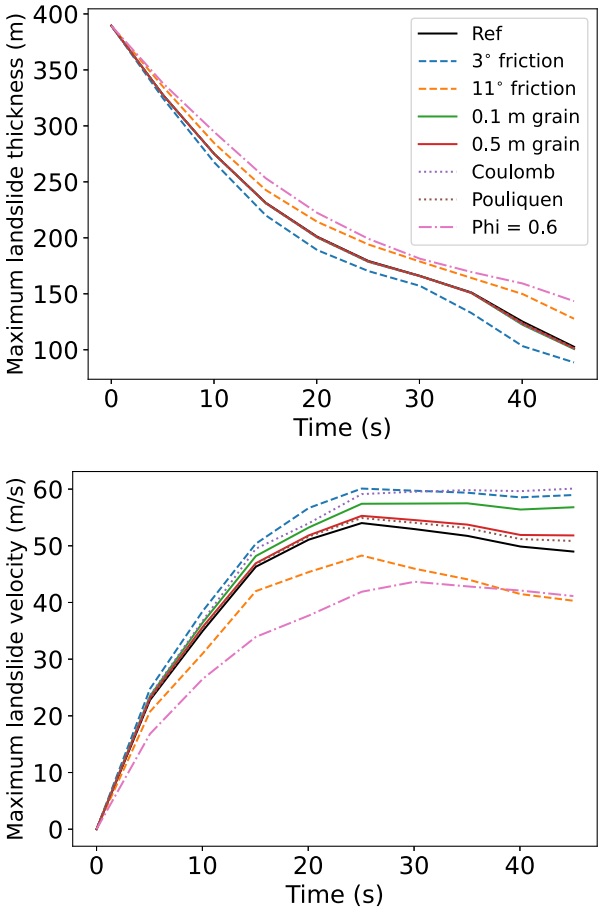


**Figure A6.** Maximum landslide thickness and velocity for the first 50 s.

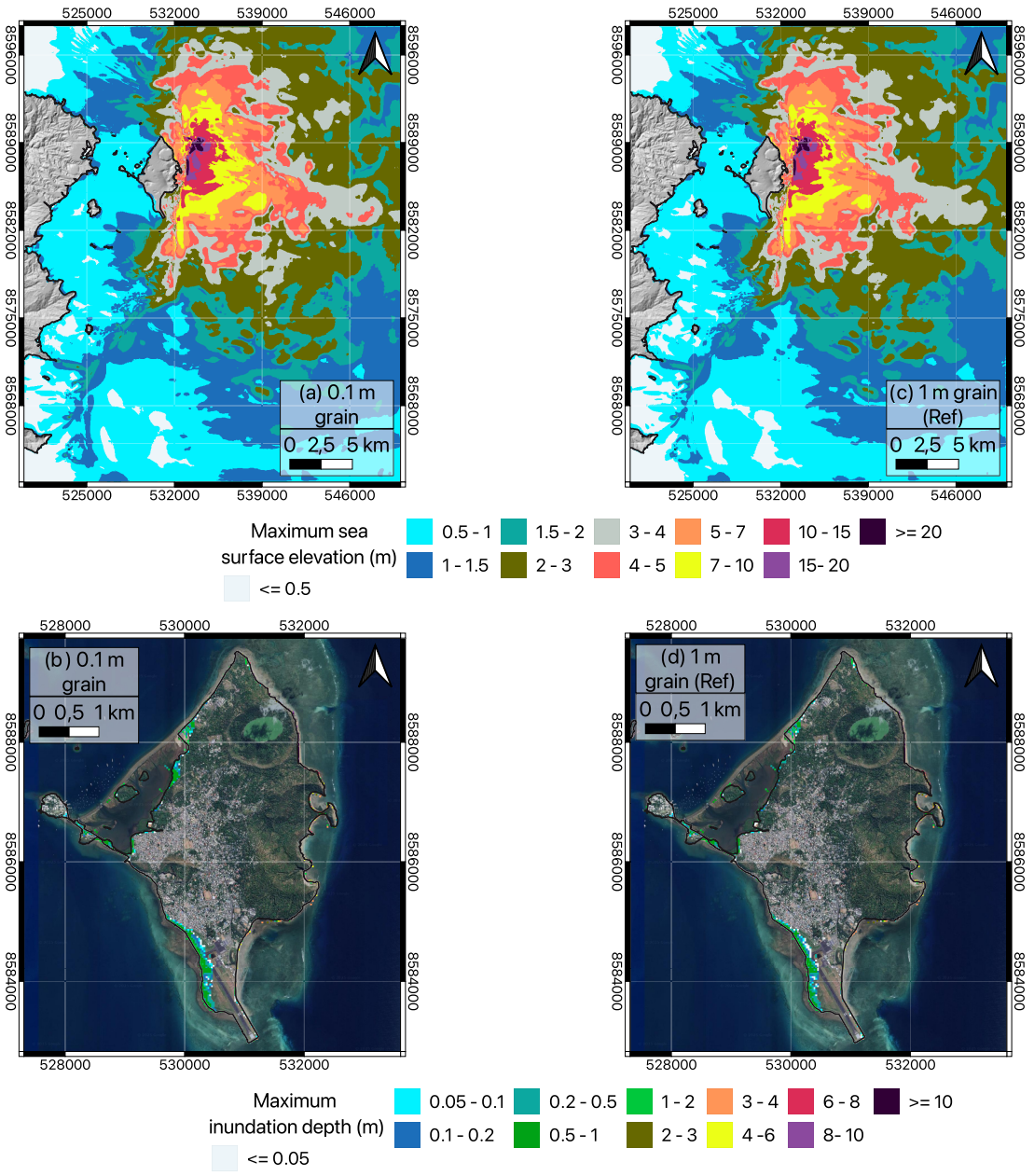


**Figure A7.** (a) Maximum sea surface elevation $\iota_{ij}$ (eq. 11) for a 0.1 m grain diameter. (b) Maximum inundation depth for a 0.1 m grain diameter. (c) Maximum sea surface elevation $\iota_{ij}$ (eq. 11) for a 1 m grain diameter (reference case). (d) Maximum inundation depth for a 1 m grain diameter (reference case).

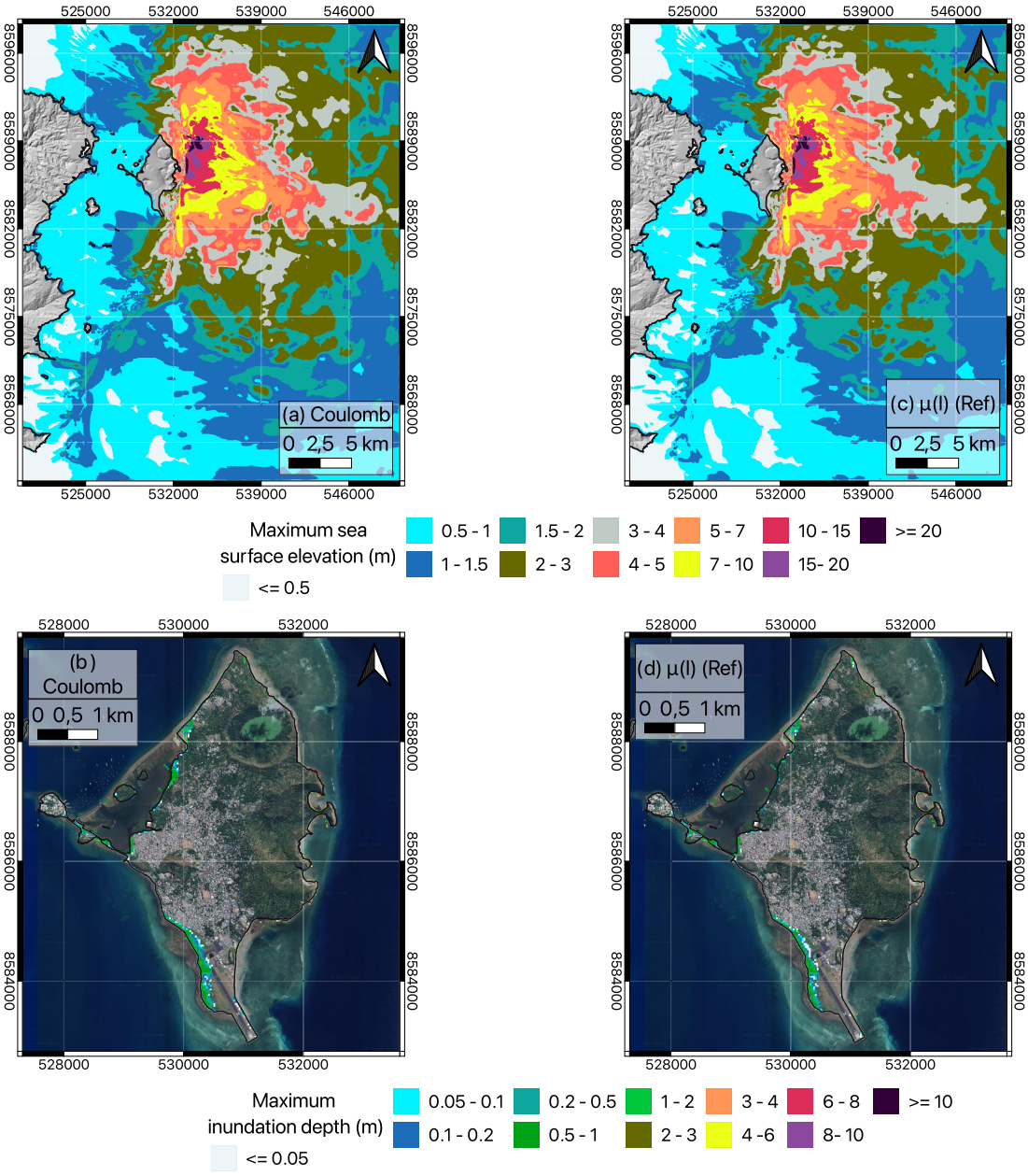


**Figure A8.** (a) Maximum sea surface elevation $\iota_{ij}$ (eq. 11) for the Coulomb friction law. (b) Maximum inundation depth for the Coulomb friction law. (c) Maximum sea surface elevation $\iota_{ij}$ (eq. 11) for the $\mu(I)$ rheology (reference case). (d) Maximum inundation depth for the $\mu(I)$ rheology (reference case).

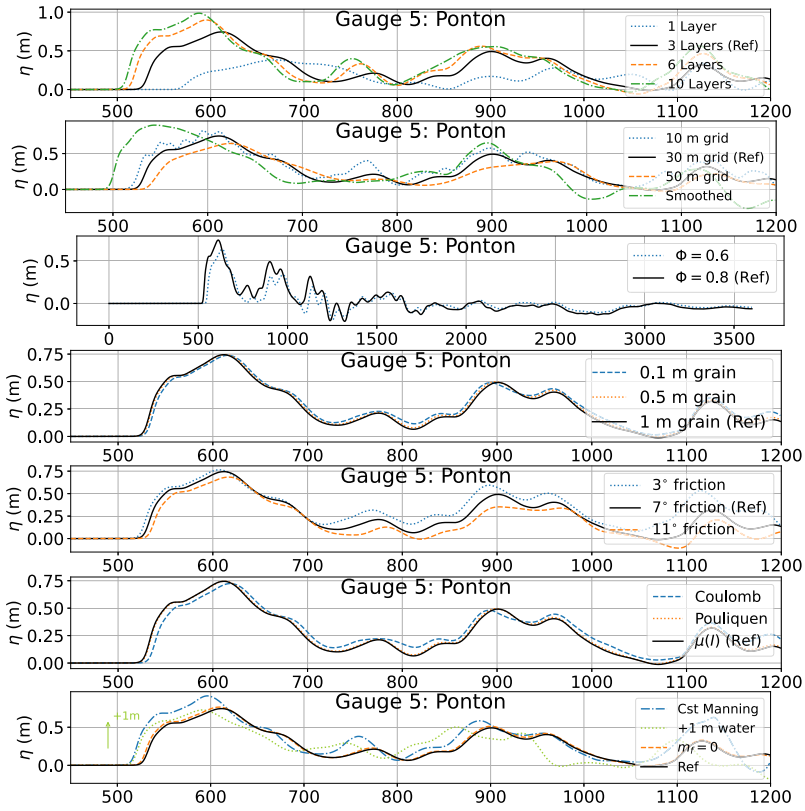


**Figure A9.** Sea surface elevation at the gauge n° 5: Ponton for the different simulations. The sea surface elevation has been shifted by −1 m for the '+1 m water' case to match the hydrostatic zero of other simulations for comparison purposes.

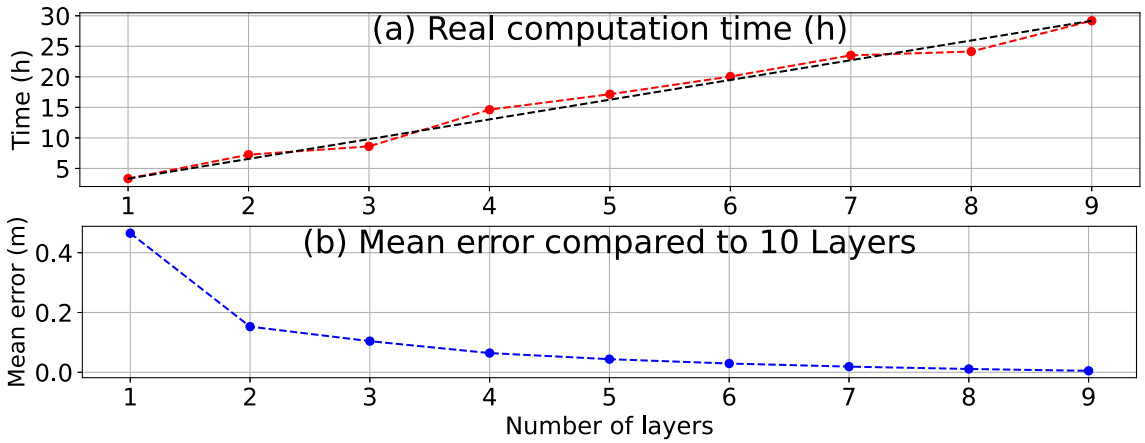


**Figure A10.** Mean error compared to the 10 layers case and computational real time for simulations with different numbers of layers: (a) Real computation time on 1 GPU (h); (b) average error (m) of eq. (E1).

**Table A1.** Avalanche parameters sensitivity analysis: recap of landslide data and comparison with the reference case.

| Landslide data | Runout (km) | Area $\times 10^7$ ($m^2$) | Max final thickness (m) |
|---|---|---|---|
| Ref | 8.14 | 2.05 | 59.04 |
| 0.1 m grain | 10.43 | 3.32 | 48.87 |
| 0.5 m grain | 8.87 | 2.38 | 55.48 |
| 3° friction | 12.79 | 3.92 | 51.63 |
| 11° friction | 5.36 | 1.19 | 85.54 |
| Coulomb | 11.46 | 4.21 | 49.00 |
| Pouliquen | 8.37 | 2.15 | 54.57 |
| $\Phi = 0.6$ | 8.18 | 2.01 | 59.29 |

**Table A2.** Gauge locations and depth. Coordinates are given in the system EPSG:4471-RGM04/UTM zone 38S as mentioned in Subsection 2.1.

| | $X$ (m) | $Y$ (m) | Depth (m) |
|---|---|---|---|
| Gauge 1: Airport | 531 228 | 8582 886 | 3.2 |
| Gauge 2: DEALM | 524 120 | 8585 883 | 2.5 |
| Gauge 3: Piton 200 | 533 524 | 8588 823 | 76.5 |
| Gauge 4: Offshore | 538 926 | 8588 820 | 1106 |
| Gauge 5: Ponton | 528 057 | 8586 964 | 9.8 |
| Gauge 6: East Airport | 533 521 | 8582 886 | 466 |

**Table A3.** Computational real time for a few simulations performed in this paper.

| | Computation time | GPU number |
|---|---|---|
| Ref | 8 hr 40 min | 1 |
| Hydro | 20 min | 1 |
| 1 Layer | 3 hr 20 min | 1 |
| 6 Layers | 20 hr | 1 |
| 10m grid | 5 d 19 hr | 2 |
| 50m grid | 3 hr 36 min | 1 |

## APPENDIX B: ADDITIONAL RESULTS ON THE MULTILAYER STRUCTURE AND BATHYMETRY EFFECTS

This Appendix presents the relative difference between cases related to the number of layers and bathymetric data are shown in Figs A3 and A4. The relative difference in the maximum sea surface elevation $\iota_{ij}$ between two simulations called Simu 1 and Simu 2 is computed by

$$\Delta_{ij} = 100 \times \frac{\iota_{ij}^{\text{Simu 2}} - \iota_{ij}^{\text{Simu 1}}}{\iota_{ij}^{\text{Simu 1}}}. \tag{B1}$$

The indices $i$ and $j$ stand for the grid points. A comparison of the landslide dynamics with the reference case is also shown in Fig. S2 (Supporting Information) for the Smoothed and the 10 m grid simulations. The maximum sea surface velocity is displayed in Fig. S1 in the Supporting Information.

## APPENDIX C: ADDITIONAL RESULTS ON EFFECTS OF LANDSLIDE RHEOLOGY AND FRICTION PARAMETERS

Landslide maximum velocities are shown in Figs S3 (reference case) and S4 (landslide parameters' simulations) in the Supporting Information. Relative differences on the maximum sea surface elevation are displayed in Fig. A5 for the different landslide parameters. Figs A7 and A8 provide the maximum sea surface elevation and the inundation pattern around Petite Terre related to the grain size parameter $d$ and the rheological law $\mu$. The results related to the friction angles have been kept in the main text (Fig. 16) since it presents the higher differences with the reference case among all the tested landslide parameters. The maximum landslide thickness and the mean landslide velocity for the first 50 s are presented in Fig. A6 for all tested landslide parameters. Table A1 collects the runout, area and maximum thicknesses for the simulations related to the landslide parameters.

## APPENDIX D: ADDITIONAL NUMERICAL GAUGES DATA

Appendix D presents additional gauge data.

### D1 Tables

Table A2 collects the coordinates and depth of each numerical gauge.

### D2 Gauge sea surface elevation

The data for the hydrostatic/non-hydrostatic feature, for the grain size related parameter $d$, and for the different rheological laws have been moved to the Supporting Information (Figs S6, S7 and S8). The gauge n°5 results are all gathered in Fig. A9. It allows a comparison of all our simulations from Table 1. From Fig. A9 and at this specific location, the parameters are classified from the most influential to the least: (1) dispersion properties (non-hydrostatic versus hydrostatic and the layer number); (2) bathymetric data and grid resolution; (3) friction angles $\delta$s; (4) initial water level; (5) Manning coefficient; (6) rheological law type and the solid volume fraction $\Phi$; (7) mass/water friction and grain size related parameter $d$. The gauge data for friction parameters and initial water level is also presented in the Supporting Information (Fig. S8). The spectral amplitude at the gauge n° 1 (airport) complete the Supporting Information (Fig. S9).

## APPENDIX E: COMPUTATION TIME

Fig. A10 presents the computation time against the number of layers and the mean error of eq. (E1)

$$\text{mean}\left(\iota_{ij}^{10\text{ Layers}} - \iota_{ij}^{\text{x Layers}}\right). \tag{E1}$$

Table A3 sums up the computation time and the number of used GPUs for a few relevant simulations listed in Table 1. The other simulations take the same time as the reference. The machine used for all the calculation possesses 4 GPUs NVIDIA Tesla V100 SXM2, each GPU attached with 16Go memory.

## APPENDIX F: NUMERICAL APPROXIMATION OF THE NON-HYDROSTATIC MULTILAYER MODEL

Systems (9) and (2) are solved simultaneously with a second-order HLL (Harten–Lax–van Leer), positivity-preserving, well-balanced, path-conservative finite volume numerical scheme (Castro-Diaz & Fernandez-Nieto 2012; Macías *et al.* 2021b). The time step is identical for the two systems and obey the usual CFL (Courant–Friedrichs–Lewy) derived for the complete system

$$\Delta t \max\left(\frac{1}{\Delta x}\max(|u|+\sqrt{gh}, |u_s|+\sqrt{g(1-r)h_s}),\ \frac{1}{\Delta y}\max(|v|+\sqrt{gh}, |v_s|+\sqrt{g(1-r)h_s})\right) \leq \frac{\text{CFL}}{2}$$

with CFL usually between 0.1 and 0.99. The CFL number is set to CFL = 0.55 for all simulations in this paper. It should be stressed that the non-hydrostatic corrections $\boldsymbol{K}_{NH}$ are computed separately since they require the discretization of an elliptic operator. It is achieved through standard second-order central finite differences. Special treatments are applied in regions with small water depth (Castro *et al.* 2005; Macías *et al.* 2021a). All the lengths are dimensionalized by $h_c = 1000$ m corresponding to characteristic depth and distance for all the Mayotte's simulations.

We consider a rectangular domain $[x_a, x_b] \times [y_a, y_b]$, which is discretized by a set of rectangular cells. Let us consider a partition $\{x_i\}_{i=1}^{N_x}$ of $[x_a, x_b]$, defined by $x_i = x_a + (i - \frac{1}{2})\Delta x$, with $\Delta x = (x_b - x_a)/N_x$, being $N_x$ the number of control volumes in the $X$-direction. Analogously, we consider a partition $\{y_j\}_{j=1}^{N_y}$ of $[y_a, y_b]$, defined by $y_j = y_a + (j - \frac{1}{2})\Delta y$, with $\Delta y = (y_b - y_a)/N_y$, being $N_y$ the number of control volumes in the $Y$-direction. Then, we consider the following definition of 2-D control volumes,

$$V_{i,j} = [x_{i-1/2}, x_{i+1/2}] \times [y_{j-1/2}, y_{j+1/2}], \qquad \begin{matrix} i = 1, \ldots, N_x \\ j = 1, \ldots, N_y \end{matrix}$$

being $\{V_{ij}\}_{i,j=1}^{N_x,N_y}$ a partition of the domain. Let us denote by $(\boldsymbol{U}_f)_{i,j}^n$ the approximation of the average of $\boldsymbol{U}_f(x, y, t)$ on the control volume $V_{i,j}$ at time $t^n$

$$(\boldsymbol{U}_f)_{i,j}^n = \begin{bmatrix} h_{i,j}^n \\ \begin{bmatrix} (h\,u)_{\alpha,i,j}^n \\ (h\,v)_{\alpha,i,j}^n \\ (hw)_{\alpha,i,j}^n \end{bmatrix}_{\{\alpha=1,\ldots,L\}} \end{bmatrix}.$$

The non-hydrostatic pressure unknowns are $\{p_{\alpha+1/2,i+1/2,j+1/2}^n\}_{i,j=0}^{N_x,N_y}$, approximations of $p(x, y, z, t)$ at $z = z_{\alpha+1/2}(x, y, t)$ for $(x, y) = (x_{i+1/2}, y_{j+1/2})$, the corners of the control volumes. Note that for $\alpha = L$, it corresponds to the non-hydrostatic pressure at the free surface, set to zero.

A splitting semi-implicit projection method is considered. For the explicit part, a two-steps second order TVD (Total Variation Diminishing) method is used (Shu & Osher 1988). The second order is achieved through reconstruction of states. For the sake of brevity, let us describe only the first order approximation of the model (9). The second order extension is done following Castro & Parés (2020). We solve the following discrete system

$$\begin{cases} \dfrac{(\boldsymbol{U}_f)_{i,j}^{n+1} - (\boldsymbol{U}_f)_{i,j}^n}{\Delta t} + \dfrac{(\boldsymbol{F}_f)_{i+1/2,j}^n - (\boldsymbol{F}_f)_{i-1/2,j}^n}{\Delta x} + \dfrac{(\boldsymbol{G}_f)_{i,j+1/2}^n - (\boldsymbol{G}_f)_{i,j-1/2}^n}{\Delta y} + (\boldsymbol{B}_f)_{i,j}^n = (\boldsymbol{H}_f)_{i,j}^n + (\boldsymbol{K}_{\text{KH}})_{i,j}^{n,n+1} - (\boldsymbol{S}_f)_{i,j}^{n,n+1} \\ (\widetilde{\nabla}_{\text{NH}})_{i+1/2,j+1/2}^{n,n+1} \cdot \boldsymbol{U}_f = \boldsymbol{0} \end{cases} \tag{F1}$$

Let us denote by $(\boldsymbol{U}_f)^{n,\pm}_{i+1/2,j}$ the hydrostatic reconstruction defined in terms of $(\boldsymbol{U}_f)^n_{i,j}$ and $(\boldsymbol{U}_f)^n_{i+1,j}$ (Audusse *et al.* 2006), and analogously for $(\boldsymbol{U}_f)^{n,\pm}_{i,j+1/2}$ in terms of $(\boldsymbol{U}_f)^n_{i,j}$ and $(\boldsymbol{U}_f)^n_{i,j+1}$. Then, the terms that appear in the previous system are defined as follows:

$$(\boldsymbol{F}_f)^n_{i+1/2,j} = \tfrac{1}{2}[\boldsymbol{F}_f((\boldsymbol{U}_f)^{n,-}_{i+1/2,j}) + \boldsymbol{F}_f((\boldsymbol{U}_f)^{n,+}_{i+1/2,j})] - \tfrac{1}{2}\Big(\alpha^n_{0,i+1/2,j}[(\boldsymbol{U}_f)^{n,+}_{i+1/2,j} - (\boldsymbol{U}_f)^{n,-}_{i+1/2,j}]$$
$$+\alpha^n_{1,i+1/2,j}[\boldsymbol{F}_f((\boldsymbol{U}_f)^{n,+}_{i+1/2,j}) - \boldsymbol{F}_f((\boldsymbol{U}_f)^{n,-}_{i+1/2,j}) - (\boldsymbol{H}_f)^n_{i+1/2,j}]\Big)$$

$$(\boldsymbol{G}_f)^n_{i,j+1/2} = \tfrac{1}{2}[\boldsymbol{G}_f((\boldsymbol{U}_f)^{n,-}_{i,j+1/2}) + \boldsymbol{G}_f((\boldsymbol{U}_f)^{n,+}_{i,j+1/2})] - \tfrac{1}{2}\Big(\alpha^n_{0,i,j+1/2}[(\boldsymbol{U}_f)^{n,+}_{i,j+1/2} - (\boldsymbol{U}_f)^{n,-}_{i,j+1/2}]$$
$$+\alpha^n_{1,i,j+1/2}[\boldsymbol{G}_f((\boldsymbol{U}_f)^{n,+}_{i,j+1/2}) - \boldsymbol{G}_f((\boldsymbol{U}_f)^{n,-}_{i,j+1/2}) - (\boldsymbol{H}_f)^n_{i,j+1/2}]\Big).$$

The coefficients $\alpha_0$ and $\alpha_1$ defining the HLL method (Castro-Diaz & Fernandez-Nieto 2012), are given by

$$(\alpha_0)^n_{i+1/2,j} = \frac{S_{\mathrm{R}}|S_{\mathrm{L}}| - S_{\mathrm{L}}|S_{\mathrm{R}}|}{S_{\mathrm{R}} - S_{\mathrm{L}}}, \quad (\alpha_1)^n_{i+1/2,j} = \frac{|S_{\mathrm{R}}| - |S_{\mathrm{L}}|}{S_{\mathrm{R}} - S_{\mathrm{L}}},$$

where

$$S_{\mathrm{L}} = \min\left(\bar{u}^n_{i+1/2,j} - \sqrt{g h^n_{i+1/2,j}}, (u_{\mathrm{s}})^n_{i+1/2,j} - \sqrt{g(1-r)(h_{\mathrm{s}})^n_{i+1/2,j}}\right).$$
$$S_{\mathrm{R}} = \max\left(\bar{u}^n_{i+1/2,j} + \sqrt{g h^n_{i+1/2,j}}, (u_{\mathrm{s}})^n_{i+1/2,j} + \sqrt{g(1-r)(h_{\mathrm{s}})^n_{i+1/2,j}}\right).$$

Coefficients $(\alpha_0)_{i,j+1/2}$ and $(\alpha_1)_{i,j+1/2}$ are defined analogously, in terms of $(v_{\mathrm{s}})^n_{i,j+1/2}$, $\bar{v}_{i,j+1/2}$, $(h_{\mathrm{s}})^n_{i,j+1/2}$ and $h^n_{i,j+1/2}$.

The approximation of the term $\boldsymbol{H}_f$ is the following

$$(\boldsymbol{H}_f)^n_{i,j} = \frac{(\boldsymbol{H}_f)^n_{i+1/2,j} + (\boldsymbol{H}_f)^n_{i-1/2,j}}{2\Delta x} + \frac{(\boldsymbol{H}_f)^n_{i,j+1/2} + (\boldsymbol{H}_f)^n_{i,j-1/2}}{2\Delta y}$$

where

$$(\boldsymbol{H}_f)^n_{i,j+1/2} = \left[\begin{bmatrix} 0 \\ 0 \\ -g\,\frac{h^{n,+}_{i,j+1/2} + h^{n,-}_{i,j+1/2}}{2}\,(h^{n,+}_{i,j+1/2} - h^{n,-}_{i,j+1/2}) \\ 0 \end{bmatrix}_{\{\alpha\}}\right].$$

for $\alpha = 1, \ldots, L$. The approximation of $\boldsymbol{B}_f$ is defined as follows:

$$(\boldsymbol{B}_f)^n_{i,j} = \frac{(\boldsymbol{B}_f)^n_{i+1/2,j} + (\boldsymbol{B}_f)^n_{i-1/2,j}}{2\Delta x} + \frac{(\boldsymbol{B}_f)^n_{i,j+1/2} + (\boldsymbol{B}_f)^n_{i,j-1/2}}{2\Delta y}$$

with

$$(\boldsymbol{B}_f)^n_{i+1/2,j} = \left[\begin{bmatrix} 0 \\ (u^n_{\alpha+1/2,i+1/2,j}\Gamma^n_{\alpha+1/2,i+1/2,j} - u^n_{\alpha-1/2,i+1/2,j}\Gamma^n_{\alpha-1/2,i+1/2,j}) \\ (v^n_{\alpha+1/2,i+1/2,j}\Gamma^n_{\alpha+1/2,i+1/2,j} - v^n_{\alpha-1/2,i+1/2,j}\Gamma^n_{\alpha-1/2,i+1/2,j}) \\ (w^n_{\alpha+1/2,i+1/2,j}\Gamma^n_{\alpha+1/2,i+1/2,j} - w^n_{\alpha-1/2,i+1/2,j}\Gamma^n_{\alpha-1/2,i+1/2,j}) \end{bmatrix}_{\{\alpha\}}\right]$$

and

$$(\boldsymbol{B}_f)^n_{i,j+1/2} = \left[\begin{bmatrix} 0 \\ (u^n_{\alpha+1/2,i,j+1/2}\Gamma^n_{\alpha+1/2,i,j+1/2} - u^n_{\alpha-1/2,i,j+1/2}\Gamma^n_{\alpha-1/2,i,j+1/2})/l_\alpha \\ (v^n_{\alpha+1/2,i,j+1/2}\Gamma^n_{\alpha+1/2,i,j+1/2} - v^n_{\alpha-1/2,i,j+1/2}\Gamma^n_{\alpha-1/2,i,j+1/2})/l_\alpha \\ (w^n_{\alpha+1/2,i,j+1/2}\Gamma^n_{\alpha+1/2,i,j+1/2} - w^n_{\alpha-1/2,i,j+1/2}\Gamma^n_{\alpha-1/2,i,j+1/2})/l_\alpha \end{bmatrix}_{\{\alpha\}}\right].$$

for $\alpha = 1, \ldots, L$. The terms in $(\boldsymbol{B}_f)^n_{i+1/2,j}$ and $(\boldsymbol{B}_f)^n_{i,j+1/2}$ are given by

$$\Gamma^n_{1/2,i+1/2,j} = \Gamma^n_{L+1/2,i+1/2,j} = 0,$$
$$\Gamma^n_{1/2,i,j+1/2} = \Gamma^n_{L+1/2,i,j+1/2} = 0,$$
$$\Gamma^n_{\alpha+1/2,i+1/2,j} = \sum_{\beta=1}^{\alpha} l_\beta\Big(h^{n,+}_{i+1/2,j}(\bar{u}^{n,+}_{i+1/2,j} - u^{n,+}_{\beta,i+1/2,j}) \qquad - h^{n,-}_{i+1/2,j}(\bar{u}^{n,-}_{i+1/2,j} - u^{n,-}_{\beta,i+1/2,j})\Big),$$
$$\Gamma^n_{\alpha+1/2,i,j+1/2} = \sum_{\beta=1}^{\alpha} l_\beta\Big(h^{n,+}_{i,j+1/2}(\bar{v}^{n,+}_{i,j+1/2} - v^{n,+}_{\beta,i,j+1/2}) \qquad - h^{n,-}_{i,j+1/2}(\bar{v}^{n,-}_{i,j+1/2} - v^{n,-}_{\beta,i,j+1/2})\Big),$$

for $\alpha = 1, \ldots, L-1$, with $u^n_{\alpha+1/2,i+1/2,j} = (u^{n,+}_{\alpha,i+1/2,j} + u^{n,-}_{\alpha,i+1/2,j} + u^{n,+}_{\alpha+1,i+1/2,j} + u^{n,-}_{\alpha+1,i+1/2,j})/4$ and analogous definitions for $v^n_{\alpha+1/2,i+1/2,j}$, $w^n_{\alpha+1/2,i+1/2,j}$, $v^n_{\alpha+1/2,i,j+1/2}$ and $w^n_{\alpha+1/2,i,j+1/2}$.

The discretization of the non-hydrostatic gradient pressure terms is given by

$$(\boldsymbol{K}_{NH})_{i,j}^{n,n+1} = \begin{bmatrix} 0 \\ \begin{bmatrix} (K_x)_{\alpha,i,j}^{n,n+1} \\ (K_y)_{\alpha,i,j}^{n,n+1} \\ -(p_{\alpha+1/2,i,j}^{n+1} - p_{\alpha-1/2,i,j}^{n+1})/l_\alpha \end{bmatrix}_{\{\alpha\}} \end{bmatrix}$$

for $\alpha = 1, \ldots, L$, where

$$(K_x)_{\alpha,i,j}^{n,n+1} = \Big( - h_{i+1/2,j}^n p_{\alpha,i+1/2,j}^{n+1} + h_{i-1/2,j}^n p_{\alpha,i-1/2,j}^{n+1} + p_{\alpha+1/2,i,j}^{n+1}(z_{\alpha+1/2,i+1/2,j} - z_{\alpha+1/2,i-1/2,j})/l_\alpha - p_{\alpha-1/2,i,j}^{n+1}(z_{\alpha-1/2,i+1/2,j} - z_{\alpha-1/2,i-1/2,j})/l_\alpha \Big)/(\Delta x),$$

$$(K_y)_{i,j}^{\alpha,n,n+1} = \Big( - h_{i,j+1/2}^n p_{\alpha,i,j+1/2}^{n+1} + h_{i,j-1/2}^n p_{\alpha,i,j-1/2}^{n+1} + p_{\alpha+1/2,i,j}^{n+1}(z_{\alpha+1/2,i,j+1/2} - z_{\alpha+1/2,i,j-1/2})/l_\alpha - p_{\alpha-1/2,i,j}^{n+1}(z_{\alpha-1/2,i,j+1/2} - z_{\alpha-1/2,i,j-1/2})/l_\alpha \Big)/(\Delta y),$$

$p_{\alpha,i+1/2,j}^{n+1} = (p_{\alpha+1/2,i+1/2,j} + p_{\alpha-1/2,i+1/2,j})/2$ and $p_{\alpha+1/2,i,j} = (p_{\alpha+1/2,i-1/2,j-1/2} + p_{\alpha+1/2,i-1/2,j+1/2} + p_{\alpha+1/2,i+1/2,j-1/2} + p_{\alpha+1/2,i+1/2,j+1/2})/4$.

The friction and breaking terms, defined in $\boldsymbol{S}_f$, are discretized semi-implicity

$$(\boldsymbol{S}_f)_{i,j}^{n,n+1} = \begin{bmatrix} 0 \\ g\, h_{i,j}^n \frac{n^2}{l_1 (h_{i,j}^n)^{4/3}} u_{1,i,j}^{n+1} \sqrt{(u_{1,i,j}^n)^2 + (v_{1,i,j}^n)^2} - m_f (u_{s,i,j}^{n+1} - u_{1,i,j}^n) \\ g\, h_{i,j}^n \frac{n^2}{l_1 (h_{i,j}^n)^{4/3}} v_{1,i,j}^{n+1} \sqrt{(u_{1,i,j}^n)^2 + (v_{1,i,j}^n)^2} - m_f (v_{s,i,j}^{n+1} - v_{1,i,j}^n) \\ m_1^{w,n,n+1} \\ \begin{bmatrix} 0 \\ 0 \\ m_\alpha^{w,n,n+1} \end{bmatrix}_{\{\alpha=2,\ldots,L\}} \end{bmatrix},$$

with

$$m_\alpha^{w,n,n+1} = \frac{C_{i,j}^n}{l_\alpha^2} G_{\alpha,i,j}^n\, w_{\alpha,i,j}^{n+1},$$

$$G_{\alpha,i,j}^n = \left( \left( \frac{(hu)_{\alpha,i+1,j}^n) - (hu)_{\alpha,i-1,j}^n)}{2\Delta x} \right)^2 + \left( \frac{(hv)_{\alpha,i,j+1}^n) - (hv)_{\alpha,i,j-1}^n)}{2\Delta x} \right)^2 \right)^{1/2}$$

for $\alpha = 1, \ldots, N$, and $C_{i,j}^n = 35 \max\left( \frac{\sqrt{(\bar{u}_{i,j}^n)^2 + (\bar{v}_{i,j}^n)^2}}{0.4\sqrt{g h_{i,j}^n}} - 1, 0 \right)$.

Finally, a projection method is considered, which is based on a semi-implicit discretization of the divergence operator at the corners of the control volumes $x_{i+1/2,j+1/2}$ for $i = 0, \ldots, N_x$ and $j = 0, \ldots, N_y$. The discretization of the divergence type operator associated to the multilayer system is

$$h_{i+1/2,j+1/2}^n (\widetilde{\nabla}_{NH})_{i+1/2,j+1/2}^{n,n+1} \cdot \boldsymbol{U}_f = \begin{bmatrix} l_1 h_{i+1/2,j+1/2}^n ((hu)_{1,i+1,j+1/2}^{n+1} - (hu)_{1,i,j+1/2}^{n+1})/\Delta x - l_1 (hu)_{i+1/2,j+1/2}^{n+1} (h_{i+1,j+1/2}^n - h_{i,j+1/2}^n)/\Delta x \\ + l_1 h_{i+1/2,j+1/2}^n ((hv)_{1,i+1/2,j+1}^{n+1} - (hv)_{1,i+1/2,j}^{n+1})/\Delta y - l_1 (hv)_{i+1/2,j+1/2}^{n+1} (h_{i+1/2,j+1}^n - h_{i+1/2,j}^n)/\Delta y \\ + 2((hw)_{1,i+1/2,j+1/2}^{n+1} - (hw)_{0,i+1/2,j+1/2}^{n+1}) \\ \begin{bmatrix} ((hu)_{\alpha+1,i+1/2,j+1/2} - (hu)_{\alpha,i+1/2,j+1/2})(z_{\alpha+1/2,i+1,j+1/2} - z_{\alpha+1/2,i,j+1/2})/\Delta x \\ + ((hv)_{\alpha+1,i+1/2,j+1/2} - (hv)_{\alpha,i+1/2,j+1/2})(z_{\alpha+1/2,i+1/2,j+1} - z_{\alpha+1/2,i+1/2,j})/\Delta y \\ - ((hw)_{\alpha+1,i+1/2,j+1/2}^{n+1} - (hw)_{\alpha,i+1/2,j+1/2}^{n+1}) \end{bmatrix}_{\{\alpha\}} \end{bmatrix}$$

for $\alpha = 1, \ldots, L-1$, where $w_0$ is defined as an approximation of $\partial_t(-H + h_s)$. In the previous equation, the following notation has been considered: $(hu)_{\alpha,i+1/2,j+1/2} = ((hu)_{\alpha,i,j} + (hu)_{\alpha,i+1,j} + (hu)_{\alpha,i,j+1} + (hu)_{\alpha,i+1,j+1})/4$, $(hu)_{\alpha,i,j+1/2} = ((hu)_{\alpha,i,j} + (hu)_{\alpha,i,j+1})/2$, and analogously for $h$, $(hv)$ and $(hw)$. The non-hydrostatic pressure approximation are obtained by solving a linear system. It is deduced by substituting the expression of $\boldsymbol{U}_f^{n+1}$ into the previous equation associated to the discretization of the velocity divergence.